UNIVERSITÀ DI PARMA

UNIVERSITÁ DEGLI STUDI DI PARMA

DOTTORATO DI RICERCA IN SCIENZA E TECNOLOGIA DEI MATERIALI

CICLO XXXII

# CARBON NANOSTRUCTURES FOR IONIC BATTERIES

Coordinatore:
Chiar.mo Prof. Enrico Dalcanale

Tutore:
Chiar.mo Prof. Mauro Riccò

Co-tutore:
Chiar.mo Prof. Daniele Pontiroli

Dottorando: Silvio Scaravonati

Anni 2016/2019

## Abstract

Lithium-ion rechargeable batteries are currently the state-of-the-art energy storage technology for devices as cell phones, laptops and electric cars. Despite their top performances, some problems have yet to be solved. The first issue is availability: lithium is difficult to recycle and, while still available in large quantities, not enough to support a future economy based on electric vehicles. The second problem is performances: despite Li-ion batteries are state-of-the-art among other battery technologies, their performances are still not competitive with fossil fuels, in terms of energy density and power density. The last issue is safety: Li-ion batteries have been reported to heat up, catch fire or even explode. Most of such safety issues come from the electrolyte, which is the most flammable element in a battery. Typical electrolytes are also toxic, and can easily leak out of a battery.

Among the possible alternatives to Li-ion batteries, sodium-ion batteries and magnesium-ion batteries are particularly relevant, since both sodium and magnesium are far more abundant in nature and hence less expensive than lithium. One of the biggest challenges in realizing sodium- or magnesium-ion batteries is represented by finding materials suitable to intercalate such ions with competitive performances with respect to lithium-ion ones, especially as far as the negative electrode is concerned; this is due to the fact that graphite, the most commonly used material for lithium-ion batteries, cannot intercalate sodium or magnesium to a significant extent. A promising substitute is $C_{60}$ fullerene, which can host in its crystal structure Na ions and Mg ions up to a stoichiometry of respecitvely $Na_{11}C_{60}$ and $Mg_5C_{60}$. This is favoured by the large interstitial voids between fullerene molecules in the crystal and by the tendency of $C_{60}$ to accept electrons from alkali and alkali-earth metals. Sodium-ion and magnesium-ion batteries with anodes based on fullerene and two fullerene-related materials, fullerene mixture and hydrogenated fullerene, were assembled and tested. Each material was electrochemically intercalated with sodium and magnesium, with a specific capacity respectively up to 320 mA h $g^{-1}$ and 125 mA h $g^{-1}$, although with a reversibility loss after the first cycles.

Improvements in battery technology can also be achieved by developing novel, more performing materials as electrodes for Li-ion batteries. Graphene, thanks to its similarity with graphite, good electrical conductivity and high specific surface area, is a good candidate to improve performances, especially fast rate of charge and discharge, of lithium-ion batteries, and former studies demonstrated capability of intercalating graphene and hydrogenated graphene up to 500 mA h $g^{-1}$. In this study, diffusion mechanisms of graphene and hydrogenated graphene are characterized by means of electrochemical impedance spectroscopy.

Hydrogenated graphene boasted an impressive reversible specific capacity with fast charge/discharge capabilities, exceeding 370 mA h $g^{-1}$ even at the high C-rate of 25C. Moreover, for the first time, thermally exfoliated graphene and hydrogenated graphene were coupled to proper cathode materials, in order to study and develop full-cell prototypes, more similar to a commercially viable product.

Lastly, one possible approach to solve liquid electrolyte-related safety issues in batteries, is the development of solid electrolytes, which cannot leak out of the batteries, and are more stable at high temperatures or if exposed to air. However, the vast majority of solid electrolytes cannot compete with liquid electrolytes in terms of room temperature ionic conductivity, which is the capability of allowing the passage of ions. Lithium borohydride is a good solid electrolyte at high temperature, and some derivatives of $C_{60}$, like $Li_4C_{60}$ and $Mg_2C_{60}$, are super ionic conductors at room temperature. Fullerene-borohydiride composite materials with high ionic conductivity were synthesised and characterized. $LiBH_4$-$Li_6C_{60}$ composite showed an ionic conductivity of $6{\cdot}10^{-5}$ S $cm^{-1}$ at room temperature, which is 100 times higher than pure $LiBH_4$, while $NaBH_4$-$Na_6C_{60}$ boasted an ionic conductivity of $5{\cdot}10^{-5}$ S $cm^{-1}$ at room temperature.

# Acknowledgements

First and foremost, the most special thanks are due to my supervisors, who have been able to create a hospitable and fruitful working environment: Prof. Mauro Riccò for his competence, experience and preciseness, and Prof. Daniele Pontiroli for his expertise and his step-by-step guidance during all my Ph. D. research. I also thank both for the help with the revision of this thesis.

Thanks are due to C1P8 s.r.l. in the person of Dott. Stefano Armani for the financial support.

Many thanks are also due to all my lab mates, for helping me with my research, as well as for the useful conversation and for sharing all fortunes and misfortunes: Giacomo Magnani, Laura Fornasini, Michele Sidoli, and Alberto Morenghi. I wish to thank also all my fellow Ph.D. and master degree students, for the refreshing lunch breaks.

Special thanks go to the Columbus team at the Center for Automotive Research of The Ohio State University, from whom I received the best hospitality during my stage in the United States of America, Prof. Marcello Canova and Prof. Jung-Hyun Kim, as well as all my lab mates Lalith Rao, Ke Pan, Junbin Choi, and Chan-Yeop Yu.

Last but not least, I wish to express my gratitude to all the people who indirectly helped my work: my family and friends, who contributed to keep my morale up.

# Contents

# List of Figures

# Chapter 1

# Introduction

## 1.1 The energy problem

Nowadays, humanity is highly dependent on energy in its many forms. Most of the energy we use is obtained from non-renewable sources; in 2018, more than 84% of energy was produced from combustion of fossil fuels (coal, natural gas, oil), and 4% from nuclear power plants[1]. Such energy sources are heavily impactful on the environment and are destined to depletion, so switching to renewable sources is an undeniable need. Most developed countries are dedicating research and investments to renewable energy.

The most crucial problems of most renewable energy sources are the intrinsic intermittence and hard predictability of energy output. In fact, renewable energy obtained from sources such as wind or solar light cannot provide a constant energy output (Figure 1.1(a)); performance of non-renewable sources can be achieved by renewable ones by employing storage systems, so that excess energy can be used in times of low output.

The study of energy storage systems is also important in the field of transports, in which fossil fuels are still the uncontested protagonists. This is mainly due to two advantages: lower costs and capacity of carrying more energy per unit mass, with respect to other energy storage systems for vehicles. The use of fossil fuel for transports comes with the obvious disadvantage of air pollution.

## 1.2 Batteries

Rechargeable batteries have been attracting a lot of attention as power supply for electric vehicles, and are being used as an alternative to pumped-storage hydroelectricity for storing the extra energy produced by intermittent energy

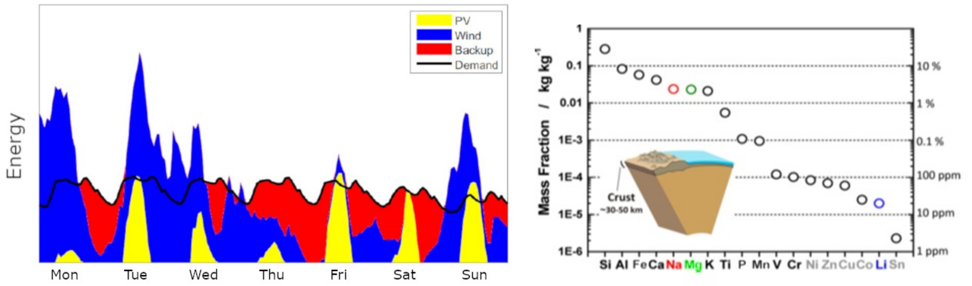

(a) (b)

Figure 1.1: (a) Energy demand and supply for a typical winter week in Germany[2]. (b) Mass fraction of elements in the Earth crust. Lithium, sodium and magnesium are highlighted[3].

sources, to make it available when it is needed[4]. Batteries store chemical energy and release it as electrical energy with a high efficiency: since they operate at a constant temperature, they are not bound by Carnot limit for maximum efficiency, unlike heat engines[5]. Batteries also supply power to all portable electric devices (cell phones, laptops, cameras, etc.) thanks to their small size, capability to be adapted to any shape, and the fact that batteries' higher costs are less impactful in small devices.

One of the reasons for the fast growth of rechargeable battery trade, is the development of lithium-ion batteries (LIB), capable of high performance and high specific energy. They are now 63% of world rechargeable battery market[6], corresponding to annual sales of over 7 billion dollars[7]. The most promising employment for lithium-ion technology is that of electric vehicles, thanks to their top performance and relatively low weight, compared to other battery technologies. Despite the good performance of LIB, electric vehicles still fail to be competitive on the market, due to high costs, short battery lifespan, and more importantly low range. Specific energy of fossil fuels is about 1300-1600 W h kg$^{-1}$, while best LIB have a specific energy up to 240 W h kg$^{-1}$[8][9] (Figure 1.2); the development of more performing batteries is then crucial to obtain a more widespread diffusion of electric cars. Another concern about LIB is safety; when used in vehicles and portable devices they can inflate or heat up, which may also cause the ignition or the explosion of the battery[10].

LIB are a promising perspective also as storage systems to complement renewable resource energy production. Nowadays, most of the energy produced in large power plants is stored in dams with pumped water, while LIBs are mostly employed in small, domestic-sized production systems, due to their cost and average lifespan[4]; however, in the recent years, more and more storage plants rely on battery storage power plants, as a result of the fast decrease in the cost of this technology, caused by the electric automotive industry: when batteries are employed in renewable energy storage, the high performance needed in the automotive area is not required, since weight is not a concern. Used batteries, coming from electric vehicles and discarded due to their performance loss after many cycles, can be refurbished and exploited in power plants[11].

One of the main issues of LIB is natural availability of lithium (Figure 1.1(b)). Although lithium is the $25^{th}$ most abundant element of the earth crust, most of it is found in a very low concentration, about 0.17 ppm, in seawater[12]. Moreover, due to its high reactivity, lithium is never found as a pure metal but only in compounds, and can be reasonably extracted only from mines, sometimes in critical conditions for workers. Consequently, effectively exploitable lithium reserves are estimated to be about 14 million tons worldwide[13]. Despite such reserves are theoretically enough to satisfy world lithium demand for more than a hundred years, they would rapidly become insufficient if LIB were employed massively in electric cars and for power plant energy storage[14].

Some possible alternatives are represented by batteries in which the charge carrier is a different element: for example sodium, magnesium, fluorine, aluminium. Sodium and magnesium have some characteristics in common with lithium, for example they have a small ionic radius and a tendency to donate electrons, so these alternative elements are supposedly well suited to take lithium's place in batteries. Both sodium and magnesium are also very abundant in nature, as they constitute respectively 2.6% and 2% of earth crust[15]. Employment of either sodium or magnesium could also contribute to the decrease of the cost of batteries. However, such batteries are not commercially available yet, due to some technological issues, which make them non-competitive. One of the main problems consists in the fact that graphite, which is commonly used as anode (ion-hosting negative electrode) in LIB, isn't suitable to host sodium or magnesium[16][17]. It is then crucial to find a proper replacement in order to develop commercially competitive sodium- or magnesium-ion batteries. In the case of sodium-ion batteries, cathode and electrolyte technology can be partially recovered from LIB, thanks to the chemical similarity of sodium and lithium. In the case of magnesium, some more issues have to be addressed: $Mg^{2+}$ ions are highly reactive, and it is necessary to employ different electrolytes[18] and cathodes[19]. Consequently, Mg-ion batteries are farther from commercialization than Na-ion batteries.

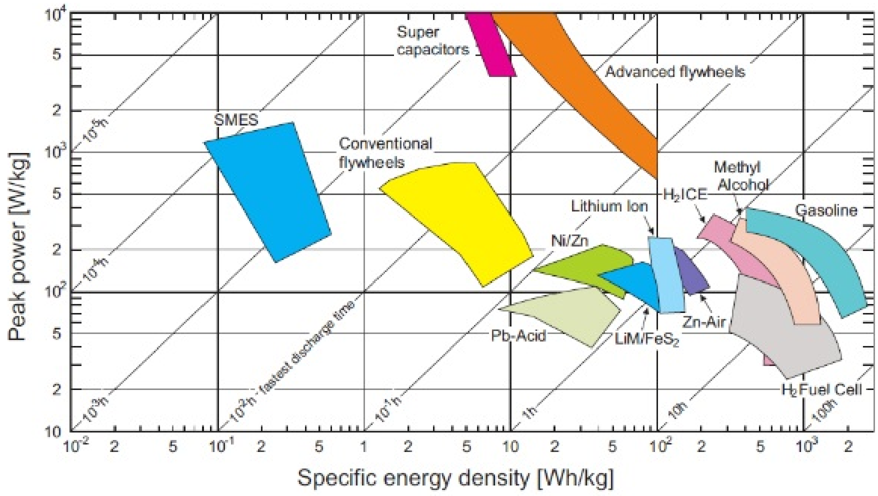

Figure 1.2: Specific power and specific energy of different fuels and energy storage technologies[9].

## 1.3 Aims of the study

The aim of this study is to address different problems about batteries - performance, safety, materials availability and costs - by exploiting the properties of carbon nanostructured materials. Carbon nanostructures are artificial materials in which one or more dimensions are smaller than tens of nanometers. Carbon nanostructures are good candidates as anode materials alternative to graphite in ionic batteries, due to their unique properties, such as high specific surface area, good electrical conductivity and capability of hosting alkali and alkali-earth ions. Among the many carbon nanostructures, fullerene and graphene, have been proven to be promising electrode materials[20][21].

### 1.3.1 Fullerene

$C_{60}$ fullerene is a football-shaped molecule in which 60 carbon atoms are placed as vertices of a truncated icosahedron. Its crystal structure is able to intercalate, which means to host in the void space between molecules, atoms of many different elements, especially alkali and alkali-earth metals. This property is due on the one hand to large availability of empty space, on the other hand to the capability of $C_{60}$ molecules to accept electrons from intercalant elements which, donating one or more electrons, form with $C_{60}$ charge transfer salts. It was demonstrated that it is possible to intercalate sodium and magnesium ions in fullerene crystal structure. For sodium, up to 11 sodium atoms can be intercalated per $C_{60}$ molecule, forming sodium clusters inside the largest interstitial voids[22]. For magnesium, up to 5 ions can be intercalated per $C_{60}$ molecule[23]. Following the discoveries of the capability of fullerene to intercalate sodium and magnesium ions, interest in exploiting fullerene as battery electrode rose significantly, and it was proven that sodium and magnesium ions can be electrochemically intercalated in fullerene[24][25]. Such discoveries also resulted in a Toyota patent[26] about fullerene as electrode material in magnesium-ion batteries.

Such discoveries attracted the attention of C1P8 s.r.l., one of the few fullerene producers worldwide, which sponsored this study in order to find new uses of fullerene in ionic batteries. In this work, $C_{60}$ fullerene was characterized as anode material for magnesium-ion batteries and, for the first time, in sodium-ion batteries, in order to better understand the physical process of ion intercalation and to develop new battery technologies. Some intrinsic limits of fullerene were encountered, such as a low reversibility of the intercalation precess; consequently, different fullerene-related materials were optimized and characterized as well. In particular, hydrogenated fullerene and mixture of different fullerene molecules, were studied. Hydrogenated fullerene, in which hydrogen atoms are chemically attached to fullerene molecules, was employed in order to increase the dimension of interstitial voids, since hydrogenation results in an expansion of the crystal structure, and to hinder polymerization between fullerene molecules, which prevents ion extraction after the first cycle. Hydrogenation was reported to improve performance of fullerene in LIB[20]. Mixture of different fullerene molecules was also studied, due to the same reasons for which hydrogenated fullerene was employed: expansion of the crystal structure and hindrance of polymerization. Fullerene mixture also has the advantage of being less expensive than pure $C_{60}$, since the latter is refined from fullerene mixture. Moreover, cells were made using solid electrolyte, realizing the first fullerene-based all solid-state sodium-ion batteries.

### 1.3.2 Graphene

Graphene is a single layer of carbon atoms in a two-dimensional hexagonal honeycomb-like lattice. It can be considered the basic constituent of graphite, since the latter is made up by many graphene layers stacked onto one another. Graphene is characterized by a very good electrical conductivity and an outstanding specific surface area; as such, it is a good candidate as anode material for batteries, in order to increase batteries' specific capacity and maximum rate of charge and discharge; thanks to its affinity with graphite, batteries with graphene-based anodes can be assembled easily by partially exploiting the already established technology. Former studies demonstrated capability of reversibly intercalating graphene and hydrogenated graphene with lithium and sodium[21], and graphene-related materials have been reported to achieve high specific capacities, up to 1200 $\mathrm{mA\ h\ g^{-1}}$[27]; sodium intercalation mechanism in graphene has also been already investigated in detail with nuclear magnetic resonance[28]. Many different methods of synthesis have been proposed for graphene; however, properties of graphene are strongly dependent on the synthesis method[29]. In this study, graphene synthesized with a scalable method was characterized as anode material in LIB, in order to better understand intercalation mechanisms and to develop novel technologies for LIB. Graphene was also subject to a hydrogenation process, in order to remove oxygen atoms and saturate dangling bonds, which are a consequence of the synthesis process. Moreover, graphene and hydrogenated graphene were coupled to suitable cathodes, in order to develop complete prototypes, more similar to a possible commercially viable product; in fact, lithium was chosen as active ion because many commercial lithium-ion cathodes are available and well established. The possibility of realizing graphene-based full-cells with $LiFePO_4$ has been reported before[30]; in this study, for the first time, graphene produced by thermal exfoliation with a highly scalable method and hydrogenated graphene were coupled to three different cathodes to realize lithium-ion full-cells.

### 1.3.3 Solid electrolytes

Another possible approach to improve batteries is that of developing solid electrolytes, which are materials with a high ionic mobility but negligible electronic conductivity. Solid electrolytes would be able to solve many safety problems deriving from the use of liquid electrolytes, such as toxicity and possibility of leaks and of ignition[31]. However, batteries employing solid electrolytes have yet to be commercialized, due to the fact that their ionic conductivity at room temperature is lower than that of conventional electrolytes. Research on solid electrolytes has attracted a considerable interest in the last years, and different classes of ionic conductors have been identified. Complex metal hydrides, like $MAH_4$ (M=alkali metal, A=Al,B) compounds, are characterized by a fast ionic conductivity but only at high temperatures; for example lithium borohydride ($LiBH_4$) features an ionic conductivity up to $10^{-3}$ S cm$^{-1}$, but only after a phase transition occurring at about 390 K[32]. Another class of solid electrolytes consists in ceramic ionic conductors, for example $Li_{1.4}Al_{0.4}Ti_{1.6}(PO_4)_3$[33], which can achieve ionic conductivities up to $10^{-3}$ S cm$^{-1}$, but with poor mechanical properties and a difficulty to obtain good interfacial contact with the electrode[34]. Some solid solutions of salts in certain polymers are also characterized by a good ionic conductivity, as for example polyethylene oxide-based solid solutions, in which a phase transition from crystal to amorphous, occurring above 330 K, allows ionic conductivity up to $10^{-4}$ S cm$^{-1}$[35]. Lastly, ionic conductivity has been observed in some fullerene-based systems, like $Li_4C_{60}$[36] and $Mg_2C_{60}$[37], which are characterized by room temperature ionic conductivities of about respectively

$10^{-2}$ and $10^{-4}$ S $cm^{-1}$, although with a possible concurrent non-negligible electronic conductivity. In this work, solid electrolyte composites with enhanced ionic conductivity were realized and characterized, using lithium and sodium borohydride in conjunction with different fullerene derivatives: $Li_xC_{60}$ (x=4,6,12) and $Na_6C_{60}$. Moreover, a gel electrolyte, made by combining a $Mg(AlCl_2BuEt)_2$-polyvinylidene fluoride composite, reported by [38], with $C_{60}$, was synthesized and characterized, with the aim of enhancing ionic conductivity, as reported in a lithium-ion ionic conductor[39].

# Chapter 2

# Batteries

## 2.1 Introduction

An electric battery is a device which converts the chemical energy of its active materials into electric energy. Batteries are divided into two categories:

- **Primary batteries**: disposable, non-rechargeable electrochemical cells. Primary batteries' size and voltage are standardized.

- **Secondary batteries**: rechargeable electrochemical cells. Secondary batteries are devices in which charge can be restored by applying a proper electrical current. Devices usually determine shape and voltage of the rechargeable batteries they are powered with.

Rechargeable batteries are usually employed in devices that need more energy and longer duration than those powered by primary batteries. They also have a lower environmental impact and are economically advantageous if they are used for a sufficiently long period; for this reason, lifetime of a rechargeable battery is an important parameter. Moreover, ageing effects have to be taken into account, since performance of rechargeable batteries gradually decreases over many charge and discharge cycles. Lithium-ion batteries are also subject to degradation over time, even if unused.

When used as renewable energy backup or as power source in electric vehicles, rechargeable batteries are needed, due to their capability of repeatedly storing and supplying energy. Among all technological advancements, rechargeable batteries are characterized by a slow growth, as compared to most common devices (Figure 2.1). Specific capacity increase in commercial lithium-ion batteries has only been of about 8% per year[40]; this is mainly due to the difficulty of both finding novel, suitable materials for battery components, and developing optimal interfaces between them[6]. Only research can advance rechargeable battery technology, and developing new, more performing

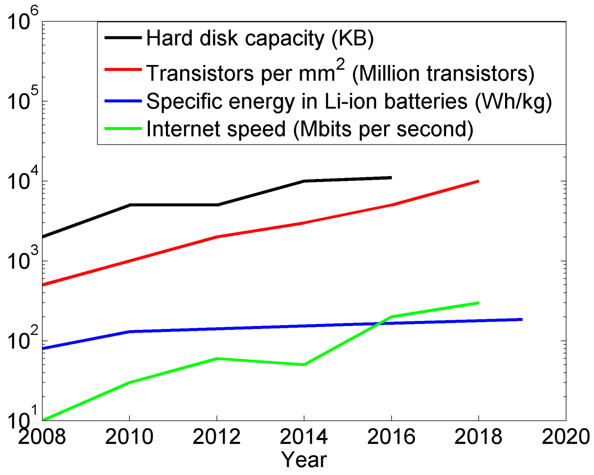

Figure 2.1: Comparison of different technology advancements over the last years[41][42][43][44].

materials is one of the most promising ways to achieve the best results.

## 2.2 Working principle

Despite many different kinds of battery exist, all of them share the same working principle. Batteries are defined as electrochemical (or galvanic) cells, and essentially exploit a spontaneous redox reaction, in which Gibbs free energy decreases, while chemical energy is converted into electrical energy. Each battery is made up of three parts:

- **anode**: negative electrode. It is made of a material with a lower standard redox potential than that of the positive electrode. When the electrochemical cell is supplying current, the anode is oxidized, forfeiting electrons to the electrode with higher potential. In batteries based on alkali and alkali-earth elements, positively charged ions migrate from the anode to the cathode during discharge.
- **separator** and **electrolyte**: the separator is an electrically insulating material needed to avoid electrical contact between anode and cathode. It is soaked in the electrolyte, which is typically a salt dissolved in a proper solvent. The main property an electrolyte must have is that in such material electric current is carried by ions, while passage of electrons is not allowed.
- **cathode**: positive electrode. During discharge, it is subject to a reduction reaction, accepting electrons.

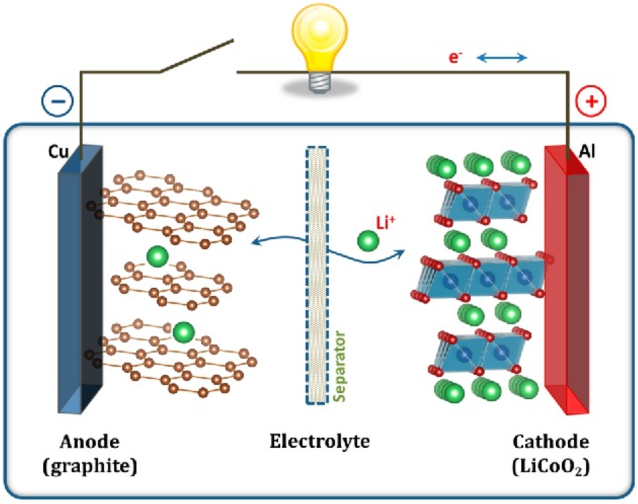

Figure 2.2: Scheme of a typical Li-ion battery, with graphite-based anode and $LiCoO_2$-based cathode[45].

A typical scheme for an electrochemical cell is shown in figure 2.2. In the example a Li-ion battery, with graphite-based anode and lithium cobalt oxide ($LiCoO_2$)-based cathode, is considered. Outside of a cell, the following reaction occurs between the electrode materials:

$$LiCoO_2 + 6C \longrightarrow Li_{1-x}CoO_2 + Li_xC_6 \tag{2.1}$$

This is a spontaneous reaction, and the driving force is the difference in Gibbs free energy between the products ($CoO_2$+$LiC_6$), and the reagents ($LiCoO_2$+graphite)[5]:

$$\Delta G = \sum \Delta G(products) - \sum \Delta G(reagents) \tag{2.2}$$

$$\Delta G = [\Delta G(CoO_2) + \Delta G(LiC_6)] - [\Delta G(LiCoO_2) + \Delta G(C)] \tag{2.3}$$

In an electrochemical cell, a separator, soaked in the electrolyte, is placed between anode and cathode. The electrolyte allows the movement of ions, in the example $Li^+$ ions, while electrons are blocked. In order for the reaction to take place, it is necessary that neutral charge is conserved on both the electrode, so in a system made of anode, electrolyte and cathode no reaction is allowed, since electrons cannot cross the electrolyte to balance the charge carried by positively charge ions. The reaction is allowed when an external circuit, connecting anode and cathode, is added, so that electrons can move to the anode and balance the charge. In this case two reactions occur: one at the anode and the other at the cathode. The different reactions occurring in the example cell are:

Anode:

$$Li_xC_6 \xrightleftharpoons[\text{discharge}]{\text{charge}} xLi^+ + 6C + xe^- \tag{2.4}$$

Cathode:

$$xLi^{+} + Li_{1-x}CoO_2 + xe^{-} \xleftrightarrow[\text{discharge}]{\text{charge}} LiCoO_2 \tag{2.5}$$

Overall:

$$CoO_2 + LiC_6 \xleftrightarrow[\text{discharge}]{\text{charge}} LiCoO_2 + 6C \tag{2.6}$$

Where $0 \leq x \leq 1$. The opposite process occurs when the battery is charged: an external current is applied in the opposite direction and ions are forced to cross the electrolyte, reverting the electrode materials back, in a non-spontaneous reaction[5].

During the first few cycles of a Li-ion battery, degradation of part of the electrolyte occurs on the surface of the negative electrode. This is due to the fact that organic solvent are unstable at highly negative potentials. The product of this degradation is called solid electrolyte interphase (SEI), and is typically a layer of decomposed, lithium containing compounds on the anode. An important feature of SEI is that of being permeable to alkali metal ions, while also blocking further reactions between the electrolyte and the electrode[5].

## 2.3 Sodium-ion and magnesium-ion batteries

Lithium-ion batteries have the issue of a low natural availability of lithium; effectively exploitable lithium reserves are estimated to be about 14 million tons worldwide[13], theoretically sufficient to satisfy world lithium demand for more than a hundred years, but in a short time insufficient if lithium-ion batteries were employed massively in electric cars and for power plant energy storage[14]. Among the many different elements that can be used as active ions in ionic batteries, sodium and magnesium are highly promising, having some characteristics in common with lithium, such as a small ionic radius and a tendency to donate electrons, but also being highly abundant in nature and cheaper than lithium. However, sodium- and magnesium-ion batteries are not commercially available yet, mainly due to the the fact that graphite, which is commonly used as anode (ion-hosting negative electrode) in lithium-ion batteries, isn't suitable to host sodium or magnesium[16][17]. In the case of magnesium-ion batteries, another issue is that divalent $Mg^{2+}$ ions are highly reactive, and it is necessary to employ organo-magnesium electrolytes, due to the fact that common electrolytes produce a blocking SEI layer[18], and particular cathode materials, due to the fact that solid state diffusion of magnesium in commonly used metal oxide cathodes is as low as $10^{-15}$ $cm^2$ $s^{-1}$[19]. Consequently, Mg-ion batteries are farther from commercialization than Na-ion batteries.

Many efforts have been made towards the realization of competitive sodium-ion or magnesium-ion batteries. In sodium-ion batteries, different classes of materials have been adopted as anodes. Carbon based-anode materials have the advantage of being rather inexpensive, and of having a low potential vs $Na/Na^+$, but with the disadvangage of a lower specific capacity. Among the many carbon-based materials tested as anodes in Na-ion batteries, such as petroleum cokes[46], carbon black[47], pitch-based carbon fibers[48], and polymers[49], the best results have been obtained with hard-carbons, which are carbon materials synthesized from carbon-based precursors at high temperatures in inert atmosphere; sodium-ion batteries with hard carbon-based anodes were proven to have reversible specific capacities up to 220 mA h $g^{-1}$[14]. Such performance can be improved if hard carbon is arranged in micro or nanostructures, achieving reversible specific capacities up to 315 mA h $g^{-1}$[50]. Metal oxide anode materials have also been tested. Most metal oxides have the disadvantage of a high intercalation potential vs $Na/Na^+$; among those with a low enough potential $NiCo_2O_4$ has been reported to achieve a specific capacity up to about 200 mA h $g^{-1}$, with the working principle of a conversion reaction in which sodium does not intercalate into the spinel-like structure of $NiCo_2O_4$, but rather reacts with it forming sodium oxide ($Na_2O$)[51][14]. Intermetallic compounds, such as the SnSb alloy, have been reported to boast an reversible specific capacity of over 500 mA h $g^{-1}$, but with volume expansion up to 400%, which is typically undesirable due to the fact that they can cause damage to the cells[14]; the volume change can be buffered by embedding metal nanoparticles in a matrix, typically of carbon nanostructures, enhancing specific capacity up to 630 mA h $g^{-1}$ and preventing damage to the electrode[52]. Performance of all solid-state sodium-ion batteries is typically lower, ranging from a reversible specific capacity of 40 mA h $g^{-1}$ with sulfur electrodes[53] to a maximum of 64 mA h $g^{-1}$[54].

In magnesium-ion batteries, the realization of anodes is more challenging, and high specific capacities have been achieved only with expensive materials based on rare elements as bismuth, with a reversible specific capacity of 360 mA h $g^{-1}$[55]. Bismuth-tin alloys have been reported to have a specific capacity up to 1000 mA h $g^{-1}$[56], but with a high enough bismuth content ($Bi_3Sn_2$) to discourage practical applications. Carbon-based anode materials would be a cheaper alternative based on an abundant element, but so far very few attempts have been made to develop carbon-based Mg-ion battery anodes, with specific capacities not exceeding 50 mA h $g^{-1}$[25].

## 2.4 Main physical quantities

- **Capacity**: the capacity of a battery is defined as the maximum electrical charge that can be accumulated. Despite the fact that the International System unit for electrical charge is Coulomb, capacity is commonly expressed in $mA\ h$ or $A\ h$ when referring to batteries, so that it is easier to guess the time in which a battery will be completely discharged for a given current. Capacity of a battery can be calculated by:

$$C = \int I(t)dt$$

Specific capacity is the capacity of an electrode per unit mass of the active materials, and is usually expressed in $mA\ h\ g^{-1}$.

- **Potential or Voltage**: Difference of potential between the electrodes of a battery. Theoretical potential is given by the difference between the standard potentials of the active materials of the cathode and the anode:

  $$\Delta V(cell) = V^o(cathode) - V^o(anode)$$

  where the standard potentials $V^o$ stand for the standard potentials of each materials with respect to hydrogen, taken as reference.

- **Energy density**: available energy per unit volume. It is a useful parameter for batteries destined to portable devices, in which small dimensions are desirable. It is frequently expressed in $W\,h\,l^{-1}$. Maximum energy is given by:

  $$E = \int \Delta V(t) I dt$$

  and energy density is the ratio between maximum energy and cell volume.

- **Specific energy**: available energy per unit mass. It is an important parameter for batteries destined to supply much energy in a low weight, as for example in automotive applications. It is typically expressed in $W\ h\ kg^{-1}$, and is calculated by dividing the maximum energy for the mass of the cell.

- **Specific power**: power supplied by the battery per unit mass. It is commonly expressed in $W\ kg^{-1}$.

- **Efficiency**: ratio between the amount of charge supplied by the battery during discharge and of charge supplied to the battery during charge, and quantifies the amount of charge that can be effectively exploited.

  $$\eta = \frac{Q_{discharge}}{Q_{charge}}$$

- **Rate of charge/discharge**: also called *C-rate*, it is the ratio between current of charge/discharge and nominal capacity of the battery, defined as the capacity for a slow rate of charge. It is equivalent to the reciprocal of the time of discharge. It is expressed with the formula $C/X$, where $X$ is the number of hours needed to completely discharge the battery: so for example C/10 (or 0.1 C) corresponds to the current at which the cell is completely discharged in 10 hours, while C/1 (or 1 C) corresponds to the current at which the cell is completely discharged in 1 hour. Higher rates of charge/discharge determine a decrease in capacity.

- **Open circuit voltage**: also known as open circuit potential, and often referred to as OCV, it is the difference in potential between the electrodes when the battery is at rest, as opposed to the terminal voltage, which is the difference in potential when a load is applied.
- **Internal resistance**: the overall resistance within the battery, which determines the heating of the battery during usage and most of the efficiency loss.
- **State of charge**: abbreviated as SOC, it is the ratio between the capacity available in the battery, and the nominal capacity. It is a dimensionless value, and describes the usable charge at a given time. It is often calculated from the charge already flown from the battery:

  $$SOC = \frac{C(t)}{C_{nominal}} = 1 - \frac{\int_0^t I(t)dt}{C_{nominal}}$$

  SOC is usually expressed as a percentage.
- **Reversibility**: reversibility is the ratio between the capacity of a given discharge and the capacity of the first discharge. It is often expressed as a percentage.

# Chapter 3

# Materials

## 3.1 Fullerene

Fullerene is a class of allotropes of carbon, discovered in 1985 by Kroto, Curl and Smalley, who demonstrated, by means of mass spectrometry, the existence of a molecule made of 60 atoms of carbon; the discovery earned the three scientists the Nobel prize in chemistry in 1996[57]. The name "fullerene" comes from architect R. Buckminster Fuller, whose geodesic domes resemble the shape of the molecule. An efficient method to produce fullerene in considerable quantity was developed in 1990 by Kratschmer and Huffman, and consists in the application of an arc discharge between two rods of ultra-pure graphite in a reactor filled with an inert gas. Heat generated by the discharge causes the evaporation of carbon from the rods, which then cools down and forms a soot containing approximatively 15% of fullerenes[58]. From the soot, amorphous carbon can be removed to obtain the so-called fullerene mixture, which contains different-sized fullerene molecules, with a composition approximately of 80% $C_{60}$ and 20% $C_{70}$, with traces of higher order fullerenes[59]; the mixture can be further purified by means of column chromatography to separate fullerenes of different size[60]. The availability of gram-scale quantities of fullerene resulted in a great stimulus to research on such carbon nanostructures[58].

### 3.1.1 Structure of $C_{60}$ fullerene

$C_{60}$ fullerene, also known as buckminsterfullerene or buckyball, is the most common type of fullerene (Figure 3.1). All carbon atoms are in equivalent positions, at about 3.55 Å from the center of the molecule, at the vertices of a truncated icosahedron. The molecule has 20 hexagonal and 12 pentagonal faces, in agreement with Euler's theorem, and each pentagon is only surrounded by hexagons. This characteristic is the reason why $C_{60}$ is the easiest to produce among all fullerene molecules: it is the smallest fullerene in which two pentagons are not adjacent, which causes instability in the

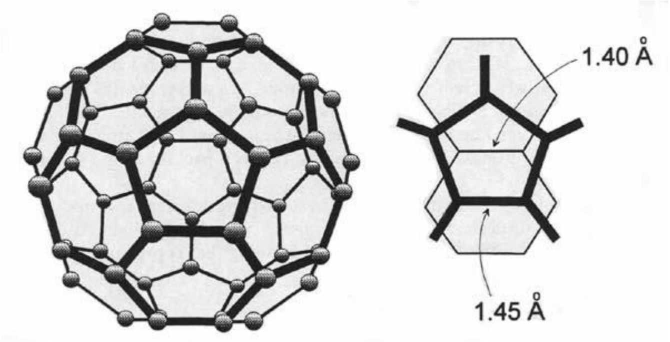

Figure 3.1: $C_{60}$ fullerene molecule and bonds between carbon atoms[62].

molecule due to tensile stress[61]. Fullerene molecules are characterized by the absence of a well defined hybridization of orbitals, unlike what happens in graphite ($sp^2$ hybridization) or diamond ($sp^3$ hybridization), because bonding of atoms between two hexagons are stronger than those between a pentagon and a hexagon. In particular, the four valence electrons of each carbon atom form an electronically richer bond between two hexagons. This also causes different distances between atoms, which are of 1.45 Å between a pentagon and a hexagon and 1.40 Å between two hexagons(Figure 3.1). $C_{60}$ molecule belongs to the icosahedral symmetry group $I_h$ and is invariant for 120 symmetry operators, thus being one of the molecules with the highest symmetry[58].

$C_{60}$ molecules are held together by weak van der Waals forces, forming a molecular solid. Crystal structure is face centered cubic (Figure 3.2(a)) with lattice constant 14.17 Å and distance between centers of first neighbour molecules equal to 10.02 Å. A consequence of the nearly-spherical shape of molecules and weak forces between molecules, is the capability of each $C_{60}$, above a critical temperature of 260 K, of rotating with three different degrees of freedom (Figure 3.2(b)); this property makes fullerene a plastic crystal. Below the critical temperature, the crystal structure becomes simple cubic, two rotational degrees of freedom are quenched and each of the four molecules in the unit cell revolves around a different $\langle 111 \rangle$ axis. This is due to a partial orientation of molecules, in which electronically richer bonds in a molecule (hexagon-hexagon) align with electronically weaker ones (pentagon-hexagon). Molecules completely stop their rotation under 90 K; however, molecules still fail to achieve a complete alignment, since they are in a cubic cell, non compatible with the icosahedral symmetry of each molecule, lacking 4-fold symmetry axes. This characteristic is named merohedral disorder[58].

### 3.1.2 Structure of $C_{70}$ fullerene

During the synthesis of $C_{60}$, higher order fullerenes are also formed, $C_{70}$ being the most abundant. $C_{70}$ are shaped as elongated $C_{60}$s, and can be seen as a

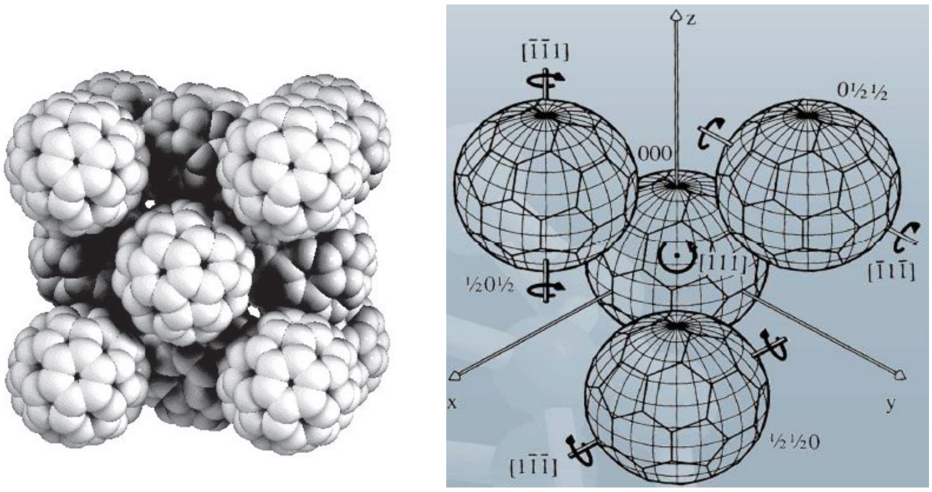

(a) (b)

Figure 3.2: (a) Crystal structure of $C_{60}$[63]; (b) Merohedral disorder[62].

$C_{60}$ with an additional ring of 10 carbon atoms around the equatorial plane of the molecule (Figure 3.3(a)). $C_{70}$ has a $D_{5h}$ symmetry, which is a subgroup of $I$, thus having less symmetry than $C_{60}$. $C_{70}$ crystal structure is more complex than that of $C_{60}$. At temperatures higher than 340 K, $C_{70}$ molecules are packed in a *fcc* structure with lattice constant of 15.01 Å with freely rotating molecules. Below 340 K, crystal structure is *hcp* with $a$=$b$=10.11 Å and $c/a$ of 1.82 (Figure 3.3(b)); this larger $c/a$ ratio is due to the orientation of the molecules along their longer axis, and rotation is limited to the 5-fold axis of the molecule. Below 280 K, the rotation along the 5-fold axis is also frozen, and the structure becomes monoclinic.

### 3.1.3 Electronic properties

Since van der Waals forces between fullerene molecules are considerably weaker than covalent bonds between atoms, the electronic structure is expected to be strongly related to the electronic levels of the single molecules. The electronic states of fullerene molecules are closely related to the number of electrons involved in $\pi$ bonds. In a $C_{60}$ molecule, a total of 240 electrons are present, 180 of which forming $\sigma$ bonds and 60, exactly one per atom, forming $\pi$ bonds. Such electrons are exactly the number needed to fill the molecular orbitals up to saturation of the highest energy occupied molecular orbital (HOMO), which has an icosahedral symmetry $h_u$ and is 5-fold degenerate. The first unoccupied molecular orbital (LUMO) is 3-fold degenerate (Figure 3.4) and has a gap from the HOMO of 1.68 eV[64]. In the crystal, the symmetry of the molecule is reduced by the crystal field, which eliminates orbital degeneracy. Electronic bands result from the superposition of molecular orbitals, and are

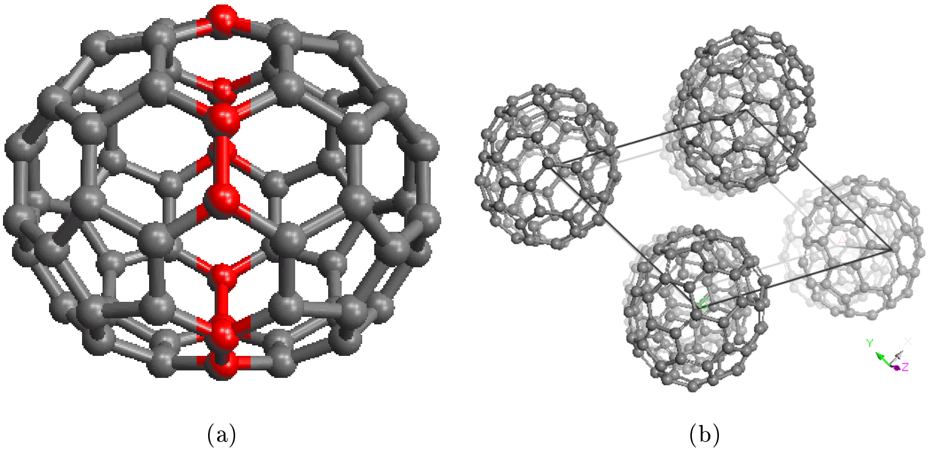

Figure 3.3: (a) $C_{70}$ molecule. The red atoms are the extra carbon atoms, with respect to a $C_{60}$ molecule; (b) Crystal structure of $C_{70}$ at room temperature.

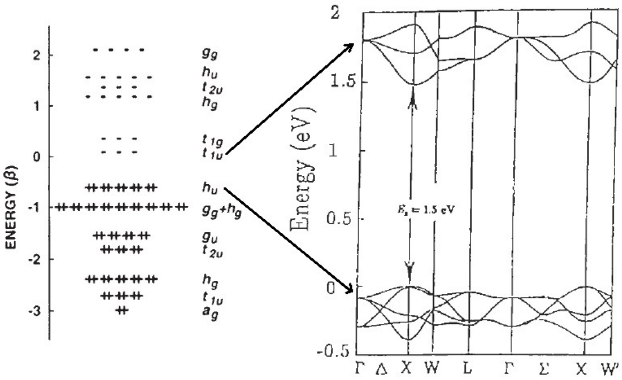

Figure 3.4: Energy levels for $C_{60}$ molecule and band structure for the crystal. Both are calculated by local density approximation[58].

similar to the energy levels of the single molecule; however, energy gap is reduced to 1.5 eV (Figure 3.4), thus making the crystal a semiconductor with a large energy gap[58].

$C_{70}$ molecules are similar to $C_{60}$, with a slightly higher HOMO-LUMO gap of 1.76 eV[64], and $C_{70}$ is also a large gap semiconductor, with a bandgap of about 1.75 eV[65].
Fullerene molecules are highly electronegative, and can accept up to six electrons in LUMO orbitals, till their complete filling. Moreover, fullerene crystal structure is characterized by large voids between molecules. $C_{60}$'s *fcc* crystal structure presents an octahedral and two tetrahedral empty sites, and thanks to the large lattice parameter, those interstitial voids are quite bulky (a di-

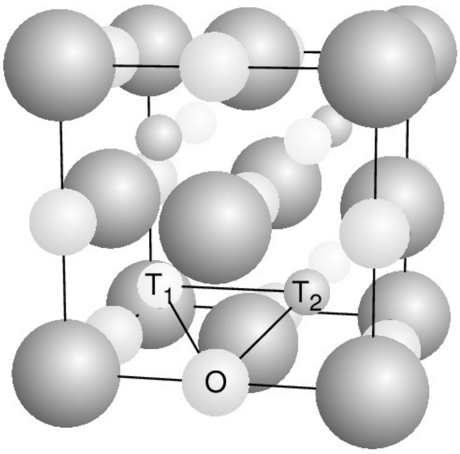

Figure 3.5: Interstitial voids in *fcc* crystal structure[67].

ameter of 2.44 Å for the tetrahedral sites and 4.14 Å for the octahedral site are estimated)[66](Figure 3.5). These characteristics make fullerene's crystal structure ideal to host small, electron-donor atoms. The insertion of one or more atoms in the voids is named intercalation, and products of such process are called intercalated fullerides[58].

### 3.1.4 Intercalated fullerides

Elements that are more easily intercalated in fullerere crystal are alkali metals and alkali-earth metals, thanks to their small ionic radius and low electronegativity, and thus tendency of donating electrons to form charge transfer salts. In the case of alkali metals, one electron per atom is forfeited, while alkali-earth metals donate two electrons per atom. Moreover, for some of the elements with smaller radius, like lithium and sodium, it is possible to intercalate metal clusters with partial charge transfer[22]. Some typical configurations of intercalated fullerides are shown in Figure 3.6.

With the presence of intercalated ions, and their electrons in the LUMO band, a metallic behaviour would be expected for all fullerides with a number of extra electrons lower than 6, which is the number of electrons needed to fully populate the LUMO orbital. However, it is not so easy to predict electronic behaviour of intercalated fullerides, due to other, more complex effect such as interactions between electrons, which cause some of these systems to be Mott insulators, or Jahn-Teller effect, which causes geometrical distortions in the molecules and solves the degeneration of the LUMO orbital. It was proven that many fullerides are in fact insulators or semiconductors[63].

A surprising property of $C_{60}$ molecules is that they can, in certain conditions,

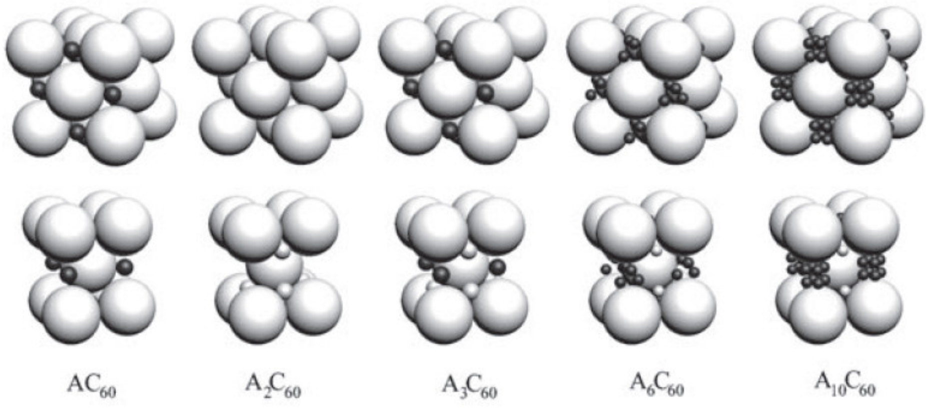

Figure 3.6: Alkali metal ions in intercalated fullerides[63].

form covalent bonds between each other. This is normally not viable at room temperature between neutral molecules, but it is allowed between ionized molecules, which can be obtained via charge transfer in intercalated fullerides. This phenomenon was first observed in $KC_{60}$ compound, in which a distance between first neighbour molecules of 9.1 Å, lower than the diameter of each molecule, was measured: covalent bonds effectively reduce distance between molecules in the direction of the bonds. The most frequent polymerization involves the formation of a ring of 4 carbon atoms, but also single bonds C-C were observed. $AC_{60}$ (A=K,Rb,Cs) compounds are known to form fullerene chains, with two C-C bonds between two molecules (Figure 3.7 (a)), and in $NaAC_{60}$ compounds single C-C bonds are observed (Figure 3.7 (b)). $Li_4C_{60}$ and $Mg_2C_{60}$ compounds are characterized by planar structures in which two C-C bonds join two molecules in one direction and a single C-C bonds in the other (Figure 3.7 (c)), while in $Na_4C_{60}$ the planar structure is held together by single C-C bonds in both directions. This last class of planar compounds have a body centered monoclinic structure[63]. Recently, such intercalated fullerides have attracted some attention due to their capability of being ionically conductive. In particular, two intercalation compounds are known as solid electrolytes: $Li_4C_{60}$ and $Mg_2C_{60}$, with ionic conductivity respectively of $10^{-2}$ S $cm^{-1}$[36] and $5 \cdot 10^{-5}$ S $cm^{-1}$ at room temperature[37].

### 3.1.5 Fullerene as battery electrode

Most lithium-ion batteries (LIB) have anodes based on graphite, which can electrochemically intercalate lithium with a theoretical capacity up to 372 mA h $g^{-1}$[20]. However, such material is not able to intercalate so well sodium and magnesium. For sodium, barely a stoichiometry of $NaC_{64}$ is allowed, corresponding to 35 mA h $g^{-1}$[16], not enough to serve as a battery anode. For magnesium it is even harder to obtain an intercalation compound with

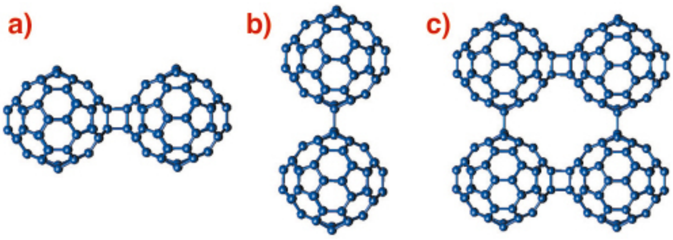

Figure 3.7: Polymeric structures in $C_{60}$ compounds: (a) ring-shaped pair of C-C bonds; (b) single C-C bond (c) planar structure with both types of bonds[68].

graphite, probably due to its high ionization potential. Only a few examples of magnesium-graphite compounds were obtained, and always using co-intercalation methods, in which an intercalation compound of graphite with other elements acts as an intermediate step for intercalating magnesium[17]. It has been proven that lithium can be electrochemically intercalated in fullerene up to $Li_{12}C_{60}$[69]. Moreover, sodium can be chemically intercalated in fullerene up to 11 sodium atoms per fullerene molecule[22], and magnesium up to 5 magnesium atoms per fullerene[23]. This is due to the large interstitial void in fullerene crystal structure and to the tendency of fullerene to accept electrons; hence fullerene seems to be a good candidate as anode in sodium-ion or magnesium-ion batteries. Moreover, electrochemical intercalation of fullerene with magnesium has already been observed, with a specific capacity up to 50 mA h $g^{-1}$[70], which led to a Toyota patent in 2013[26].
In addition to fullerene, during this study two fullerene-related materials were investigated: fullerene mixture and hydrogenated fullerene. In both cases, the aim was that of tuning some properties of fullerene structure, in order to better host metallic ions, and in particular to modify the steric hindrance of the molecules, thus obtaining larger empty spaces between molecules, to change electronic properties of the molecules, and to hinder polymerization between fullerene molecules, which prevents ion extraction after the first cycle.

### Hydrogenated fullerene

Fullerene molecules can be hydrogenated by reaction with $H_2$ at high temperature, producing a compound known as hydrogenated fullerene or hydrofullerene. Hydrogen atoms attach in pairs to carbon by breaking the electron-rich hexagon-hexagon bonds, thus creating a couple of covalent C-H bonds; as a consequence, only an even number of hydrogen atoms can be attached on a fullerene. The most stable hydrofullerenes are $C_{60}H_{18}$ and $C_{60}H_{36}$. Despite some stoichiometries are more stable than others, it is not possible to obtain a homogeneous disposition of hydrogen atoms on the fullerene molecule, and hydrofullerene sotichiometries always refer to a mixture of isomers (Figure 3.8(a)). Hydrogenation of fullerene reduces the symmetry of the molecules, and can modify the crystal structure: for low hydrogenation levels, fullerene's

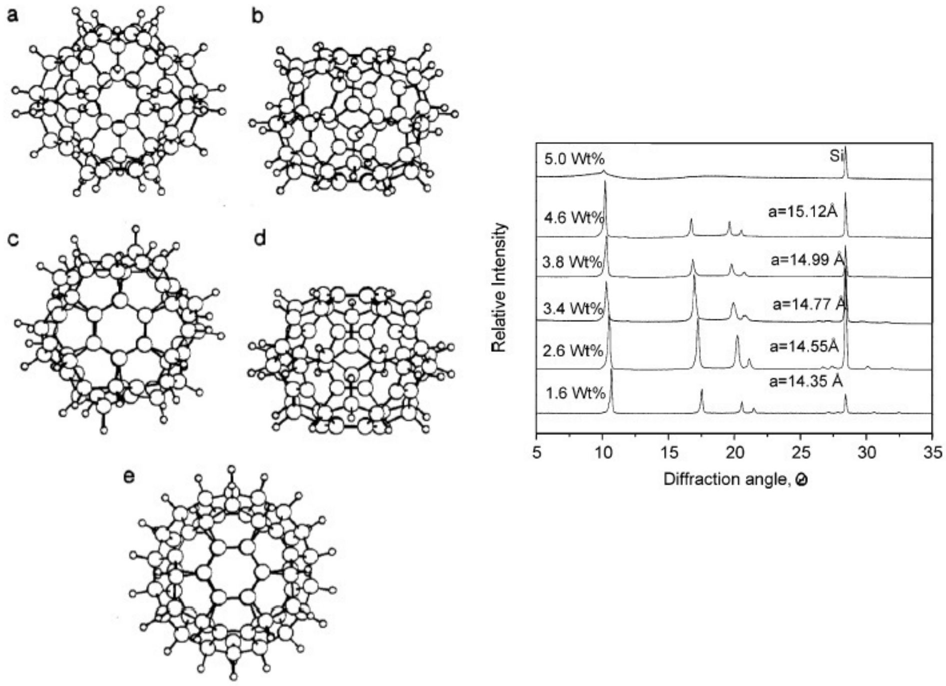

(a) (b)

Figure 3.8: (a) Three possible $C_{60}H_{36}$ isomers: a - $T_h$ in the direction of $c_3$ axis; b - $C_{3i}$ orthogonal to $c_3$ axis; c - $C_{3i}$ in the direction of $c_3$ axis; d - $D_{3d}$ orthogonal to $c_3$ axis; e - $D_{3d}$ in the direction of $c_3$ axis[72]. (b) x-ray diffraction pattern for samples with different hydrogenation level[71].

structure remains face-centered cubic, with increasing lattice constant, up to 15.12 Å (Figure 3.8(b)). After further hydrogenation, structure becomes body-centered cubic; lastly, higher hydrogenation levels can result in an amorphous system[71][72].

The increase of first neighbour distance between fullerene molecules, resulting from hydrogenation, can increase also the volume of the voids between the molecules, which could enhance the capability of hosting ions. It has been observed that hydrogenation can increase the capability of intercalating lithium ions up to a first discharge capacity of 1100 mA h $g^{-1}$, although a considerable loss of reversibility was also observed[20].

## 3.2 Graphene

Graphene is defined as a single layer of carbon atoms packed in a hexagonal, honeycomb-like 2D lattice. It can also be described a single layer of graphite, since the latter is a 3D arrangement of graphene layers stacked onto each other. First studies of graphene date back to 1947, when theoretical calculations were performed in order to better understand electrical behaviour of graphite. However, it was believed, based on theoretical predictions, that no 2D solid structure was possible at finite temperatures, because thermal fluctuations would cause the melting of the crystal. Single- or few-layer graphene was synthesized by epitaxial growth on substrates, but the interaction with the substrate would alter the electronic properties of graphene. Standalone graphene was first produced in 2004 by Geim and Novoselov via mechanical exfoliation, by cleaving the surface of graphite with an adhesive tape. The two scientists were awarded the Nobel Prize in Physics in 2010, for their discovery of the exotic electronic properties of graphene[29].

### 3.2.1 Graphene structure

Graphene is defined as a "single-atom-thick sheet of hexagonally arranged, $sp^2$-bonded carbon atoms that is not an integral part of a carbon material, but is freely suspended or adhered on a foreign substrate"[73]. Its thickness is about 0.34 nm, and its theoretical specific surface area is 2630 $m^2$ $g^{-1}$. It has been said before that perfectly flat single layer crystal should not exist; in fact, graphene is actually a not perfectly flat surface, but it is characterized by ripples and curvatures on its surface; such imperfections help stabilize graphene structure. This phenomenon becomes weaker when the number of layers increases, and just combining two layers of graphene is enough to obtain a much flatter surface[29].

### 3.2.2 Electronic properties

Graphene electronic properties are unique: valence and conduction bands of graphene have a single intersection point, called the Dirac point, making graphene a zero-gap semiconductor (Figure 3.9). At the Dirac point, charge carriers have an effective mass equal to zero, and are characterized by an astonishingly high mobility, up to 200 000 $cm^2$ $V^{-1}$ $s^{-1}$ for high quality graphene. Such high mobility determines a ballistic behaviour of the carriers up to the micrometer scale at room temperature. This also determines the possibility of observing quantum Hall effect even at room temperature. The electrons in graphene behave like relativistic particles, or massless Dirac fermions; as a consequence, they are described by the Dirac equation rather than the Schroedinger equation, the latter describing the electronic properties of conventional solids. Therefore, graphene is a good probe for relativity theory and quantum electrodynamics[29].

Graphene charge carriers have another important characteristic: they can be either electron or holes depending on the gate potential. This is due

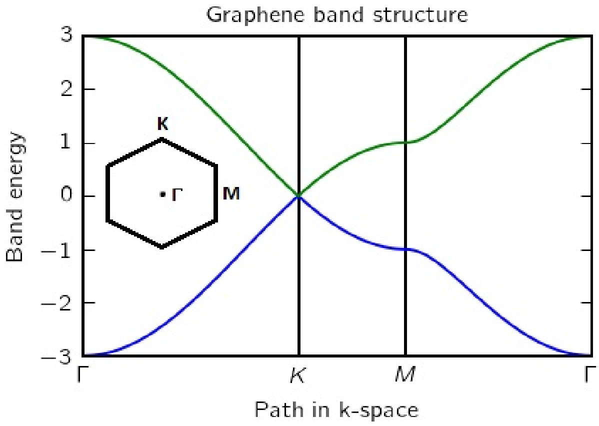

Figure 3.9: Band structure of graphene[74]. Inset: first Brillouin zone.

to the fact that Fermi level is exactly at the level of the Dirac point, and supplying a negative potential has the effect of dropping the Fermi level below the Dirac point, populating the valence band with holes; on the contrary, a positive potential raises the Fermi level above the Dirac point, populating the conduction band with electrons. This exotic characteristic is called ambipolar electric field effect. Such chiral nature of charge transport in graphene has a curious consequence, called Klein tunneling: the probability for an electron to overcome a potential barrier of any size is 100%. This means that graphene is not suitable to make most electronic devices based on semiconductors, since any potential barrier is completely ineffective[29]. In order to realize functional graphene-based electronics, increasing the energy gap to a non-zero value is needed; this can be achieved by doping graphene with heteroatoms, or by increasing the number of layers of graphene. For example, graphene energy gap can be finely tuned by adding B or N heteroatoms[75], or by synthesizing bilayer graphene[76].

### 3.2.3 Graphene as battery electrode

Thanks to its high specific surface area and good conductivity, graphene is an appealing candidate for energy storage applications. Graphene is currently studied in LIB, in order to solve issues like poor conductivity and slow ion diffusion in the electrode materials. It has been proposed as a high-capacity anode itself[21] or as a conductive agent to improve electrochemical performance of well-known electrode materials[77]. Graphene-based anodes can achieve specific capacities up to 1200 mA h $g^{-1}$[27]; metal oxide nanoparticles, which usually have low conductivity, can exploit a graphene matrix to increase their capacity, as for example in a hybrid graphene-Manganese(II,III)oxide ($Mn_3O_4$) material, in which capacity can grow up to 730 mA h $g^{-1}$, as opposed to the 300 mA h $g^{-1}$ of bare $Mn_3O_4$[78]. Metal oxides can also be graphene-coated, in order to improve their performance by exploiting the extra capacity provided by surface graphene, as for graphene-coated lithium iron phosphate ($LiFePO_4$), in which a capacity increase of 30% was observed[79]. Another possible application of a graphene network is to improve mechanical properties of materials. It is known that a high capacity electrode candidate for novel LIB is silicon, which has the disadvantage of high volume changes when charging and discharging, causing mechanical stress, cracks and loss of electronic contact, which damage the electrode. Graphene has been used as a conductive matrix to host silicon nanoparticles, dampening mechanical stress and reducing charge transfer resistance by 50%[80].

### Thermally exfoliated graphite oxide

Despite many different methods have been proposed for the synthesis of graphene, production of large quantities of graphene is still challenging. Methods for the production of high quality graphene are typically expensive and have a low yield; in fact, only a few methods are applicable for industrialization and commercialization. Synthesis of graphene can be divided in two major categories: top-down and bottom-up. Top-down methods employ graphite as starting material and consist in exfoliation of the different layers, while bottom-up methods use carbon-based precursors to chemically synthesize graphene. Mechanical exfoliation is a top-down method which produces the highest quality graphene, with nearly perfect atomic structure, but has an impratically low yeld. Some examples of bottom-up methods are epitaxial growth and chemical vapour deposition (CVD). Graphene can be grown with an epitaxial method by decomposing the surface of an oriented silicon carbide (SiC) substrate. Typically, an atomically flat (0001) face of a single-crystal SiC is treated at 1000 °C under ultra-high vacuum: silicon atoms sublimate, leaving graphene layers on the SiC substrate. CVD can be achieved by decomposing a precursor gas or vapour, for example methane ($CH_4$), on a proper substrate, the more convenient being copper, thanks to its ability to self-limit growth of graphene to a single layer. Epitaxial growth and CVD have the advantages of a large, continuous area of graphene, and more repeatability as compared to mechanical exfoliation, but they suffer a low yield and some difficulties in removing the substrate[29].

A top-down, highly scalable method for producing graphene is represented by exfoliation, and subsequent reduction, of graphite oxide. Graphite oxide (GO) consists in the product of a process during which oxygen-containing functional groups are attached to carbon atoms in graphite, resulting in an increase in distance between graphite layers, as well as a substantial decrease of the interaction between layers. Oxidation can be achieved through different methods, the most notable of which are the Brodie method, the Staudenmaier method, and the Hummers' method, all of which adopt strong acids and oxidants. Exfoliation is the next step required to obtain graphene, and can be achieved mainly by two routes: liquid phase exfoliation or thermal exfoliation. Liquid exfoliation consists in the dispersion and subsequent ultrasonication of GO in a proper solvent, during which GO layers are detached from each other. After exfoliation, reduction of graphene oxide is necessary; after liquid phase exfoliation this is typically achieved through chemical reduction, obtained by using a strong reducing agent, as for example hydrazine. Thermal exfoliation consists in heating GO at high temperatures, which determines the decomposition of oxygen-containing functional groups, which results in their detachment from graphite layers. When the rate of decomposition is higher than the rate of diffusion of oxygen in graphite, which can be achieved by abruptly raising temperature, pressure between GO layers can also detach the layers from each other. After thermal exfoliation, no reduction process is needed, since the high temperature treatment also yields the release of oxygen groups. The main advantages of exfoliation of graphite oxide is the high yield, while the main disadvantages are a higher defectivity: graphene produced via liquid phase exfoliation can be polluted by atoms or functional groups from the reducing agents, for example nitrogen for hydrazine, which get covalently bonded to the surface of graphene; graphene produced from thermal exfoliation can have vacancies of carbon atoms, detached as carbon monoxide during thermal treatment. In addition to this, thermal or chemical reduction of GO never completely get rid of all oxygen, and some of it is still attached to graphene after the treatment[29].

For my study, graphene samples, hereby referred as thermally exfoliated graphite oxide (TEGO), were obtained by thermal exfoliation of graphite oxide. Graphite was oxidized via Brodie method, and exfoliated at high temperature under vacuum. TEGO was chosen due to the scalability of the synthesis method, and a lower concentration of contaminants with respect to liquid phase exfoliated graphene. Some earlier studies on TEGO demonstrated that it is a good performer in LIB[21]. TEGO is characterized by domains of few layer graphene, with a number of layers variable from 1 to 5, surrounded by domains of amorphous carbon and residual graphite oxide (Figure 3.10)[81].

Concerning graphene, the aim of this study was to better understand the intercalation/de-intercalation mechanisms of lithium in TEGO, as well as realizing and characterizing lithium-ion full cells with graphene-based anodes and cathodes based on well established and commercially available materials, in order to make a step further towards commercialization of graphene batteries. A derivative of TEGO, obtained from a functionalization with hydrogen, hereby referred as H-TEGO, was synthesized and characterized as well. H-TEGO is obtained by high temperature reaction of TEGO with hydrogen, which operates a twofold modification: a reduction of the leftover

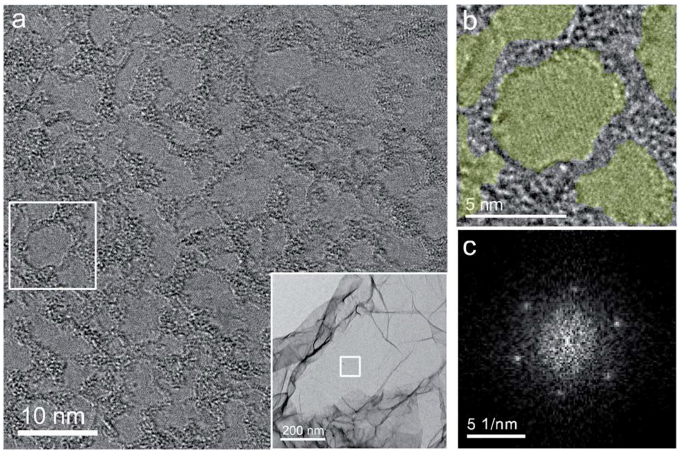

Figure 3.10: High-resolution transmission electron microscopy image of TEGO (from the flat region indicated in the inset). Graphene domains, surrounded by a network of amorphous carbon and residual GO, is visible. (b) Zoom of the region indicated in (a), in which graphene domains (mostly single layers) are highlighted in green. (c) Fast Fourier Transform of a graphene domain, with sharp 1100 spots proving ordered hexagonal graphene pattern[81].

oxygen, so that it is removed from TEGO, since the presence of oxygen could compromise the health of the battery, and bonding of hydrogen atoms to the surface of graphene, which could saturate possible dangling bonds on TEGO, derived from the removal of carbon atoms during thermal exfoliation. After the hydrogenation treatment, hydrogen on TEGO reaches 0.69%[82].

## 3.3 Solid electrolytes

Electrolytes are materials in which electrical conduction is carried by ions instead of electrons; for this reason they are also called ionic conductors. The electrolytes that are most commonly employed in batteries are salts in which ions are dissociated, once dissolved in an organic solvent. Such materials are one of the main environmental concern about batteries, since they can be toxic or hazardous, and thus need to be properly disposed. Electrolytes can also leak out of the battery, due to factory defects, shocks, bad storage conditions or usage at high temperature; moreover, electrolytes are air sensitive and must be stored and packed under inert atmosphere. An interesting alternative to conventional electrolytes is represented by solid ionic conductors (also known as solid electrolytes), a class of materials which has yet to be commercialized, since their ionic conductivity at room temperature is typically lower than that of liquid electrolytes. In solid electrolytes, conductivity is allowed by the capability of ions of hopping from their position in the crystal lattice to an empty site nearby. Such process is temperature-dependent and has an Arrhenius behaviour; it requires the overcoming of a potential barrier $E_a$

(activation energy), corresponding to the energy needed for hopping from one site to the next one[83]:

$$\sigma(T) = \sigma_0 \ e^{-\frac{E_a}{K_B T}} \tag{3.1}$$

where $\sigma$ is the ionic conductivity and $\sigma_0$ coefficient is a constant which is equal to the saturation conductivity, which means the conductivity when hopping is activated for all charge carriers.

Typical advantages of solid electrolytes are the possibility of operating at higher temperature, possibility to be tailored in a well-defined shape, so there is no risk of leaks and no need for a separator, and a good chemical stability, sometimes even in air, which results in less danger. The main disadvantages are the need of operating at higher temperatures, a lower ionic conductivity, and a lower interfacial contact between electrode and electrolyte; for these last two reasons, batteries made with solid electrolytes are also bound to be charged and discharged at lower rates. Despite the fact that all solid-state batteries have yet to be commercialized, research on solid electrolyte is highly active, and different classes of ionic conductors are being studied. Complex metal hydrides, like $MAH_4$ (M=alkali metal, A=Al,B) compounds, for example lithium borohydride ($LiBH_4$), are characterized by a fast ionic conductivity up to $10^{-3}$ S cm$^{-1}$, but only after a phase transition occurring at high temperatures (390 K for $LiBH_4$)[32]. Another class of solid electrolytes is represented by ceramic ionic conductors, for example $Li_{1.4}Al_{0.4}Ti_{1.6}(PO_4)_3$[33], in which an ionic conductivity up to $10^{-3}$ S cm$^{-1}$ can be obtained, but with a difficulty to obtain good interfacial contact with the electrode[34]. Solid solutions of salts in certain polymers are also being studied: they are characterized by a good ionic conductivity after a phase transition from crystal to amorphous occurs; for example, in polyethylene oxide, an ionic conductivity up to $10^{-4}$ S cm$^{-1}$ is observed above 330 K[35]. Lastly, some intercalated fullerides feature an ionic conductivity; for example $Li_4C_{60}$[36] and $Mg_2C_{60}$[37] with room temperature ionic conductivities of about respectively $10^{-2}$ and $10^{-4}$ S cm$^{-1}$, although with a possible non-negligible electronic conductivity. In this study, solid electrolytes were synthesized and characterized. In some cases, they were also used in batteries, when a problem of solubility of anode materials in organic solvents emerged for fullerene-related materials, as also reported in [20].

### 3.3.1 Polyethylene oxide

Polyethylene oxide (PEO) is an amply studied material which forms solid solutions that can be ionically conductive. PEO, which is composed by the polymeric chains shown in Figure 3.11 (a), can dissociate salts as happens with liquid solvents. At room temperature, PEO has a monoclinic crystal structure, in which all the chains are ordered and aligned, and ionic conductivity is too low for battery purposes. Above a temperature of about 65 $^{o}$C, a phase transition to a vitreous state occurs, and chains become disordered[84]. In this phase, ionic conductivity can increase up to $10^{-3}$ S/cm, which is sufficiently high to be used as an electrolyte, although still 10 times lower than typical liquid electrolytes. Moreover, it was demonstrated that addition of certain ceramic nanoparticles, like alumina ($Al_2O_3$) or titania ($TiO_2$)[35], can hinder re-crystallization of PEO during cooling, effectively causing a hysteresis of ionic conductivity, which can be maintained at values of about $10^{-4}$ S cm$^{-1}$ even at room temperature[85].

### 3.3.2 Borohydrides

Borohydrides (as for example $LiBH_4$, $NaBH_4$) are a class of materials initially studied for their hydrogen storage properties. Such materials failed to meet the requirements for automotive hydrogen storage; however, the study of physical and chemical properties of borohydrides led to the discovery of the ionic conductivity in $LiBH_4$. The salt $LiBH_4$ is a orthorhombic crystal at room temperature, with a rather low ionic conductivity. It has been observed that above a temperature of 390 K, it undergoes a phase transition from orthorhombic to the ionically conductive hexagonal (Figure 3.11 (b)), in which ionic conductivity is $10^{-3}$ S cm$^{-1}$, three orders of magnitude higher than that observed at room temperature[32]. Following this discovery, it has been demonstrated that $LiBH_4$ composites with salts or anions can increase the mobility of ions in the crystal[86][87]. Recently, a $LiBH_4$-$C_{60}$ composite with improved ionic mobility has been synthesized: $C_{60}$ molecules are embedded in the crystal structure of $LiBH_4$, and are probably reduced by the latter, removing $Li^+$ from $LiBH_4$ and thus allowing $BH_4^-$ to react with $C_{60}$, which gains one hydrogen atom forfeited by $BH_4^-$[39]. However, reaction of $C_{60}$ with lithium ions can cause the formation of $Li_xC_{60}$ fullerides, and completely saturate the LUMO band of $C_{60}$, since the 50:50 weight ratio between $LiBH_4$ and $C_{60}$ determines a very high number of lithium ions per fullerene molecule. The complete filling of the LUMO band could hinder mobility of ions. In this study, $Li_xC_{60}$-$LiBH_4$ (x=4,6,12) composites were synthesized, in order to study the ionic conductivity of the such materials and determine if more free lithium ions in $LiBH_4$ give rise to a higher ionic conductivity. A high ionic conductivity has been observed even at low temperatures in composites between lithium fullerides and $LiBH_4$, as well as in a composite between a sodium fulleride and sodium borohydride ($NaBH_4$), despite the latter is not known for being an ionic conductor.

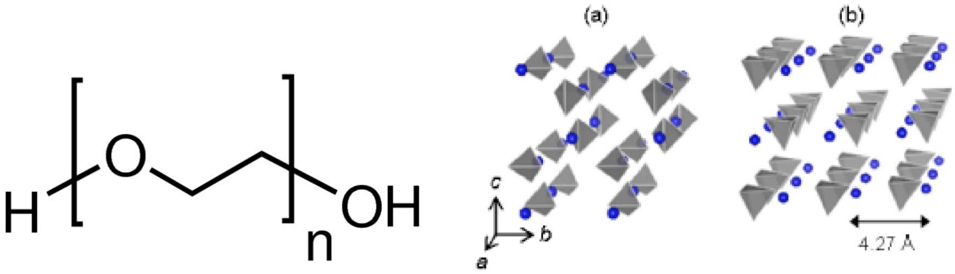

(a) (b)

Figure 3.11: (a) Polyethylene oxide. (b) Lithium borohydride[32].

## 3.4 Magnesium electrolyte

Realizing functional magnesium-ion batteries is more challenging than lithium- or sodium-ion batteries. One of the main problems hindering the effectiveness of magnesium electrochemical cells is the high reactivity of Mg; due to this, most magnesium electrolytes cause the growth of a passivating solid-electrolyte interphase (SEI) on the electrode-electrolyte interface, which, after a few charge and discharge cycles, completely blocks passage of magnesium ions from the electrolyte to the electrode, in contrast with behaviour of SEI in Li- and Na-ion batteries, in which passage of ions is allowed. The so-called Grignard reagents (RMgX, where R is an alkyl or aryl group, and X is Cl or Br) can form non-passivating electrolytes in combination with proper solvents; however, Grignard reagents are too reactive to be effectively used in batteries, since they are strong reducing agents. Some Grignard-derived organohaloaluminates salts, with formula $Mg(AlCl_3R)_2$ and $Mg(AlCl_2RR')_2$, where R and R' are alkyl groups, have been developed for their use in Mg-ion batteries in combination with a proper solvent. One of the most effective electrolytes of such family, which has been employed for this study, is $Mg(AlCl_2BuEt)_2$ in tetrahydrofuran (THF)[18].

## 3.5 Cathodes

Graphene-based anodes for lithium ion batteries have been coupled to three different well known cathodes: lithium cobalt oxide ($LiCoO_2$, referred as LCO), lithium nickel manganese cobalt oxide ($Li_xNi_yMn_zCo_{1-y-z}O_2$, with variable Ni:Mn:Co ratio, referred as NMC) and lithium iron phosphate ($LiFePO_4$, referred as LFP). LCO is the first high potential (vs $Li/Li^+$) cathode ever commercialized; it was developed by SONY in 1990 and its working principle involves the insertion of lithium, balanced by the $Co^{3+}/Co^{4+}$ redox reaction[5]. LCO is characterized by a face-centered cubic packing of oxide ions, with space group $r3m$, in which lithium ions are located in the octahedral sites forming a layered structure, with alernating sheets of $Li^+$ cations and $CoO_2^-$ anions. Average operating voltage of LCO is 3.6 V, and specific capacity is 150 mA h $g^{-1}$[88]. The advantage of LCO is a high specific energy, due to its high potential vs $Li/Li^+$, but with the disadvantage of a short lifespan, low thermal stability and danger when charging or discharging at a high C-rate, as well as problems related to the use of cobalt, which is expensive and toxic[40]. Moreover, cobalt has been classified by the European Union as one of the critical raw materials, since it is mostly found in mines in politically sensitive regions[89].

The first alternatives to LCO that have been investigated are $LiNiO_2$ and $LiMnO_2$. Sadly, both structures are unstable upon lithium extraction: in $LiNiO_2$ nickel ions tend to occupy lithium sites, while in $LiMnO_2$ a structural transition occurs from layered to spinel sctructure; in both cases lithium insertion is hindered after the first cycle. Combination of the three cations has led to the development of NMC, in which cobalt ions stabilize the structure upon lithium extraction. Many different compositions exist, the first and most studied being being Ni:Mn:Co=1:1:1; recently, Ni:Mn:Co=8:1:1 is also being studied, in order to reduce the amount of cobalt[5]. As LCO, NMC is known for its high specific energy, again due to a high potential vs $Li/Li^+$, and for a lower cost with respect to LCO, since content of the expensive cobalt is lower, but with a slightly lower voltage. It is also safer than LCO, and has faster charge/discharge capabilities, deriving from its lower internal resistance[40].

LFP has an olivine structure, in which the close-packed hexagonal crystal hosts lithium and iron ions in half of the available octahedral sites, while phosphorus ions occupy one eighth of the tetrahedral sites. The octahedral sites have two different sizes, and since lithium and iron have different sizes, they occupy different octahedral sites, so the crystal is characterized by an ordered cationic distribution[5]. LFP cathodes have the advantage of a higher charge and discharge rate, which is also expected in graphene-based anodes, and of being composed of safe and inexpensive elements. It also has the advantages of a good thermal stability, longer cycle life, and more safety if charged at a C-rate higher than nominal maximum or if left in a charged state for a long time. The main disadvantage is a much lower voltage (average 3.2 V vs $Li/Li^+$), with the consequence of a lower specific energy. Specific capacity is 170 mA h $g^{-1}$[40].

# Chapter 4

# Methods

## 4.1 X-ray diffraction

Most of the materials employed in this work are crystalline powders: ions, atoms or molecules are arranged in a well defined periodic structure. When studying electrode or solid electrolyte materials for ionic batteries, investigating such periodic lattice is useful to determine the relative positions of atoms and molecules and to evaluate possible structural transitions, which can be caused by changes in temperature or in the relative concentration of atoms, for example during intercalation. X-ray diffraction (XRD) is probably the most effective technique for studying crystal structure of materials, and is based on scattering, a physical phenomenon in which radiation, when crossing a medium, is deviated from its original trajectory. Electromagnetic radiation is typically scattered by electrical charges of atoms, mainly by electrons. XRD exploits scattering of X-rays, thanks to the fact that such electromagnetic radiation has wavelengths similar to the interatomic distances between atoms in a crystal lattice, of the order of magnitude of 1 Å, thus generating interference similarly to what happens to visible light through narrow slits. Scattering interactions between electrons and electromagnetic radiation can be divided into two categories:

- **Elastic scattering**: also known as Thomson scattering, it is a collision event in which the energy of each particle, referred to the frame of reference of their center of mass, is conserved. This implies that the wavelength of the scattered electromagnetic radiation is the same as that of the incident radiation. Such interaction is a coherent scattering, since a well defined relationship exists between the phase of the incident wave and that of the scattered wave.

- **Inelastic scattering**: also known as Compton scattering, it is a collision event in which the scattered electromagnetic radiation loses, or more rarely gains, any amount of energy with respect to the incident beam. The resulting variation of wavelength determines the loss of the relationship between the phase of the incident beam and that of the scattered beam, thus being an incoherent scattering.

In XRD, the interaction of interest is elastic scattering, since coherent radiation, contrarily to incoherent radiation, can give rise to interference. Atoms are centers of scattering for radiation, and the scattered beam from an ordered array of atoms, like those in a crystal, is characterized by an interference pattern, useful to study the interatomic distances and their relative positions[90].

A qualitative interpretation, useful to describe the constructive and destructive interference conditions of a scattered beam, was first developed in 1913 by W. L. Bragg, who considered diffraction as a consequence of reflection of the incident beam caused by a family of crystal planes, acting like semi-transparent mirrors equally spaced of a distance $d$ (Figure 4.1(a)). The difference of path between parallel beams reflected by neighbour planes is given by:

$$AB + BC = 2dsin\theta \tag{4.1}$$

and constructive interference condition is given by:

$$n\lambda = 2dsin\theta \tag{4.2}$$

with $n$ integer. Bragg's interpretation is empirical, and is based on the assumption that crystal planes are semi-transparent mirrors, which is not physically true. A more strict explanation was later given by M. von Laue. Considering a monochromatic beam, incident with an angle $\phi$ on a monodimensional lattice (Figure 4.1(b)), and a scattered angle $\psi$, constructive interference is given by:

$$a(cos\phi + cos\psi) = h\lambda \tag{4.3}$$

with $h$ integer. Intensity of scattered radiation is assumed zero for each $\psi$ not satisfying equation 4.3. Such condition gives rise to a family of cones, each with axis laying on the considered monodimensional lattice; each cone is defined by the integer $h$. For a 3-dimensional lattice, three equations, one for each different crystallographic direction, must be satisfied at the same time. Consequently, incident radiation is scattered only in the directions defined by the intersections of three cones, each with the axis laying on a different lattice vector (Figure 4.2)[90].

Switching to a vector notation, the system of three 4.3 equations can be written as:

$$\vec{R} \cdot \vec{s} = q \tag{4.4}$$

where $\vec{R}$=$n\vec{a}$+$m\vec{b}$+$p\vec{c}$ (with $n,m,p$ integers) defines the lattice of scatterers, $\vec{s}$ is the scattering vector, equal to the difference in wavevector between the scattered beam and the incident beam, and $q$ is an integer. This equation can also be rewritten as $\vec{s}$=$\vec{R}^*$, where $\vec{R}^*$ is a vector in the reciprocal lattice.

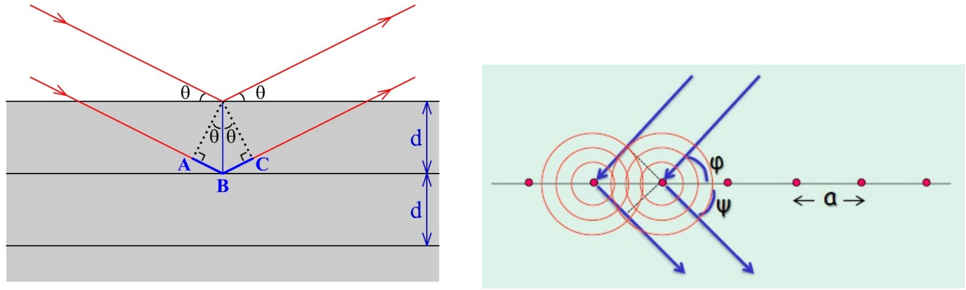

(a) (b)

Figure 4.1: (a) Bragg interpretation: beam reflected by semi-transparent mirrors; (b) Laue interpretation: beam scattered by a monodimensional lattice, in which each point is a new source of radiation.

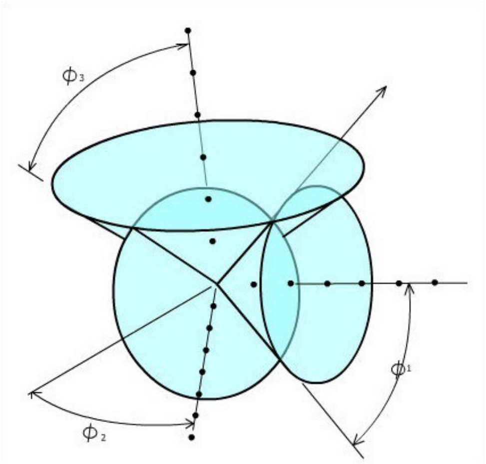

Figure 4.2: Laue cones intersections in three dimensions.

Therefore, from the constructive interference peaks, informations on crystal structure can be obtained[90].

Laue's explanation, formulated for ideal crystals, can be extended for real crystals, with some tweaks. For starters, atoms always vibrate around their equilibrium positions, and a correction, called Debye-Waller factor, is necessary. The consequence of lattice vibrations is a decrease of peak intensity. Another relevant experimental limit is that often single crystals are not available; it is possible to perform XRD on powders of crystalline materials, with the difference that diffraction peaks are not points but circumferences centered in the axis of the incident beam. Sadly, this determines a loss of information. The origin of the circle-shaped diffraction pattern can be explained by starting with a single crystal and adding more, one at a time: with each new crystal, orientations are more disordered, and each interference maximum is distributed in a random direction, yet remaining at the same distance from the axis of the incident beam (Figure 4.3). Due to the symmetric nature of this kind of data, it is easier to visualize the intensity of the the peaks as a function of the angular distance from the axis of the incident beam, called $2\theta$[90].

### 4.1.1 Powder X-ray diffraction

In a powder diffraction experiment, peak position depends on the unit cell, while intensity depends on symmetry and structure of the crystal; the shape of the peaks depends on instrumental factors and intrinsic sample conditions. In order to determine the structure of the crystal, it is necessary to index each diffraction peak, which means to determine the correspondence between peak position and unit cell symmetry, not counting atom position, which only intervene in peak intensity and are considered at a second step of XRD analysis. Lastly, peak profile is considered: profile depends both on instrumental factors (beam width, collimation quality, monochromaticity), which determine a gaussian-shaped peak, and sample factors (mainly crystallites dimension), which determine a lorentzian-like shape. One method, which allows to simultaneously optimize structure and profile parameters, to refine crystal structure starting from a powder XRD is the Rietveld method, and is based on minimizing difference between calculated and experimental data through the least squares method. Intensity of scattered beam is given by:

$$I(R^*) = M_{hkl} I_0 LPT |F_{hkl}(R^*)|^2 DW \tag{4.5}$$

where $M_{hkl}$ is a factor taking into account equivalent reflections multiplicity, $I_0$ is the incident beam intensity, $DW$ is the Debye-Waller factor, $F_{hkl}(R^*)$ is the structure factor, or the intensity scattered by the unit cell in each crystallographic direction, and $L$, $P$ and $T$ are corrections: $L$ is the Lorentz cor-

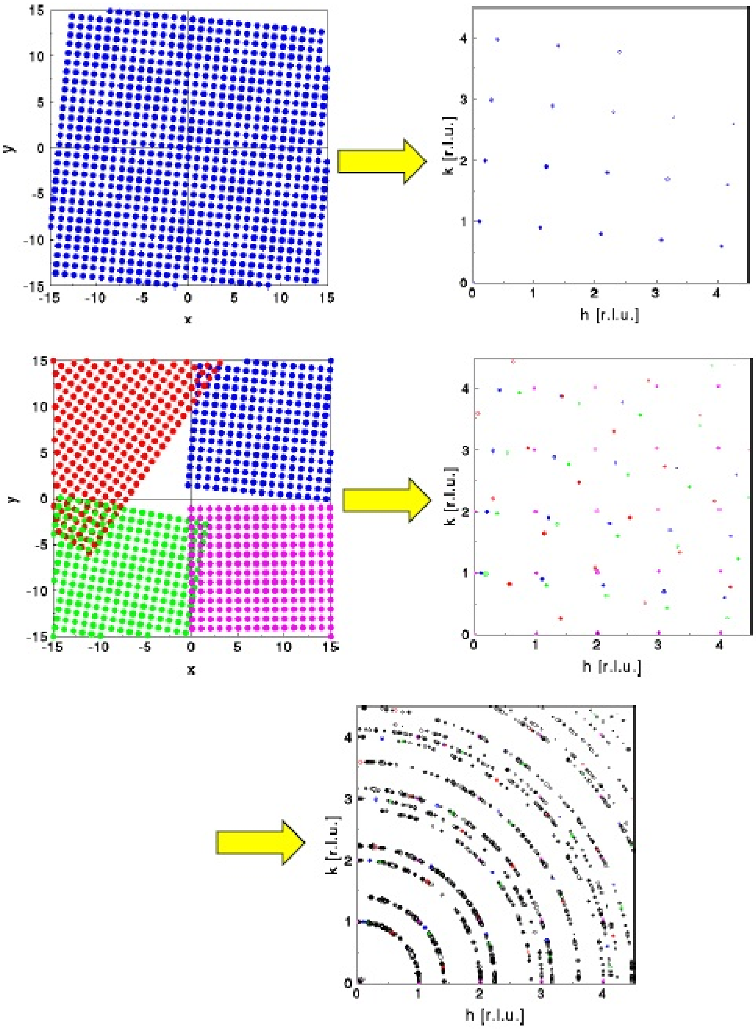

Figure 4.3: X-ray diffraction pattern with an increasing number of crystallites.

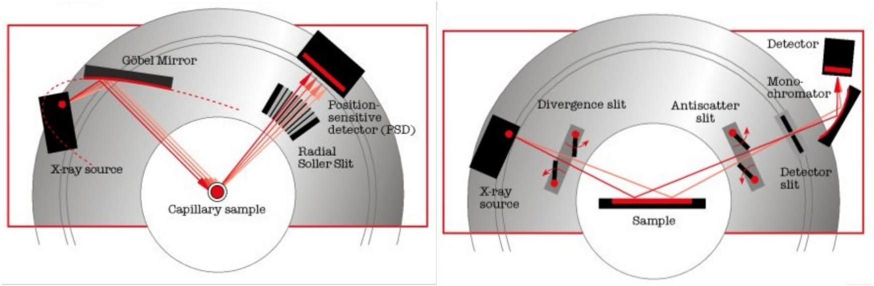

(a) (b)

Figure 4.4: (a) Debye-Scherrer geometry[94]; (b) Bragg-Brentano geometry[94].

rection, which accounts for the fact that the intensity measured by a detector with finite dimension is a fraction of the total intensity of the circumference, and that the measured fraction of the intensity decreases at higher angles; $P$ is a correction which depends on the polarization of the incident beam; $T$ is a correction which takes into account the sample's absorption of the incident and the scattered beams[91].

### 4.1.2 Experimental setup

Two different instruments were used for XRD, each conceived for powder experiments and equipped with an X-ray copper tube source, exploiting copper $K_\alpha$ radiation, with $\lambda$=1.54 Å. The first instrument is a Bruker D8 Discover, equipped with an area detector GADDS and two Göbel mirrors as monochromators, and operating in Debye-Scherrer geometry (Figure 4.4(a)). Samples were sealed in a glass capillary under argon atmosphere and rotated, thus reducing preferred orientations of crystallites during measurements. Bruker D8 was employed to perform powder XRD on pure $C_{60}$ and $C_{60}$-based electrodes after insertion of sodium[92].

The second instrument is a Bruker D2 Phaser, equipped with a Linxeye detector, operating in Bragg-Brentano geometry (Figure 4.4(b)). Samples were put on a zero-background silicon plate and rotated. When dealing with air-sensitive samples, a plexiglass, non-rotating airtight dome, closed under argon atmosphere, was employed. Bruker D2 was employed to perform powder XRD on $C_{60}H_x$-based electrodes before and after insertion of sodium, on mixture before and after high energy ball-milling, and on fulleride-borohydride composites[93].

## 4.2 Electrochemical impedance spectroscopy

Electrochemical impedance spectroscopy (EIS) is a powerful technique with many different uses. In this work, EIS was exploited to study the dynamics of charged particles inside a material or at the interface between two different materials: most electronic properties, as for example charge carriers diffusion, can be obtained from the response of the material to an alternate current. In particular, EIS is particularly effective for studying ionic conductivity and to discriminate the electronic and ionic contributions to the total conductivity. By applying a sine wave potential $V(t){=}V_{max}\sin(\omega t)$ with frequency $\nu = \frac{\omega}{2\pi}$, there will be a current response in the material $I(t){=}I_{max}\sin(\omega t{+}\theta)$, where $\theta$ is the phase difference between the applied potential and the measured current. In general, treating the system's response in the time domain is complex, since a solution to a system of differential equations is needed for the capacitive $I(t){=}\frac{dV(t)}{dt}C$ and the inductive $V(t){=}\frac{dI(t)}{dt}L$ response, where $C$ and $L$ are respectively capacity and inductance[95].

An easier method to treat data is possible by expressing the time-dependant equations in the frequency domains, by exploiting the Fourier transform; this way the previous equations become $I(j\omega){=}C\omega jV(j\omega)$ e $I(j\omega){=}\frac{V(j\omega)}{Lj\omega}$, where $j$ is the imaginary unit. It is then possible to define an impedance function $Z(j\omega)$ or simply $Z(\omega)$ so that the system's response to an alternating signal can be written similarly to Ohm's law:

$$I(j\omega) = \frac{V(j\omega)}{Z(j\omega)} \tag{4.6}$$

Capacitive and inductive response is respectively given by:

$$Z_C(j\omega) = \frac{1}{Cj\omega} \qquad\qquad Z_L(j\omega) = Lj\omega \tag{4.7}$$

Impedance in circuits with multiple elements can be obtained similarly to what happens for multiple resistors. Since $Z(\omega)$ is a complex function, it can be written as a sum of real and imaginary part[95]:

$$Z(\omega) = Z' + jZ'' \tag{4.8}$$

$$Re(Z) = Z' = |Z|cos\theta \qquad\qquad Im(Z) = Z'' = |Z|sen\theta \tag{4.9}$$

with phase angle $\theta$ and modulus respectively equal to:

$$\theta = arctan\left(\frac{Z''}{Z'}\right) \qquad\qquad |Z| = \sqrt{(Z')^2 + (Z'')^2} \tag{4.10}$$

### 4.2.1 Graphical representations

Expressing impedance as the sum of real and imaginary part allows more intuitive graphical representations:

- **Impedance representation**: values for real (Z') and imaginary (Z") parts are pictured as a function of frequency. Such representation can better emphasize characteristic frequencies in the system.
- **Nyquist representation**: also known as Cole-Cole or Argand plot, it consists in a representation in which data are shown in the complex plane, with Z' as abscissa and -Z" as ordinate. The advantage of such representation is that behaviour of the system can be easily understood by the shape of the Nyquist curve.
- **Bode representation**: values of $\theta$ and $|Z|$ are expressed as a function of frequency, usually in logarithmic scale. The advantage of such representation is that impedance behaviour at high frequencies is weighted equally to that at lower frequencies[95].

### 4.2.2 Models

Although it is quite hard to extrapolate electrical transport properties of a material directly from the response to an alternate potential, it is easier to understand such information by modelling the behaviour with an equivalent circuit, made of basic elements of macroscopical circuits, such as resistors, capacitors and sometimes inductors: resistors represent conductivities of different natures, while capacitors and inductors can model other processes, like local polarizabilities[95].

In a solid electrolyte, the parameter of interest is the ionic conductivity; for this reason the model must be suited to better understand the dynamics of ionic charge carriers. Our most basic systems consist of a solid electrolyte between two blocking, which means impermeable to the ions of the ionic conductor, stainless steel electrodes, to which a sine wave potential is applied; the simplest equivalent circuit to model such behaviour takes into account a resistance $R_i$, corresponding to ions crossing the electrolyte. It has been demonstrated[96], both theoretically and experimentally, that the effect of the interface between a solid electrolyte and a purely electronic conductor, which is an accumulation of ions at the metal/electrolyte interface, can be modelled as a simple series of a capacitor $C_{int}$ with the ionic resistance $R_i$.

A series of a resistance and a capacitor is not enough to model an ionic conductor. A geometric capacity must be added, due to the fact that the system, in which two metal electrodes are separated by a dielectric, behaves like a parallel plates capacitor. Such contribution, typically small but non-negligible, is modelled with a capacity $C_{geom}$, parallel to the series of resistance and capacitor, and is more effective at higher frequency; the model obtained is called "Debye circuit" (Figure 4.5(a)). The typical Nyquist plot for a Debye

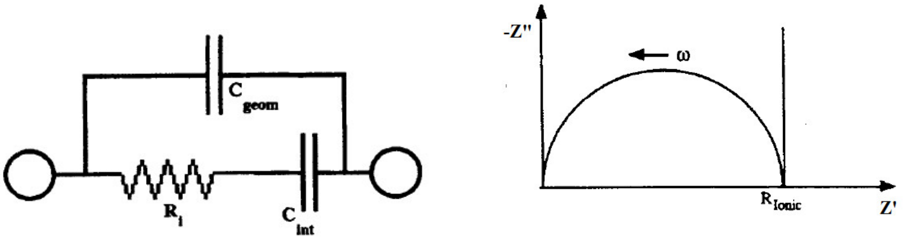

(a) (b)

Figure 4.5: (a) Debye equivalent circuit[97]; (b) Nyquist plot for a Debye equivalent circuit[97].

circuit is shown in Figure 4.5(b). Qualitatively, it is quite easy to understand such behaviour: at low frequencies the impedance of the capacitors $C_{geom}$ and $C_{int}$ is high and current flow is impeded. When the frequency increases, impedance of $C_{int}$ is lower than that of $C_{geom}$; consequently, current starts flowing through the series of $C_{int}$ and $R_i$, showing a vertical straight line, called "tail", typical of an ionic conductor. At higher frequencies the impedance of the capacitor $C_{int}$ decreases, and after a frequency threshold the capacitor behaves as a closed circuit, so the imaginary part of the impedance is zero and all the impedance is real and due to the resistance. The maximum of the semicircle is reached when the impedance of $C_{geom}$, also decreasing with higher frequencies, is equivalent to that of the resistance, so that current is equally divided between the two branches of the circuit[97].

It is frequent that a material is characterized by both an electronic and an ionic conductivity: in this case the system is well represented by an equivalent circuit with an electronic resistance $R_e$ parallel to the Debye circuit (Figure 4.6(a)). If the electronic conductivity is high, the corresponding Nyquist plot will not have the low frequency tail (as $C_{int}$ will become negligible); if electronic conductivity is lower than or of the same order of magnitude of ionic conductivity, the Nyquist plot will be characterized by two adjacent semicircles (Figure 4.6(b))[97]. Lastly, a resistance may be added in series to the aforementioned circuit in order to take into account the external resistance of the contacts[95].

Up to now, ideal circuit elements were considered. In reality, such elements can be considered ideal only in a limited frequency range. A resistance, for example, at very high frequency also behaves as a capacitor and an inductor, not counting that its response to a signal is always delayed due to its nonzero length. Two main differences exist between ideal and non ideal systems: finite dimension of samples, in contrast with point-like elements in an ideal

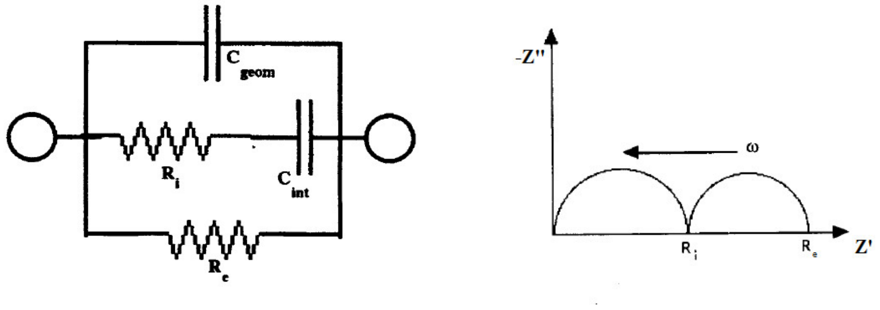

(a)

(b)

Figure 4.6: (a) Debye equivalent circuit for mixed conductivity, ionic and electronic[97]; (b) Nyquist plot for a Debye circuit with mixed conductivity[97].

circuit, and macroscopic dimension of the electrodes, which give rise to different conductivity channels, crossing the samples in different regions, which may be inhomogeneous. When probing the ionic conductivity of either a solid electrolyte or an electrode, the effect of inhomogeneities can be remarkable, since ion hopping implies the overcoming of a potential barrier, which can be strongly influenced by proximity differences. When ideal elements are not sufficient to model its impedance, it is necessary to employ distributed elements in equivalent circuits. The two most useful distributed circuit elements are the infinite-length Warburg element and the constant phase element[95].

The infinite-length Warburg impedance ($Z_{W\infty}$), first introduced in 1899, comes from the solution of the diffusion equation, Fick's second law, in one dimension for an infinite medium[95]. For real experiments, the finite-length Warburg impedance ($Z_W$), coming from the solution of the diffusion equation for a finite medium of length $l_e$, is more interesting:

$$Z_W = \frac{\sigma}{\sqrt{\omega}}(1-j)tanh(\sqrt{js}) \qquad s = l_e^2\frac{\omega}{D} \tag{4.11}$$

where $D$ is the diffusion coefficient and $\sigma$ is the Warburg coefficient, which may be easily derived from the slope of the imaginary part of the impedance (or the real part, since the slope should be the same) versus $\omega^{-1/2}$[98]. Diffusion coefficient is the given by:

$$D = \frac{1}{2}V_m^2\frac{\left(\frac{dE}{dx}\right)^2}{FA\sigma^2} \tag{4.12}$$

where $V_m$ is the molar volume of the compound in which the charge is diffusing and $\frac{dE}{dx}$ is the slope of the open circuit voltage curve[99]. When performing EIS on an electrochemical cell to study the diffusion of ions in the electrode, it is important to probe the system at different states of charge and discharge, due to the fact that the diffusion coefficient may be strongly dependent on the stage of intercalation.

Although diffusion is usually well described by a Warburg impedance, there are situations in which the Nyquist plot shows a tail with an angle different from 45°; in such cases, the frequency response of the real and imaginary parts of the impedance is proportional to $\omega^{\psi}$ and is modelled by the so-called constant phase element (CPE):

$$Z_{CPE} = \frac{1}{A_0 (j\omega)^{\psi}} \tag{4.13}$$

where $A_0$ and $\psi$ are frequency-independent, and $\psi$ can assume any values between 0 and 1; when $\psi$=1 $Z_{CPE}$ behaves like a capacitor, and when $\psi$=*0* it behaves like a resistor. Introduction of one or more CPE, usually in place of capacitors, is useful to make the model more effective, also to explain systems which present downcast or partially intertwined semicircles in the Nyquist plot[95].

### 4.2.3 Experimental setup

Impedance spectroscopy measurements were performed using either a HP 4192A impedance analyser, or a Gamry Interface 1010 potentiostat/galvanostat. When using the HP 4192A, an alternate signal of 0.1 V was applied, with frequencies ranging between 5 Hz and 13 MHz, while when using the Gamry interface 1010, an alternate current signal of C-rate 0.1 C was applied, with frequencies ranging between 5 Hz and 200 KHz. For each frequency, data was acquired as |Z| e $\theta$ and averaged on 7 measurements. HP 4192A was used to perform EIS on solid or gel electrolytes, while Gamry Interface 1010 was used to characterize lithium-ion batteries (LIB) based on graphene and derivatives.

## 4.3 Galvanostatic chronopotentiometry

Galvanostatic chronopotentiometry (GCP) is a technique from which many different characteristics of a battery can be obtained. In a GCP experiment, the battery is repeatedly charged and discharged at a constant current, while the electrical potential is acquired at frequent time intervals ($\sim$ 1 s), so capacity, defined as the electric charge that can be stored and equating to the current integrated over time, is the product of current and time of each semicycle. If charge and discharge are performed at a low enough rate, galvanostatic curves can also be considered a good approximation of the open circuit voltage (OCV) curve. Rate of charge/discharge dependence of capacity can also be analysed, and from cell behaviour over a long number of cycles it is also possible to understand effects of long-term usage, like capacity loss caused by ageing. Moreover, from GCP the amount of ions moving from the anode to the cathode can be calculated, thus estimating the chemical species building up in the electrodes during the interaction. Mass $m$ of the active material and charge flown through the electrolyte, equal to the product of current $I$ and time $t$, are related by Faraday's first law:

$$m = \frac{M}{zF} \cdot It \tag{4.14}$$

where $M$ is the molar mass, $z$ is the total number of electronic charges flown and $F$ is Faraday's constant, equal to the product of the charge of the electron and Avogadro's number. This way, it is possible to estimate the stoichiometry of the intercalation compounds produced after the electrochemical reaction of the electrode, assuming intercalation is the only process occurring[88].

Potential as a function of time during charge or discharge is typically "S" shaped. Such behaviour is explained by Gibbs' phase rule:

$$DOF = C - P + 2 \tag{4.15}$$

Where $C$ is the number of elements in the system, $P$ is the number of phases, and $DOF$ is the number of degrees of freedom, or the number of intensive thermodynamic parameters needed to fully describe a system and all its properties, including electrical potential. If all the $DOF$ parameters, as for example temperature and pressure, are maintained constant, potential will approximately be constant; otherwise potential will have an "S" shaped curve, since it won't be solely based on the difference of standard potential between the electrode and the electrolyte, but it will be influenced also by other parameters, as for example concentration of ions in one of the two electrodes. In some cases, multiple plateaus can be observed; such behaviour is typical of the formation of different phases in one or both electrodes during discharge.[5].

When a battery potential is dependant on the concentration of compounds in the electrodes, behaviour can be explained by Nernst's equation. Considering $N$ compounds involved in an electrochemical reaction, each with chemical potential $\mu_i$ and a stoichiometric factor $\nu_i$:

$$\Delta G = \sum_{i=1}^{N} \nu_i \cdot \mu_i \tag{4.16}$$

In the hypothesis of low current, energy available per molar unit is equal to the reaction's free energy:

$$\Delta G = -zF\Delta V_0 \tag{4.17}$$

where $F$ is Faraday's constant and $\Delta V_0$ is the theoretical potential of the cell, equal to the difference between the standard potentials of the electrode materials. By combining 4.16 and 4.17:

$$-\frac{\Delta G}{zF} = \Delta V_0 = \frac{1}{zF}\sum_{i=1}^{N} \nu_i \cdot \mu_i \tag{4.18}$$

The chemical potential of a half-cell, or of just one of the reactions taking place on each electrode, depends on the concentration $c_i$ of the compounds reacting on the electrode:

$$\mu_i = \mu_{i0} + RT \cdot ln(c_i) \tag{4.19}$$

where $R$ is the ideal gas constant and $T$ is the temperature. From 4.18 and 4.19, Nernst's equation, addressing only one of the two electrode reactions, can be obtained:

$$\Delta V = \Delta V_0 + \frac{RT}{zF}\sum_{i=1}^{N} \nu_i \cdot ln(c_i) \tag{4.20}$$

Such equation explains the behaviour of the potential $\Delta V$ of a battery as a function of the concentration of compounds reacting on the electrodes[88].

In non-equilibrium conditions, when current is flowing through the electrochemical cell, it is possible to experience a deviation from the expected potential. Such deviation $\eta$ is called overpotential, and is described by:

$$\Delta V_{real} = \Delta V - \sum |\eta| \tag{4.21}$$

Overpotential can have multiple explanations:

- **Charge transfer**: caused by a limit in the speed of charge transfer through the interface between electrode and electrolyte. It depends on the involved compounds.
- **Diffusion**: caused by slow diffusion in the electrode, from the electrode-electrolyte interface to the current collector. It is typically observed at high current rates, and determines a gradient of reaction products in the electrode, with a consequent lack of reagents at the interface.
- **Reaction**: it is due to reaction not happening at the electrode-electrolyte interface, but inside the bulk electrode or electrolyte. It is typically negligible, but may be the limiting factor in certain conditions.
- **Crystallization**: it is the result of an ineffective intercalation of metal ions in the electrode lattice, with consequent crystallization outside of the electrode[88].

The effect of the overpotential is an offset in the measured potential, with respect to the actual potential difference of the electrodes: one possible consequence is, for example, considering a cell completely charged or discharged when a fraction of ions can still be intercalated or extracted. Another possible issue of overpotential is the danger of starting to build a plating of metallic ions on the surface of the electrode, thus damaging or killing the cell, if potential drops below zero. In lithium-ion batteries, for example, a lithium plating can cover the graphite anode, since graphite has a potential close to zero vs Li/Li$^+$. Typically, overpotential is current dependant and behaves like a resistance, thus satisfying Ohm's law:

$$\eta = IR \tag{4.22}$$

Where $R$ is the overall resistance of the battery[88].

### 4.3.1 Experimental setup

Three different instruments were employed for GCP: a Kikusui DC Voltage/Current Standard Model 101 as direct current source and a Keithley Multimeter 2000 connected to a PC via RS-232; a Landt CT2001A battery testing system; and an Arbin LBT21084 battery test equipment. Each instrument sampled potential values every interval of 1 s. Kikusui-Keithley setup was used to characterize sodium-ion batteries (SIB) with $C_{60}$- and $C_{60}H_x$-based electrodes[92], which were charged and discharged between 0.1 V and the potential of the freshly assembled cells, respectively of 2.4 V and 2 V (Vs Na/Na$^+$). Landt CT2001A was employed to study all magnesium-ion batteries (MIB) and SIB with $C_{60}$-$C_{70}$ mixture-based electrodes[93]; magnesium-ion half-cells were charged and discharged between 0.01 V and 2 V, while mixture-based electrodes were charged and discharged between 0.05 V and either 1.6 V (fullerene mixture) or 2 V (ball-milled mixture). Arbin LBT21084 was used to characterize all LIB; half-cells were charged and discharged between 0.01 V and 2 V, while full-cells between 0.01 V and the maximum operation voltage of the cathodes: 4.4 V for NMC, 4.2 V for LCO, 3.5 V for LFP.

## 4.4 Cyclic voltammetry

Cyclic voltammetry (CV) is a technique to study electron transfer processes at the interface between the electrode and the electrolyte in an electrochemical cell. In a CV experiment, the flow of electrons caused by chemical changes, usually due to the oxidation or reduction of a metal complex, is measured. In a typical two-electrodes CV, a difference of potential is applied to a pair of electrodes thanks to a potentiostat, and the current flowing through the electrodes is measured. When the applied potential, varying linearly at a speed called "scan rate", decreases from the upper bound to the lower bound of the potential window, the sweep is called "cathodic trace"; when the lower limit is reached, scan direction is reversed, and during the sweep, called "anodic trace", the potential increases back to the upper limit[100].

Charge transfer are described by Nernst's equation 4.20; in contrast to GCP experiments, in a CV test potential is externally controlled, determining a variation of the concentration of the species in solution or in the electrode. Considering as an example an electrochemical cell with a sodium-based electrolyte, in which the chemical species in solution is $Na^+$, and a $C_{60}$-based working electrode, acting as a cathode, the cell starts with a potential $\Delta V_0$. By applying a decreasing potential, sodium ions start reacting with the $C_{60}$-based electrode when the potential is low enough in order for a reduction reaction to occur: $C_{60}$ molecules on a diffusion layer near the surface of the electrode are reduced and become $C_{60}^-$s, and the compound $NaC_{60}$ is produced:

$$\Delta V = \Delta V_0 + \frac{RT}{zF} \cdot ln \frac{[C_{60}]}{[C_{60}^-]} \tag{4.23}$$

where the variable is the logarithm of the relative concentration of the chemical species on the surface of the electrode before and after oxidation. A charge transfer occurs at the interface of the electrode, since a positively charged $Na^+$ enters the electrode, and thus a current flow is measured, due to the fact that $C_{60}$ is reduced and an electron is involved:

$$Na^+ + C_{60} + e^- = Na^+ + C_{60}^- \tag{4.24}$$

When the potential is zero, all the electrode's surface is saturated and no more sodium ions can be intercalated. When a positive sweep is started and potential increases, nothing happens until a high enough potential is applied in order for the oxidation $C_{60}$ to occur; consequently, sodium is dissolved back in the electrolyte and a current flow with the opposite direction is measured. When the transfer of electrons is fast enough, the current peak observed during reduction is at the same potential of the current peak observed during oxidation; in this case the electrochemical reaction is considered reversible and follows the Nernst equation, so the reaction is called "Nernstian"[100].

The scan rate of a CV is an important parameter, since the depth of the diffusion layer depends on it. For example, increasing the scan rate determines a decrease of the diffusion layer, with a consequent increase in the measured current. Peak current is described by the Randles-Sevcik equation, which is true for electron transfer processes involving freely diffusing species:

$$I_P = 0.4663 \cdot zFAC\sqrt{\frac{zFvD}{RT}} \tag{4.25}$$

where $I_P$ is the peak current, $A$ is the interfacial area of the electrode, $C$ is the bulk concentration of the chemical species in solution, $v$ is the scan rate, and $D$ is the diffusion coefficient of the chemical species in solution. It is then clear that peak current is linearly proportional to the square root of the scan rate. For non-freely diffusing species, mostly due to surface adsorption of the dissolved chemical species, as happens in all battery systems, 4.25 is not valid, and the Randles-Sevcik equation takes the form:

$$I_P = \frac{n^2F^2}{4RT}vA\Gamma^* \tag{4.26}$$

where $\Gamma^*$ is the adsorbed species surface coverage. In such case, peak current is expected to increase linearly with the scan rate[1].

### 4.4.1 Experimental setup

Cyclic voltammetry (CV) was performed on the half-cells using a Keithley Sourcemeter 2400 at 10 mV $s^{-1}$. Materials of interest were used as working electrodes, while the pure metal of intercalating ions was used as both counter and reference electrode. For SIB, NaI in polyethylene oxide (PEO) solid electrolyte was employed[92], while for MIB $Mg(AlCl_2BuEt)_2$ in tetrahydrofuran (THF, Sigma Aldrich, 99.9%) was used. For details on the preparation of the electrolytes, refer to the 4.5.2 section.

## 4.5 Sample preparation

### 4.5.1 Sample handling

Most battery components, in particular the electrolyte, are highly air-sensitive, so all samples were prepared and cells were assembled in an argon-filled glove box (either MBRAUN MB 200B or MBRAUN Labmaster 130), with oxygen and water concentrations lower than 1 ppm; electrochemical cells and solid electrolyte samples were tested either in airtight stainless steel coin cells (standard CR2032), or, when performing measurements at temperatures higher than room temperature, in an airtight split cell (MTI corporation, stainless steel SS304), with either a silicone or Viton o-ring.

### 4.5.2 Electrolytes

PEO-based ionic conductor was employed as solid electrolyte in SIB. Reagents were thermally treated for 24 h at $10^{-6}$ mbar dynamic vacuum in Schlenk vials before use, to ensure complete water and solvents removal. Temperature was 50 °C for PEO and 300 °C for the other reagents. PEO (Sigma Aldrich, $M_w = 1\,000\,000$) and sodium iodide (NaI, Sigma Aldrich, 99%) were dissolved in anhydrous acetonitrile (Sigma Aldrich, 99.8%), such as the ratio between oxygen atoms in PEO chains and sodium ions in NaI was 10:1, as reported in [35]. To prevent crystallization of the ionic conductor upon cooling, which would reduce ionic conductivity, nanostructured aluminium oxide ($Al_2O_3$, Sigma Aldrich, average particle size 13 nm, 99.8%), was added to the mix as 10% of the total mass of PEO+NaI, according to [85]. The obtained solution was stirred overnight and drop cast on a flat polytetrafluoroethylene substrate. After 24 h drying at room temperature, the discs were detached from the substrate. All steps were carried out in a glove box[92].

Borohydride-fulleride composites were prepared via solid-state high energy ball milling. $Li_xC_{60}$ (x = 4, 6, 12) and $Na_6C_{60}$ were fist synthesized. $Li_4C_{60}$ and $Na_6C_{60}$ were synthesized starting from $C_{60}$ (MER Corporation, 99+%, purified at 250 °C for 12 h under vacuum) and lithium azide ($LiN_3$) or sodium azide($NaN_3$). Lithium azide (20% wt in water) and sodium azide (20% wt in water) were purchased from Sigma Aldrich and dried in a flask under vacuum at 90 °C using a Heidolph WB2000/VV2000 system. Each azide was then dissolved in ethanol (Fluka, 99.8%) washed with anhydrous diethyl ether (Carlo Erba Reagents, 99.9%) and filtered through a ceramic porous septum, then dried in an oven at 60 °C. $C_{60}$ and either $LiN_3$ or $NaN_3$ were ground together in stoichiometric ratio and pelletized, then thermally treated in a tantalum envelope under dynamic vacuum at $10^{-6}$ mbar; for $LiN_3$, thermal treatment was a sequence of a ramp of 30 °C $h^{-1}$ up to 120 °C, then of 5 °C $h^{-1}$ up to 180 °C, and finally of 20 °C $h^{-1}$ up to 240 °C, at which the sample was left for 5 h. For $NaN_3$, the sample was heated up to 250 °C with a ramp of 50 20 °C $h^{-1}$, then treated at 450 °C for 5 h, with a ramp of 10 °C $h^{-1}$. Both $Li_6C_{60}$ and $Li_{12}C_{60}$ were synthesized starting from $C_{60}$ and pure lithium (Sigma Aldrich, 99%), which were put in an agate bowl in stoichiometric ratio and ball milled for 30 minutes (3 cycles of 10 minutes with 5 minutes rests between each cycle) at 30 Hz with a Fritsch Pulverisette 23.

Either lithium borohydride ($LiBH_4$, Sigma Aldrich, 95%) and $Li_xC_{60}$ or sodium borohydride ($NaBH_4$, Sigma Aldrich, 98%) and $Na_6C_{60}$ were put in a agate bowl and ball-milled for 90 minutes (9 cycles of 10 minutes with 5 minutes rests between each cycle) at 30 Hz with a Fritsch Pulverisette 23. Borohydride:fulleride ratio was 50:50 weight, with the exception of $LiBH_4$-$Li_6C_{60}$ composite, for which different ratios (25:75, 50:50 and 75:25) of fulleride and borohydride were synthesized. After ball-milling, $LiBH_4$-$Li_xC_{60}$ samples were thermally treated under vacuum at $10^{-6}$ mbar at a temperature of 220 °C (with a ramp of 50 °C $h^{-1}$) for 24 h, apart for $LiBH_4$-$Li_6C_{60}$ composite, for which three different durations of the thermal treatment were used: 2 h, 24 h and 48 h. $NaBH_4$-$Na_6C_{60}$ was thermally treated in a sealed pyrex vial filled with argon at a temperature of 300 °C (with a ramp of 50 °C $h^{-1}$) for 2 h, then left at 350 °C for 24 h. Samples were then pelletized with a titanium pelletized with a diameter of 6.5 mm, and tested by means of EIS in a split cell. Temperature was controlled with a previously calibrated resistor heater covered in Kapton (Minco Inc.).

Magnesium-ion battery electrolyte was synthesized starting from di-n-butyl magnesium ($MgBu_2$, Sigma Aldrich, 1 M in heptane) and ethylaluminium dichloride ($AlCl_2Et$, Sigma Aldrich, 1 M in hexane), which were put in a vial in argon flux in a stoichiometric ratio, and stirred for 1 day at room temperature; the solution became completely opalescent, testifying the formation $Mg(AlCl_2BuEt)_2$. After that, solvents were removed by vacuum pumping and then anhydrous, degassed THF was added, to obtain a 0.25 M solution[18].

A gel composite electrolyte, based on $Mg(AlCl_2BuEt)_2$, was also realized and characterized. Polyvinylidene fluoride (PVDF, Solvay, Solef 5310) was added to $Mg(AlCl_2BuEt)_2$ 0.25 M in THF, so that the ratio between fluorine atoms in PVDF chains and magnesium ions was 10:1. The solution was sealed in an airtight flask and stirred at 80 °C for 12 h. The solution was then drop-cast on a polytetrafluoroethylene (PTFE) substrate and left drying until it became from liquid to gel-like. In order to obtain an enhancement in ionic conductivity, two more samples were realized: following the example, respectively, of PEO-based electrolytes and of borohydride composites, 10% in weight of either nanostructured $Al_2O_3$ or $C_{60}$ was added to the solution before heating and stirring.

### 4.5.3 Graphene and derivatives

Thermally exfoliated graphite oxide (TEGO) was synthesized starting from graphite power (SGL Carbon, RW-A grade, average particle size 66 mm), which was oxidized through the Brodie method: graphite was mixed with ground sodium chlorate ($NaClO_3$, Sigma Aldrich, >99%); concentrated nitric acid was added drop by drop while stirring the powder. Temperature was kept close to 0 °C through an ice bath until all the acid was added. The mixture was then heated for 8 h at 60 °C with a slow thermal ramp (20 °C $h^{-1}$). After cooling to room temperature, the mixture was stirred for 24 h, until it became dark green. The suspension was then washed in milli-Q water and filtered with a coarse filter paper; the product was then washed in a water-based hydrochloric acid solution, filtered, and washed again two more times with milli-Q water. The product was then dried at 60 °C overnight. The obtained graphite oxide powder was thermally exfoliated by sudden exposure to 1100 °C under dynamic vacuum, thus obtaining TEGO[21].

Hydrogenated TEGO (H-TEGO) was obtained by heating TEGO in a quartz vial at 800 °C under hydrogen flux for 1 h at ambient pressure. Neither that TEGO or H-TEGO have been exposed to air during their preparation[21].

Conductivity of TEGO was measured by supplying different values of direct current, in the range of $10^{-3}$-$10^{-6}$ A, with a Keithley 6221 Current Source and measuring the direct voltage with a Keithley 2182A Nanovoltmeter. Measurements were made on thin samples, with four ohmic gold contacts in Van der Pauw geometry with the Keithleys operating in Delta mode.

### 4.5.4 Electrodes

$C_{60}$-, $C_{60}H_x$- (x∼39), and fullerene mixture-based electrodes for SIB were prepared by mixing 85% in weight of the active material with 10% polyvinylidene fluoride (PVDF, Solvay, Solef 5310) binder with 5% carbon black (CB, Timcal, Super C65) conductive agent. Electrodes for MIB were prepared similarly, but with polytetrafluoroethylene (PTFE, Sigma Aldrich, 60% wt dispersion in water), as in [25]. Slurries were obtained by adding anhydrous N-methyl-pyrrolidone (NMP, Sigma Aldrich, 99.5%) until the solution was completely homogeneous, while stirring in a pyrex flask. The mix was then cast on a copper foil (Alfa Aesar, 25 $\mu$m thick, 99.8%) and spread with a thickness of 0.3 mm by using a notch bar. NMP was removed at 60 °C in a vacuum oven overnight. The film was pressed at about 7 Mpa in a hydraulic press, then discs with a diameter of 7 mm were punched. $C_{60}$, $C_{60}H_x$, and fullerene mixture were purchased from MER corporation with 99+% purity. All starting materials were thermally treated before use under vacuum at $10^{-6}$ mbar at a temperature of 250 °C for 12 h, apart for solvents and PVDF, which was thermally treated under vacuum at 130 °C[92]. Fullerene mixture was employed both as received and after ball-milling treatment, in an agate bowl at 30 Hz with a Fritsch Pulverisette 23 for 90 minutes (9 cycles of 10 minutes with 5 minutes rests between each cycle)[93].

Magic Angle Spinning (MAS) Nuclear Magnetic Resonance (NMR) was performed to verify that no polymerization occurred after ball-milling of fullerene mixture, reported in some cases[59]. NMR spectra were acquired with a JEOL ECZ 600R spectrometer. NMR was performed on $^{13}$C under a magnetic field of 14 T with a frequency of 600 MHz, with a Hahn echo pulse, applying a 2.2 $\mu$s 90° pulse followed by a 4.4 $\mu$s 180° pulse and a $\tau$ of 8.3 $\mu$s. Spinning of MAS rotors, respectively at 5 and 18 kHz for fullerene mixture and ball-milled mixture, was obtained with a Nitrogen flux[93].

TEGO- and H-TEGO-based electrodes were prepared by mixing 90% in weight of the active material with 10% binder. Several different binders were tested, in order to increase the mechanical restitance of the elctrodes: polyacrilic acid (PAA, Sigma Aldrich, average $M_w = 1800$), PVDF (Kynar, Arkema), carboxymethyl cellulose (CMC, MTI Corporation, average $M_w = 4 \cdot 10^5$), sodium alginate (Na-A, $(C_6H_7O_6Na)_n$, MP Biomedicals) and lithium polyacrilic acid (LiPAA), obtained from reaction of PAA with lithium hydroxide (LiOH, Sigma Aldrich, 98%) in water at PH=7. In the end PAA was chosen. No conductive agent was added, thanks to the already high electrical conductivity of both active materials[21]. Slurries were obtained by adding anhydrous NMP until the solution was completely homogeneous, then the mix was cast on a copper foil and spread with a thickness of 0.5 mm with a notch bar. NMP was slowly removed at 60 °C in air for 30 minutes, then at 80 °C in a vacuum oven overnight. Electrodes were then hot-pressed at 50 °C between two rollers with a spacing of 0.1 mm and punched with a diameter of 13.7 mm.

### 4.5.5 Cell assembly

Before cell assembly, the mass of each electrode was measured, in order to calculate specific capacity from GCP. Half-cell assembly started from the active electrode, placed on the bottom of a coin cell or of the split cell. For all-solid state SIB, PEO-based electrolyte discs were placed onto the electrode, completely covering the active material[92][93]. For MIB, glass microfibre separator disks, completely covering the electrodes, were soaked in the $Mg(AlCl_2BuEt)_2$ electrolyte solution. For LIB, Celgard separators were employed, which were placed onto the electrodes and soaked in an electrolyte lithium hexafluorophosphate 1 M solution in ethylene carbonate-diethyl carbonate($LiPF_6$ solution in EC/DEC, ratio EC:DEC=50:50 in volume, Merck corporation, battery grade). Finally, a counter electrode of the pure element of the active ions was placed on the wet separator (Figure 4.7 (a)): for SIB, discs of pure sodium (Sigma Aldrich, 99.98 %); for LIB, discs of pure lithium (Sigma Aldrich, 99.9 %); for magnesium, due to the easy oxidization of magnesium surface even in glove box, a different approach was needed. Pure magnesium was obtained from thermal decomposition of magnesium hydride ($MgH_2$, ABCR chemicals, 98 %), performed under $10^{-6}$ mbar vacuum at 350 °C (70 °C $h^{-1}$ up to 200 °C, then 20 °C $h^{-1}$ up to 350 °C). The obtained magnesium powder was then pelletized with a diameter of 6.5 mm.

Graphene-based LIB were also tested in full cells, complete with cathode. Cathodes were prepared by suspending 85% wieght of either lithium cobalt oxide (LCO), lithium nickel manganese cobalt oxide (NMC, Ni:Mn:Co=1:1:1) or lithium iron phosphate (LFP) powder, purchased from MTI corporation, with 7.5 % of carbon black (Timcal, Super P) conductive agent and 7.5 % of PVDF binder in anhydrous NMP. Solutions were stirred and cast on an aluminium foil and spread with a 0.3 mm notch bar. NMP was slowly removed at 60 °C in air for 30 minutes, then at 80 °C in a vacuum oven overnight, and electrodes were then punched with a diameter of 13.7 mm. In order to assemble full cells, TEGO and H-TEGO electrodes had to undergo a pre-lithiation process, due to the fact that such systems consume a considerable amount of the lithium during the formation of SEI, with the risk of lacking enough lithium to fully lithiate during the subsequent cycles. To do this, half-cells with graphene-based electrodes were discharged and charged 3 times, then the

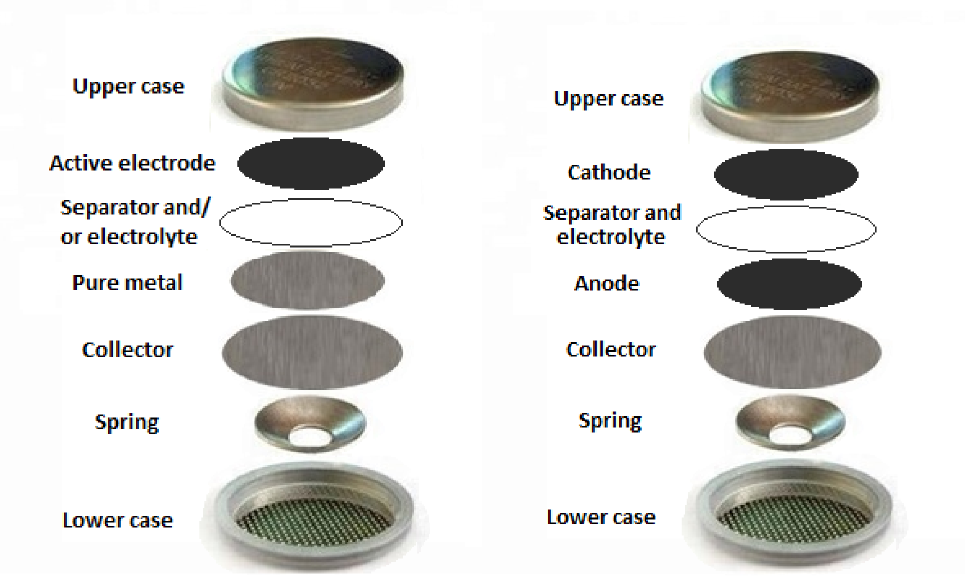

(a) (b)

Figure 4.7: Scheme for the assembly of batteries: (a) half-cell; (b) full-cell.

cells were opened to remove the electrodes; this method is different than that reported in [30], and has the advantage of allowing the formation of a more complete SEI, since the capacity loss due to SEI formation is observed during the first few cycles, not just the first one. Evidence that SEI is preserved after disassembling the half-cells has been reported in [28]. Then, electrodes were placed in new coin cells, a new Celgard separator was added along with fresh $LiPF_6$ in EC/DEC electrolyte solution, and finally the cathodes were added (Figure 4.7 (b)). Masses of the electrodes were balanced so that anodes and cathodes had equal capacity, with a tolerance of 10%.

All solid-state SIB were tested at 60 °C, in order to achieve an acceptable ionic conductivity in the PEO-based solid electrolyte. When using the split cell, a previously calibrated resistor heater covered in Kapton (Minco Inc.) was employed[92]. When using coin cells, devices were directly dipped in alumina powder, inside a thermostatic vessel controlled by a Lauda RCS 6-D thermostat[93].

# Chapter 5

# Results and discussion

## 5.1 Sodium-ion batteries

Thanks to the large interstitial void in fullerene crystal structure and to the tendency of fullerene molecules of accepting electrons, $C_{60}$ is a good candidate as anode in sodium-ion batteries, to replace graphite which cannot intercalate sodium. Sodium-ion half-cells with electrodes based on $C_{60}$ were studied by means of cyclic voltammetry (CV), galvanostatic chronopotentiometry (GCP), electrochemical impedance spectroscopy (EIS), X-ray diffraction (XRD) and magic angle spinning nuclear magnetic resonance (MAS-NMR), with the aim of understanding the intercalation mechanism of sodium in fullerene and of developing new battery technologies based on sodium. Other fullerene-related materials, $C_{60}H_x$ and fullerene mixture, were also characterized and employed in sodium-ion half-cells, in order to enhance specific capacity and increase reversibility, which was found out to be an issue in $C_{60}$-based half-cells. By using $C_{60}H_x$ and fullerene mixture, an expansion of the crystal structure can be obtained, as well as an increase in disorder and hindrance of the polymerization between fullerene molecules. Due to the solubility of $C_{60}$ in the typical organic solvents used for battery electrolytes[20], a proper solid electrolyte was optimized and employed[92][93].

### 5.1.1 Characterization of electrode materials

Powder XRD was performed on fullerene mixture in order to study its crystal structure (Figure 5.1 (a)). Fullerene mixture is characterized by two separate phases, recognizable as $C_{60}$ and $C_{70}$ crystal structures. $C_{60}$ peaks are indexed by a *fcc* structure, of symmetry group $Fm\bar{3}m$ and lattice constant $a$=14.185 ± 0.003 Å, while $C_{70}$ peaks are indexed by a *hcp* structure, of symmetry group $P6_3/mmc$ and lattice parameters $a$=10.637±0.004 Å and $a$=17.49±0.01 Å. The lower intensity of the $C_{70}$ peaks is due to the lower content of $C_{70}$, approximately of 26% opposed to 74% of $C_{60}$, as estimated by Rietveld quantitative phase analysis. Such composition is consistent with the composition of fullerene mixture obtained from the soot without further refinement[59]; such unrefined material was chosen in order to evaluate the electrochemical performance of a cheaper electrode material with respect to $C_{60}$. After discovering that fullerene mixture is in fact composed by two different phases, a treatment to obtain a homogeneous electrode material was needed. High-energy ball-milling was chosen as a solid state treatment to break $C_{60}$ and $C_{70}$ crystallites to merge them in a single structure. Powder XRD was then performed on ball-milled mixture in order to evaluate the effect of the ball-milling treatment on $C_{60}$ and $C_{70}$ molecules. After ball-milling, the XRD pattern is a single *fcc* phase, similar to that of $C_{60}$, but with larger peaks and a lattice constant $a$=14.299±0.003 Å. The increase of the intensity in the region between the peaks at 18° and 21°, as well as the enlargement of the peaks, are due to the decrease of grain size, with average crystallite dimension of 8 nm, and possibly also to the formation of an amorphous fraction and/or stacking faults; all the three effects are ascribable to the high-energy ball-milling treatment. The increase of the lattice constant and the presence of a single phase suggest that the ball-milling treatment was successful in producing a solid solution of $C_{60}$ and $C_{70}$ molecules, in which $C_{70}$ molecules are merged into the *fcc* lattice of $C_{60}$. Such insertion is also effective in increasing from 710 to 723 $A^3$ the available volume per each fullerene, thus also increasing the space of the interstitial voids between molecules[93]. MAS-NMR was performed on the samples in order to check the presence or absence of covalent bonds between fullerenes, which should be proven by the rising of peaks in the chemical shift in the range of 0-100 ppm due to the formation of covalent bonds with $sp^3$ hybridization (Figure 5.2). No signature of polymerization was observed in the NMR spectrum[93].

### 5.1.2 Characterization of half-cells

#### Cyclic voltammetry

CV was performed on $C_{60}$ and $C_{60}H_x$, in order to better understand sodium insertion and extraction mechanisms. Figure 5.3 (a) shows the first two redox cycles of a half-cell with $C_{60}$-based electrode. During the first sweep, from high to low voltage, at least two reduction peaks are observed, while during the second sweep, back to a higher potential, six oxidation peaks are distinguishable, as reported in Table 5.2. During the second cycle, the six peaks are observed both during the reduction sweep, contrarily to the first cycle, and during the oxidation sweep; the presence of the same number of peaks during oxidation and reduction suggests that the electrochemical intercalation of $Na^+$ in $C_{60}$ is reversible, albeit the potential peak labelled as "D" is not observed during the second reduction. Even more interestingly, six different intercalation compounds are formed during reduction, since six different reversible electrochemical processes are observed, corresponding to

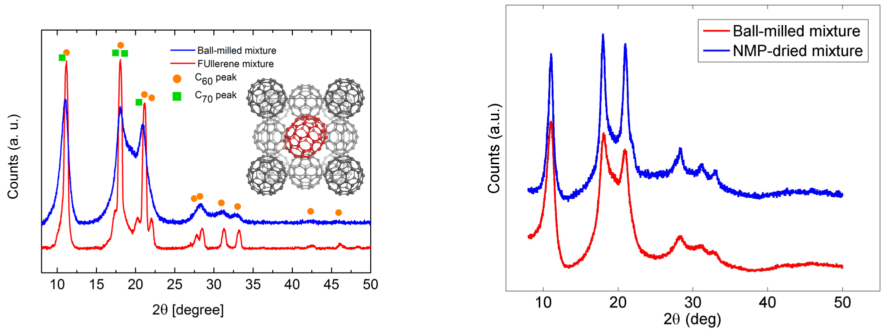

(a) (b)

Figure 5.1: (a) XRD of fullerene mixture and ball-milled mixture compared. Expected peaks for *fcc* $C_{60}$ and *hcp* $C_{70}$ are highlighted. After ball milling, the two phases of different-sized fullerene merge, giving rise to a single *fcc* phase with larger lattice (inset)[93]. (b) Ball-milled fullerene mixture after dispersion in NMP and drying, compared to as-prepared fullerene mixtures[93].

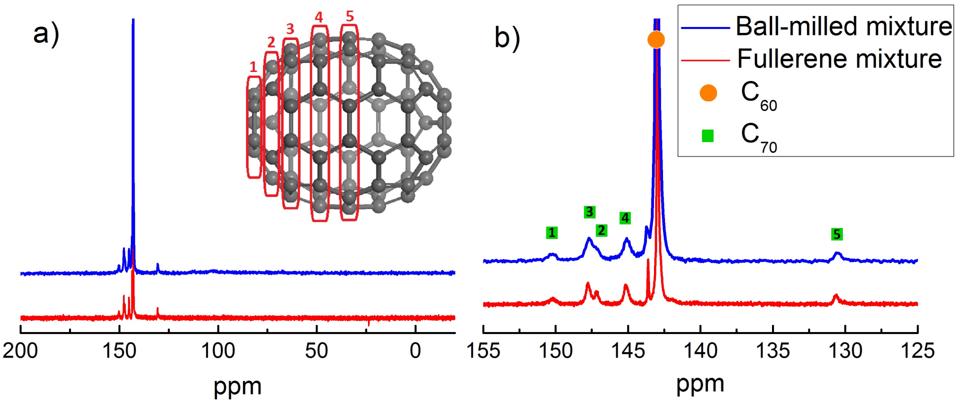

Figure 5.2: (a) MAS-NMR of fullerene mixture and ball-milled mixture compared. No significant changes are observed[93]. (b) Highlight of NMR signal of $C_{60}$ (at 143 ppm) and $C_{70}$ (five shorter, broader peaks). The sharp peak at about 143.5 ppm is due to solvent traces[93]. Inset: equivalent position of carbon atoms in $C_{70}$, giving rise to five different chemical shifts, highlighted in green.

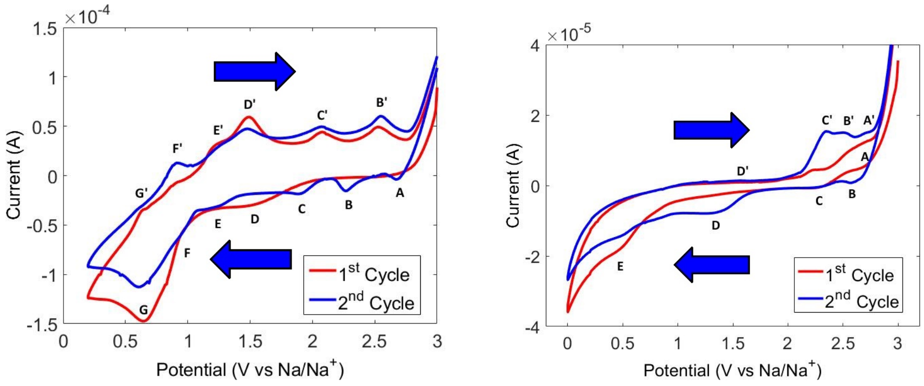

(a) (b)

Figure 5.3: Cyclic voltammetry of half-cells with electrodes based on $C_{60}$ (a) and $C_{60}H_x$ (b)[92]. Starting potential is 3 V and sweep direction is indicated by the arrows. The letters indicate the positions of the reduction/oxidation peaks, reported in Tables 5.2 and 5.3.

six different $Na_xC_{60}$ stoichiometries. It is worth noting that the accessible redox states of $C_{60}$ are exactly six, since such is the number of electrons in the lowest unoccupied molecular orbital (LUMO) band of $C_{60}$; this hints at the fact that six different $Na^+$ ions per $C_{60}$ molecule are reversibly inserted in the electrode. It is also worth noting that the reactions occur with approximately equal potential intervals between one another. Further CV cycles show the same peaks to those of the second cycle, confirming the reversibility of the process[92].

CV on the $C_{60}H_x$ electrode is shown in Figure 5.3 (b). As for $C_{60}$, many different reactions are observed. During the first reduction sweep three reaction are observed, while during the first oxidation just two peaks are detectable. During the second cycle, two more peaks are observed, for a total of five different reduction reaction (Table 5.3), with only the one at the lowest potential not showing an oxidation counterpart. Subsequent cycles show the same peaks as the second cycle. Contrarily to what observed in $C_{60}$, peaks are not equally separated in potential[92].

### Galvanostatic chronopotentiometry

GCP was employed to probe the performance of all solid-state half-cells with electrodes based on $C_{60}$, $C_{60}H_x$, fullerene mixture and ball-milled fullerene mixture. $C_{60}$ and $C_{60}H_x$ half-cells were discharged and charged with a slow C-rate of C/60 (a current such that the cell is completely discharged in 60 hours), in order for the discharge curve to be a good approximation of an open circuit voltage (OCV) curve. During the first galvanostatic discharge, $C_{60}$ and $C_{60}H_x$ electrodes are characterized by a large specific capacity, re-

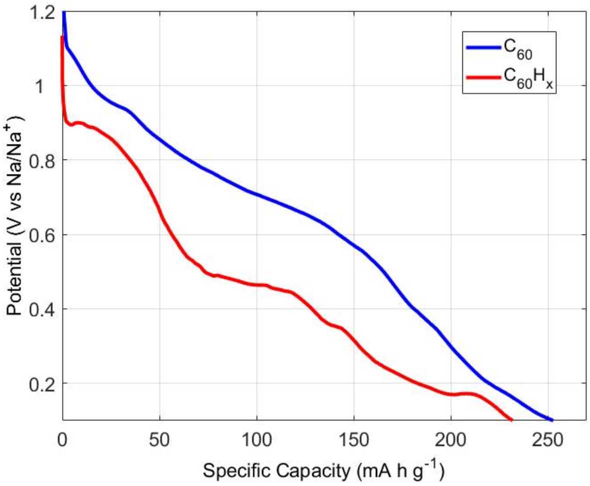

Figure 5.4: OCV of $C_{60}$- and $C_{60}H_x$-based half-cells with respect to the specific capacity, during the first discharge semicycle[92].

spectively of 250 and 230 mA h g$^{-1}$ (5.4), corresponding to a stoichiometry of $Na_{6.8}C_{60}$ and $Na_{6.5}C_{60}H_x$ after a complete discharge, assuming a homogeneous intercalation of the electrode. Each electrode is characterized by several plateaus of the potential, each marking a different electrochemical reaction[92].

For subsequent cycles, specific capacity of $C_{60}$ and $C_{60}H_x$ based electrodes in sodium-ion half cells is shown in Figure 5.5. The $C_{60}$-based electrode is characterized by an evident irreversibility of the specific capacity, and capacity retention lower than 1% after few cycles. On the contrary, $C_{60}H_x$ features a better reversibility, with a specific capacity of 34 mA h g$^{-1}$ after 10 cycles, although still much lower than the initial capacity[92].

GCP was also employed to test the performance of all solid-state half-cells with electrodes based on fullerene mixture and ball-milled fullerene mixture. The cells were tested with a slow C-rate of C/70, to better estimate the OCV curve. Both electrodes were characterized by a large specific capacity during the first discharge, up to 276 mA h g$^{-1}$ for fullerene mixture and 320 mA h g$^{-1}$ for ball-milled mixture, which is larger than first cycle specific capacity of pure $C_{60}$ and $C_{60}H_x$. For each fullerene molecule, the calculated number of sodium ions after complete intercalation is 7.7 for fullerene mixture and 8.9 for ball-milled mixture. Fullerene mixture is characterized by a single plateau at about 1 V, while ball-milled mixture shows three main plateaus, at about 1.9 V, 1.4 V and 0.2 V (Figure 5.6)[93].

Similarly to $C_{60}$ and $C_{60}H_x$, part of the specific capacity of mixtures is lost

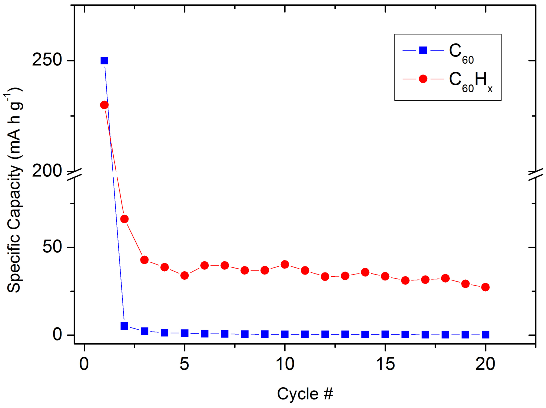

Figure 5.5: Specific capacity of half-cells with electrodes of $C_{60}$ and $C_{60}H_x$ during the first 20 cycles[92].

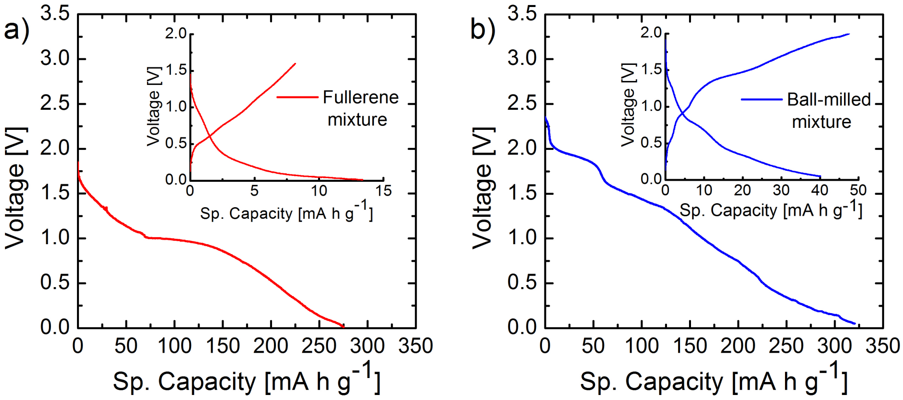

Figure 5.6: OCV of fullerene mixture (a) and ball-milled mixture (b) based half-cells with respect to the specific capacity, during the first discharge semicycle, and during subsequent charge and discharge cycles (insets)[93].

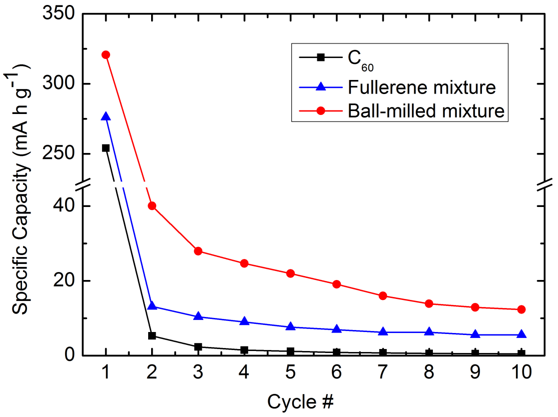

Figure 5.7: Specific capacity of half-cells with electrodes of fullerene mixture and ball-milled mixture during the first 10 cycles, compared to that of pure $C_{60}$[93].

after the first cycle. In the inset of Figure 5.6, discharge curves for cycles subsequent to the first are shown, while Figure 5.7 displays the specific capacity for the first 10 cycles. Fullerene mixture shows a strong irreversible character, albeit reversibility is higher than that of pure $C_{60}$, hinting at the fact that reversibility of $C_{70}$ is higher. Ball-milled mixture shows an even higher reversibility, suggesting that the disorder introduced by the alloying of $C_{60}$ and $C_{70}$ is effective in reducing the formation of stable, irreversible phases[93].

### 5.1.3 Impedance spectroscopy

EIS measurements were performed on half-cells with fully intercalated electrodes based on $C_{60}$ and $C_{60}H_x$, in order to better understand the dynamics of sodium ions in the structure of fullerene and derivatives. Nyquist plots for $C_{60}$ and $C_{60}H_x$ are shown in Figures 5.8 and 5.9. The equivalent circuit model employed for the data analysis is shown in the inset[101]. The model takes into account the SEI impedance ($R_{SEI}$ and $C_{SEI}$), the charge transfer resistance of the $Na^+$ ions at the electrode/electrolyte interface ($R_{CT}$ and $C_{CT}$) and impedance of the $Na^+$ ions moving through the electrode ($R_{Diff}$ and $C_{Diff}$). $R_0$ is the resistance of the contacts and cables, while $L$ is an inductive effect due to the geometry of the battery. Fit parameters are shown in Table 5.1. In particular, for the $Na^+$ ions dynamics inside the electrodes, a resistivity of $\rho$=7.45 MΩ cm was found for the $C_{60}$-based electrode and of $\rho$=617 kΩ cm for the $C_{60}H_x$-based electrode[92].

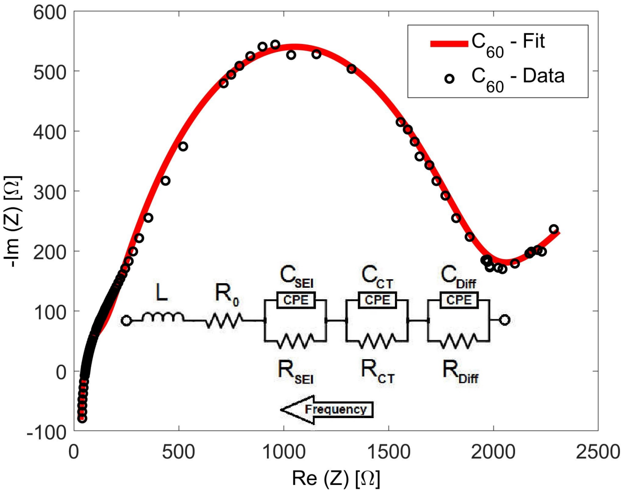

Figure 5.8: Nyquist plot for EIS performed on half-cells with a $C_{60}$-based fully intercalated electrode. Inset: equivalent circuit employed to model the system[92].

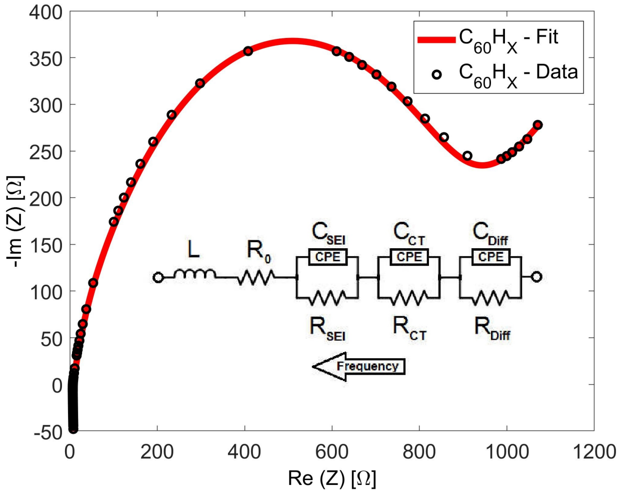

Figure 5.9: Nyquist plot for EIS performed on half-cells with a $C_{60}H_x$-based fully intercalated electrode. Inset: equivalent circuit employed to model the system[92].

Table 5.1: EIS parameters for the impedance analysis of $C_{60}$- and $C_{60}H_x$-based half-cells[92]

| | **L (H)** **(H)** | $\mathbf{R}_0$ (Ω) | $\mathbf{R}_{SEI}$ (Ω) | $\mathbf{R}_{CT}$ (Ω) | $\mathbf{R}_{Diff}$ (Ω) |
|---|---|---|---|---|---|
| $\mathbf{C_{60}}$ | $1.1 \cdot 10^{-3}$ | 9.77 | 1660 | 91.6 | 19600 |
| $\mathbf{C_{60}H_x}$ | $1.3 \cdot 10^{-3}$ | 6.17 | 730 | 71.9 | 4870 |
| | | | $\mathbf{CPE}_{SEI}$ | $\mathbf{CPE}_{CT}$ | $\mathbf{CPE}_{Diff}$ |
| $\mathbf{C_{60}}$ | | | $A=6.3 \cdot 10^{-5}$ F | $A=4.4 \cdot 10^{-6}$ F | $A=4.2 \cdot 10^{-3}$ F |
| | | | $\psi=0.69$ | $\psi=0.83$ | $\psi=0.25$ |
| $\mathbf{C_{60}H_x}$ | | | $A=1.2 \cdot 10^{-3}$ F | $A=2.5 \cdot 10^{-3}$ F | $A=1.4 \cdot 10^{-2}$ |
| | | | $\psi=0.89$ | $\psi=0.91$ | $\psi=0.50$ |

### 5.1.4 Structural characterization of the intercalated electrodes

Post-mortem powder XRD was performed on $C_{60}$ and $C_{60}H_x$ before and after intercalation with sodium. XRD pattern for $C_{60}$ and $Na_xC_{60}$ is shown in Figure 5.10. Several different crystalline phases can be observed, attributable to known $Na_xC_{60}$ phases and to polyethylene oxide (PEO). In particular, the monoclinic phase corresponding to polymeric $Na_4C_{60}$[102] and the cubic phases of $Na_2C_{60}$ and $Na_xC_{60}$, with $x \geq 6$[103]. No peaks of metallic sodium were observed[92].

Figure 5.11 shows the powder pattern for a fully intercalated $C_{60}H_x$ electrode. Contrary to $C_{60}$, the number of reflections is low, and could be attributed to a single phase, tentatively indexed as a tetragonal cell, with lattice parameters $a=b=18.59$ Å, $c=13.72$ Å, $\alpha=\beta=\gamma=90°$.

### 5.1.5 Discussion

$C_{60}$- and $C_{60}H_x$-based electrodes are characterized by many different redox reactions with sodium, corresponding to different redox potentials, observed both with CV and GCP. GCP potential plateaus correspond to some of the intercalation peaks observed during cyclic voltammetry: a comparison between the reaction potentials has been reported in Tables 5.2 and 5.3. For the $C_{60}$-based electrode, the plateau potentials observed in GCP match quite well three of the six reduction peak potentials observed in CV, suggesting that the same electrochemical reactions are occurring; at the same time, three reduction reactions observed in CV are not present in GCP as evident plateaus, suggesting that some of the surface reactions, occurring in CV and corresponding to the redox states of $C_{60}$, do not have a bulk counterpart when intercalating sodium ions, probably due to the fact that the formation

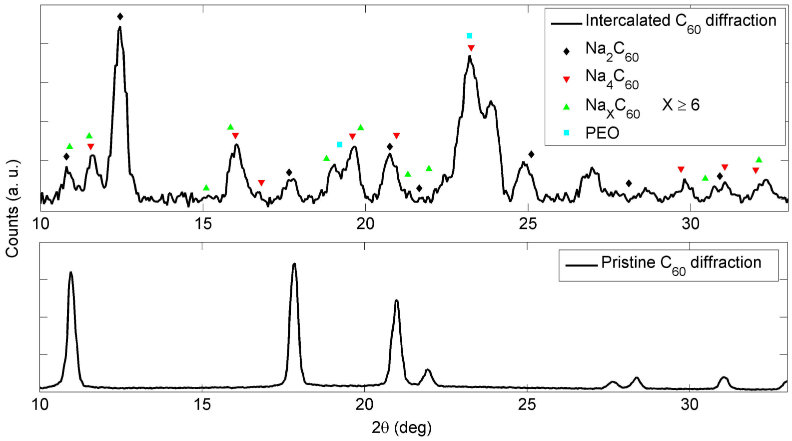

Figure 5.10: Post-mortem powder XRD performed on the fully intercalated $C_{60}$-based electrode, compared to the powder XRD pattern of pure $C_{60}$. Reflections of different $Na_xC_{60}$ phases and of the PEO-based solid electrolyte are highlighted[92].

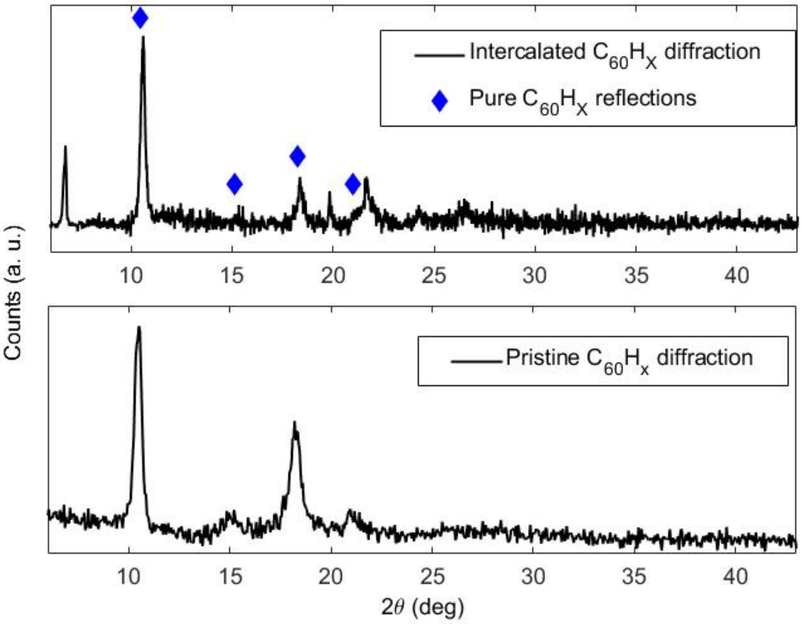

Figure 5.11: Post-mortem powder XRD performed on the fully intercalated $C_{60}H_x$-based electrode, compared to the powder XRD pattern of pure $C_{60}H_x$. Reflections of pure $C_{60}H_x$ are highlighted[92].

Table 5.2: Comparison between reduction reactions in $C_{60}$ electrodes in sodium-ion half cells, observed from CV peaks and from GCP plateaus, with possible stoichiometry of products, assuming homogeneous intercalation[92]

| **Peak index** | **CV $2^{ND}$ reduction peak potential (V vs Na/Na$^+$)** | **GCP plateau potential (V vs Na/Na$^+$)** |
|---|---|---|
| A | 2.68 | - |
| B | 2.27 | - |
| C | 1.90 | - |
| E | 1.21 | 1.10 |
| F | 0.94 | 0.93 |
| G | 0.61 | 0.65 |

Table 5.3: Comparison between reduction reactions in $C_{60}H_x$ electrodes in sodium-ion half cells, observed from CV peaks and from GCP plateaus, with possible stoichiometry of products, assuming homogeneous intercalation[92]

| **Peak index** | **CV $2^{ND}$ reduction peak potential (V vs Na/Na$^+$)** | **GCP plateau potential (V vs Na/Na$^+$)** |
|---|---|---|
| B | 2.58 | - |
| C | 2.30 | - |
| D | 1.35 | 0.89 |
| E | 0.49 | 0.46 |
| - | - | 1.35 |
| - | - | 0.16 |

of some $Na_xC_{60}$ stoichiometries is more favoured than others. As for $C_{60}H_x$, only for a single plateau at around 0.5 V a CV counterpart can be found, while no other plateau can be clearly connected to the CV peaks; similarly to $C_{60}$, a possible explanation could be that some surface reactions happening during CV do not happen in the bulk[92].

From GCP, a loss of capacity in $C_{60}$ electrodes is observed, which could be due to the formation of the solid-electrolyte interphase (SEI) during the first cycle[104], but is probably not enough to justify the high loss of capacity in $C_{60}$, since the reversibility of $C_{60}H_x$ is higher. This suggests that other irreversible processes occur while intercalating sodium in $C_{60}$, as for example the formation of stable polymeric $Na_xC_{60}$ phases, while in $C_{60}H_x$ polymerization is not possible due to the fact that bonds of carbon atoms are completely saturated. This is confirmed by post-mortem XRD: the formation of such a high number of different $Na_xC_{60}$ phases in $C_{60}$ is due to the inhomogeneous intercalation of sodium, probably due to the slow diffusion of $Na^+$, as also observed with EIS. The cause of such slow diffusion could be the formation of the monoclinic polymer $Na_4C_{60}$: in *fcc* crystals, hopping between neighbouring tetrahedral and octahedral sites takes place through trigonal channels[92], which could be closed in the monoclinic phase. In the cubic $Na_2C_{60}$ and $Na_6C_{60}$, diffusion of sodium between sites has been reported, albeit at temperatures higher than 400 K[105][106]; ion mobility in $Na_6C_{60}$ has been studied through NMR, which is probably not sufficient to prove ionic conductivity, since mobility of sodium is probed in the time scale of the microseconds, and mobility at faster time scales, necessary for ionic conductivity, is still unknown. No evidence of $Na^+$ diffusion in $Na_4C_{60}$ has ever been reported, probably due to the fact that in the 2-dimensional polymer the hopping of sodium is hindered[107], which could justify the electrochemical intercalation irreversibility[92].

On the contrary, post-mortem XRD on $C_{60}H_x$ shows a more homogeneous intercalation than that of $C_{60}$. This could be due to the fact that hydrogenation of $C_{60}$ determines an expansion in the crystal lattice, granting larger hopping pathways, and/or to the fact that hydrogenation hampers the capability of polymerization of $C_{60}$ molecules, since all bonds are saturated by hydrogen atoms[92]. This is in agreement with EIS measurements: large resistivity in $C_{60}$ confirms the nature of the irreversible character after sodium intercalation, while $C_{60}H_x$ shows a better ion diffusion, in agreement with GCP and with the homogeneous phase observed with XRD. The SEI resistance of $C_{60}$, of 1660 $\Omega$, is larger than that of $C_{60}H_x$, equal to 730 $\Omega$[92]; this suggests the formation of a thicker SEI layer in $C_{60}$, which could be caused by a non-negligible diffusivity of $C_{60}$ in PEO-based electrolytes[108].

Ball-milling treatment was effective in realizing a solid solution of $C_{70}$ into $C_{60}$ crystal structure. Three main concerns have to be addressed about ball-milled fullerene mixture. The first is the risk of breaking the fullerene cage during high-energy ball-milling, with a consequent amorphization of the sample, as reported in [109]. In our case, crystallinity of the sample is preserved at least in part, since the peaks of fullerene crystal structure are still present; however, some amorphization occurs, as signaled by the appearance of a broad peak at 20° (Figure 5.1). In [109], a planetary ball-milling treatment, which showed a complete destruction of the fullerene cages, was also proven by the appearance of the (0 0 2) reflection of graphite at about 25°[109], not observed after the present treatment. The second concern is the segregation of $C_{60}$ and $C_{70}$, which could crystallize back into two different phases after dissolution in N-methyl-pyrrolidone (NMP) and consequent drying, necessary for the realization of electrodes. As shown in Figure 5.1 (b), no significant difference is observed between ball-milled mixture peaks before and after recrystallization, signifying that fullerene mixture is dispersed in NMP without any dissolution occurring; therefore, the crystals are preserved. The only noticeable difference is the decrease of the intensity at 20°, attributed to an amorphous fraction, which could be due to the fact that amorphous carbon is not well dispersed in NMP, thus being separated from fullerene mixture when taken from a flask prior to casting onto the current collector. Lastly, it has been reported in [59] that ball-milling treatment can cause a polymerization between $C_{60}$ and $C_{70}$ molecules. MAS-NMR proves the absence of such polymerization, since no signature of polymerization was observed in the NMR spectrum (Figure 5.2)[93], in the form of peaks in the range between 0 and 100 ppm, corresponding to $sp^3$ carbon. All chemical shifts of $C_{60}$ and $C_{70}$ are consistent with those reported in [110]. One peak at about 143.5 ppm, not ascribable to $C_{60}$ or $C_{70}$, is due to unremoved solvent traces; this is proven by the sharpness of the peak, typical of liquids[93].

Similarly to $C_{60}$, several potential plateaus are present in the GCP of ball-milled mixture, not observed with non ball-milled mixture; this could be due to the fact that ball-milled mixture has the same *fcc* crystal structure as $C_{60}$, while non ball-milled mixture is made of two different phases, and plateaus could be unobservable because the contributions coming from different phases are probably merged. Surprisingly, plateau potentials of ball-milled mixture are quite higher than those observed for pure $C_{60}$[93]. This may be due to the fact that the significantly higher strain of the $C_{70}$ molecules enhances its electron affinity, with respect to $C_{60}$ molecules, so that reduction potentials switch to higher potentials; the lower potential reduction peak, however, has approximatively the same potential as $C_{60}$, which could be due to the fact that the effect of the strain is compensated by a lower presence of the more electronegative pyracylene bonds in $C_{70}$[111]. Similarly to $C_{60}$, fullerene mixture shows a strong irreversible character, albeit reversibility is higher than that of pure $C_{60}$, hinting at the fact that $C_{70}$ is more reversible than $C_{60}$. Ball-milled mixture shows an even higher reversibility, proving that disorder introduced by mechanical alloying of $C_{60}$ and $C_{70}$ reduces the formation of stable, irreversible phases[93].

## 5.2 Magnesium-ion batteries

### 5.2.1 Characterization of half-cells

Similarly to sodium-ion batteries, $C_{60}$ fullerene is a good candidate as anode in magnesium-ion batteries, thanks to the large interstitial voids in its crystal structure and to its tendency to accept electrons. Magnesium-ion half-cells with electrodes based on $C_{60}$ were studied by means of cyclic voltammetry (CV) and galvanostatic chronopotentiometry (GCP), with the aim of understanding the intercalation mechanism of magnesium in fullerene and of developing new battery technologies based on magnesium. To enhance the specific capacity and increase the reversibility, the same strategy employed for sodium-ion batteries has been applied, adopting $C_{60}H_x$ and fullerene mixture, exploiting the expansion of the crystal structure, the increase in crystal disorder and the absence of polymerization between fullerene molecules. A proper electrolyte, capable of transferring $Mg^{2+}$ ions without solid-electrolyte interphase (SEI) formation, was synthesized and employed[18].

### Cyclic voltammetry

CV was performed on $C_{60}$- and $C_{60}H_x$-based electrodes, in order to better understand magnesium insertion and extraction mechanisms and to obtain information on the intercalation potentials. For $C_{60}$, during the first sweep from high to low voltage, one reduction peak is observed at 1.42 V, with possibly a less evident second one at 0.55 V. During the second sweep, back to a higher potential, one oxidation peak, corresponding the the reduction peak at 1.42 V, is distinguishable (Figure 5.12 (a)). In the case of magnesium intercalation in $C_{60}$, no multiple, equally spaced peaks are present, contrary to what has been observed for sodium in $C_{60}$. Above 2.4 V, a large oxidation peak is observable during both the first and second oxidation sweep. Given the broad shape of the peaks, its presence also in the CV of both mixture and milled mixture, and the fact that it happens only during oxidation, the nature of such peak is probably an undesired reaction of the electrolyte due to a too high potential. $C_{60}H_x$, during the first reduction sweep, is characterized by three different electrochemical reactions, at 1.64 V, 1.18 V and 0.78 V, two of which are still present during the second reduction (Figure 5.12 (b)). Unfortunately, no peaks are observable in the oxidation reaction, denoting that reactions are not reversible, maybe due to the fact that magnesium ions are highly reactive, and could irreversibly bond with $C_{60}H_x$ molecules.

CV for non ball-milled fullerene mixture is shown in Figure 5.13 (a). The reduction sweep is characterized by two peaks at 1.28 V and 0.87 V; only the peak at 1.28 V has an oxidation counterpart, although the peak intensity is far lower than the reduction peak, meaning that the reaction is not fully reversible. On the contrary, CV for ball-milled mixture is characterized by a small peak at 0.62 V, which disappears after the first reduction, and a single, reversible peak at 1.21 V. An anomaly is observed in the case of ball milled mixture. Two broad peaks, ascribable to undesired reactions in the electrolytes, can be observed during oxidation when potential exceeds 2 V. A similar peak is observed also during $C_{60}$ oxidation and, to a lesser extent, also for non ball-milled mixture. However, such effect does not compromise battery performance during GCP, since all cells were charged up to potential values lower than or equal to 2 V. Among the electrode materials tested with CV, ball-milled mixture features the highest reversibility.

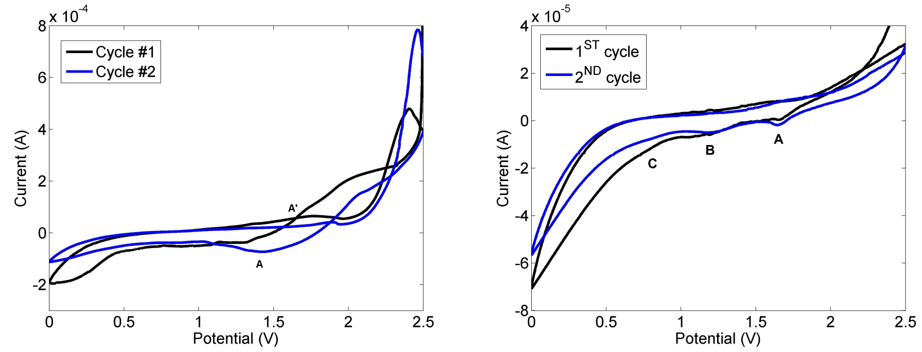

(a) (b)

Figure 5.12: Cyclic voltammetry of $C_{60}$ (a) and $C_{60}H_x$ (b) based magnesium-ion half-cells.

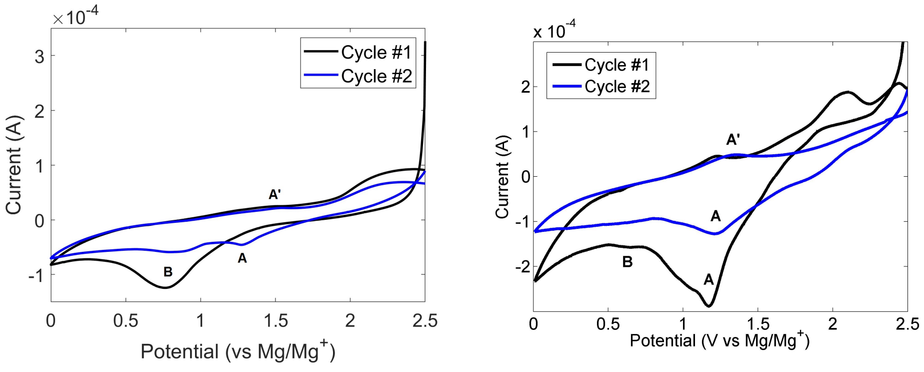

(a) (b)

Figure 5.13: Cyclic voltammetry of Mg-ion half-cells with electrodes based on fullerene mixture (a) and ball-milled mixture (b).

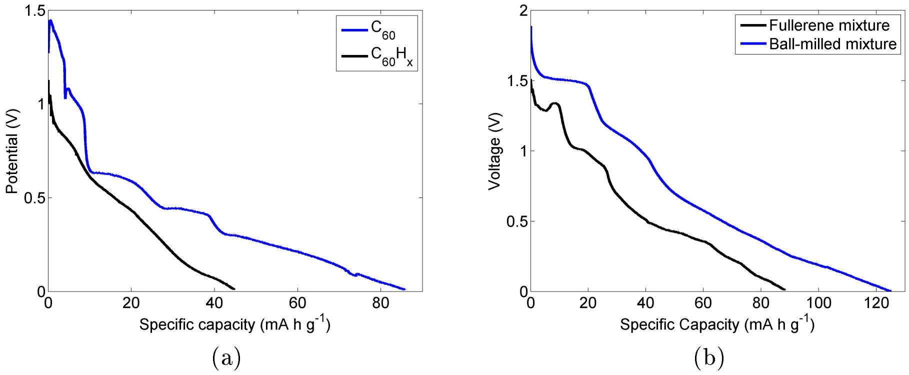

(a) (b)

Figure 5.14: (a) OCV of half-cells with electrodes of $C_{60}$ and $C_{60}H_x$ during the first discharge semicycle. (b) OCV of fullerene mixture and ball-milled mixture based half-cells with respect to the specific capacity, during the first discharge semicycle.

### Galvanostatic chronopotentiometry

GCP was employed to probe the performance of magnesium-ion half-cells with electrodes based on $C_{60}$, $C_{60}H_x$, fullerene mixture and ball-milled mixture. $C_{60}$ and $C_{60}H_x$ half-cells were discharged and charged with a slow C-rate of C/30 (a current such that the cell is completely discharged in 30 hours), in order for the discharge curve to be a good approximation of an open circuit voltage (OCV) curve. During the first GCP discharge, $C_{60}$ and $C_{60}H_x$ electrodes show a specific capacity of respectively 44.7 mA h $g^{-1}$ and 85.7 mA h $g^{-1}$ (Figure 5.14 (a)), corresponding to a stoichiometry of $Mg_{0.6}C_{60}$ and $Mg_{1.2}C_{60}H_x$, respectively. Both electrodes are characterized by several plateaus of the potential, each standing for a different electrochemical reaction. The $C_{60}$-based electrode shows at least five plateaus, at about 1.3 V, 1 V, 0.6 V, 0.4 V and 0.2 V, while $C_{60}H_x$-based electrode shows three, at about 0.8 V, 0.6 V and 0.1 V

Non ball-milled fullerene mixture is characterized by a specific capacity of 88.2 mA h $g^{-1}$ during the first cycle, and GCP curve that resembles that of pure $C_{60}$ (Figure 5.14 (b)). At least three plateaus are observed, at 1.3 V, 1 V, 0.4 V, with possibly another plateau at low voltage. Moreover, the same anomaly observed in pure $C_{60}$ is also present. Electrodes based on ball-milled fullerene mixture show a first cycle discharge specific capacity of 125 mA h $g^{-1}$, corresponding to 1.7 magnesium ions per fullerene molecule, with at least two different plateaus at 1.5 V and 1.1 V; the latter can be attributed to the CV potential peak at 1.17 V. Capacity retention for cycles subsequent to the first is shown in Figure 5.16.

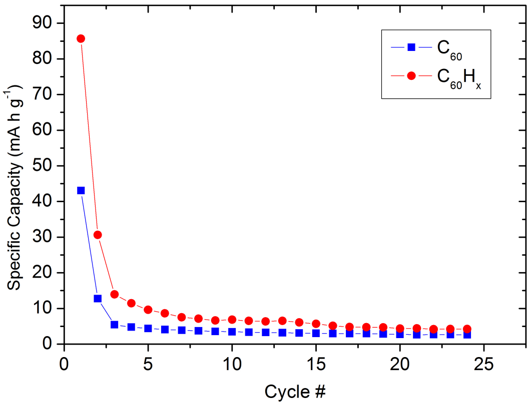

Figure 5.15: Specific capacity of Mg-ion half-cells with electrodes of $C_{60}$ and $C_{60}H_x$ during the first 25 cycles.

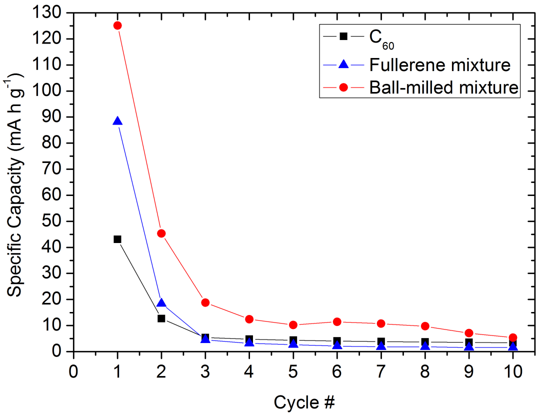

Figure 5.16: Specific capacity of Mg-ion half-cells with electrodes of $C_{60}$, fullerene mixture and ball-milled mixure during the first 10 cycles.

### 5.2.2 Discussion

GCP performed on $C_{60}$ shows several potential plateaus, corresponding to different redox reaction. This is in contrast with the fact that just one peak is observed through CV, which could be due to the fact that the first reaction observed in CV at 1.42 V, probably corresponding to the 1.3 V plateau of GCP, is an intermediate step required for the subsequent reactions to occur, and that CV is too fast for magnesium to completely intercalate the surface of the electrode. $C_{60}$ electrode is characterized by an anomaly at about 1.1 V: potential initially decreases during discharge, then rises, and after a small plateau starts decreasing again. This anomaly is probably due to a phase transition of $C_{60}$, due to the intercalation of magnesium and the consequent reorganization of the crystal structure, but could also be caused by a local polarization of the electrode due to a slow charge transfer dynamic of magnesium into the electrode. Reversibility of the process is quite low (Figure 5.15); the formation of stable polymeric $Mg_2C_{60}$[112] could be the reason for both the low reversibility and the slow formation of the compound, which hinders the formation of other compounds during CV. $C_{60}H_x$ plateaus are far less evident than those of $C_{60}$; moreover, initial specific capacity of $C_{60}H_x$ is much lower than those of pure $C_{60}$, in contrast to what observed in sodium-ion half cells, in which initial specific capacity is quite similar. Among the plateaus in $C_{60}H_x$ discharge, at about 0.8 V, 0.6 V and 0.1 V, only the one at 0.8 V has a counterpart in the cyclic voltammetry, which is barely recognizable in the first reduction of the CV (labelled with letter C). Contrarily to $C_{60}$, no anomaly was observed during discharge.

The close similarity between both CV and GCP of fullerene mixture and pure $C_{60}$, hints at the fact that *hcp* $C_{70}$ gives little to no contribution to magnesium intercalation. However, both CV and GCP of ball-milled mixture are characterized by redox reactions which are quite different from those of $C_{60}$ and non ball-milled mixture, having different intercalation potentials and not showing the potential recovery at 1.1 V in GCP, proving that ball-milling of $C_{60}$ and $C_{70}$ is effective in enhancing specific capacity, despite $C_{70}$ alone seems to intercalate only a small amount (or no amount at all) of magnesium. Moreover, ball-milled mixture has a higher capacity than the other electrodes even for the subsequent cycles (Figure 5.16), and the enhancement in reversibility is probably due to the same reason for which it also occurred in sodium-ion batteries: solid solution of $C_{60}$ and $C_{70}$ is effective in expanding free space in the crystal and in preventing polymerization between fullerenes.

## 5.3 Lithium-ion batteries

From previous studies, it has been demonstrated that graphene is a good candidate as anode in lithium-ion batteries, thanks to its high specific capacity and fast charge-discharge rate capabilities[21]. Lithium-ion half-cells with electrodes based on thermally exfoliated graphite oxide (TEGO) were assembled and characterized by means of galvanostatic chronopotentiometry (GCP) and electrochemical impedance spectroscopy (EIS): the aim of this work has been that of studying the performance of graphene produced with a scalable method and to better understand lithium intercalation and diffusion mechanisms. Moreover, hydrogenated TEGO (H-TEGO) was synthesized and characterized, the role of the hydrogen being that of removing oxygen atoms and saturating dangling bonds, which are a consequence of the synthesis process. Full-cells with TEGO and H-TEGO based electrodes were also realized, coupling for the first time the novel, scalable anode materials with electrodes made with three different commercial cathode materials. All lithium-ion batteries were assembled and characterized at the Center for Automotive Research of The Ohio State University in Columbus, Ohio, United States of America.

### 5.3.1 Characterization of electrode materials

DC conductivity of TEGO was measured, in order to understand if graphene can work in batteries without the use of a conductive agent. A conductivity of 9.4±0.1 S $cm^{-1}$ was observed, enough to justify the making of the electrode without carbon black. XRD was performed on graphite powder (starting material for the realization of TEGO and H-TEGO), on GO and exfoliated TEGO (Figure 5.17). The main peak of graphite, corresponding to the (0 0 2) reflection, is shifted in GO towards smaller angles, meaning that oxidation was successful in increasing the distance between graphite sheets. After thermal exfoliation, graphene sheets detach from each other, giving a mostly amorphous XRD pattern. the broad peak in TEGO pattern, falling at approximatively the same angle as the (0 0 2) peak of graphite, is proof of the fact that few layered graphite (up to about 5 layers[81]) is present in the sample along with monolayer graphene.

### 5.3.2 Characterization of half-cells

#### Galvanostatic chronopotentiometry

GCP was employed to measure the performance of lithium-ion half-cells with electrodes based on TEGO and H-TEGO, which were discharged and charged at different C-rates; the slowest C-rate of 0.1 C was employed in order to have a good approximation of the open circuit voltage (OCV) curves, while faster C-rates were employed to study the fast charge and discharge capability of the electrodes. Before actual GCP at different rates of charge and discharge, an optimization of the electrode binder was needed: most TEGO and H-TEGO electrodes were characterized by poor mechanical robustness, due to

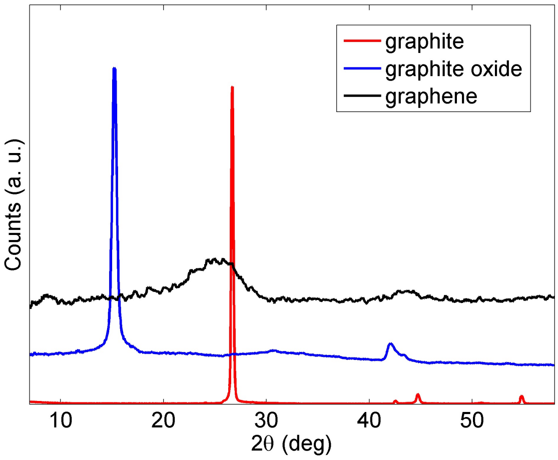

Figure 5.17: XRD of graphite precursor, graphite oxide and TEGO.

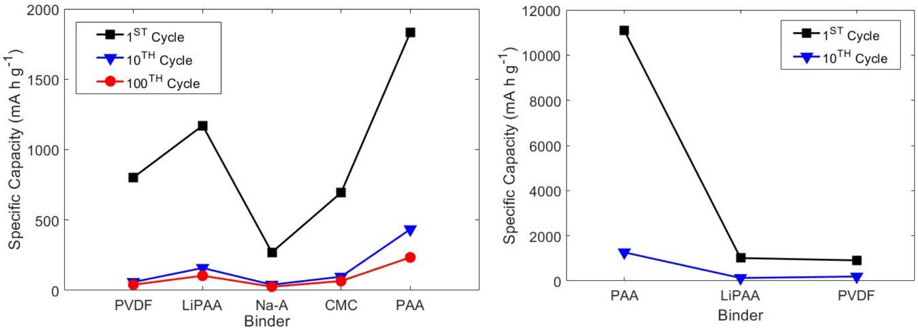

(a) (b)

Figure 5.18: Specific capacity of half-cells with TEGO (a) and H-TEGO (b) based electrodes with different binders, for the first and subsequent cycles.

the large volume expansion of TEGO and H-TEGO after dispersion in N-methyl-pyrrolidone (NMP), with the consequence of formation of cracks in the electrode during the drying process or after the assembly of the cells, which resulted in a loss of specific capacity during GCP. Many different binders were employed: for TEGO, polyacrilic acid (PAA), Polyvinylidene fluoride (PVDF), carboxymethyl cellulose (CMC), sodium alginate (Na-A) and lithium polyacrilic acid (LiPAA); for H-TEGO, PAA, LiPAA, and PVDF. After some trial-and-error attempts and GCP measurements on electrodes with different binders, PAA was chosen as the best binder, both from the point of view of mechanical resistance and electrode performance (Figure 5.18).

Both TEGO and H-TEGO are characterized by a different GCP curve between the first discharge and the subsequent ones. In particular, TEGO and

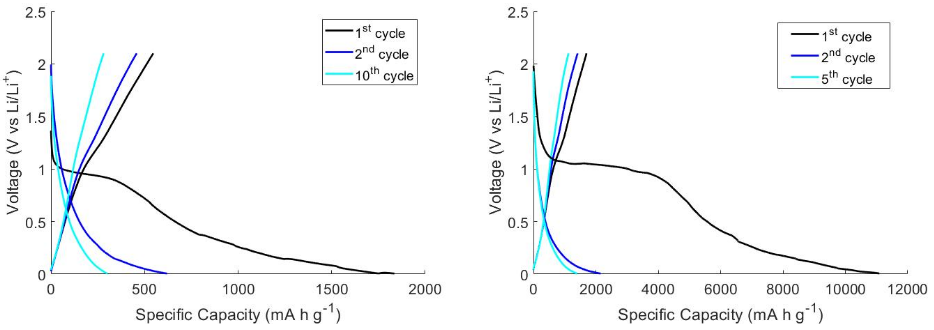

(a) (b)

Figure 5.19: OCV of half cells with electrodes based on TEGO (a) and H-TEGO (b) as a function of the specific capacity, measured with a low rate of charge (0.05 C for TEGO, 0.1 C for H-TEGO), for the first and subsequent cycles.

H-TEGO electrodes are characterized by a single plateau at about 1 V during the first discharge, with a specific capacity exceeding 1 500 mA h g$^{-1}$ for TEGO and 10 000 mA h g$^{-1}$ for H-TEGO, and subsequent cycles with a steeply decreasing discharge curve, which is atypical for batteries (Figure 5.19). The reason for such differences is in the fact that both TEGO and H-TEGO are characterized by a very large specific surface area, which relates to the interface between the electrode and the electrolyte. For this reason, the effect of the solid-electrolyte interphase (SEI) formation is more pronounced than in conventional electrodes, and most of the specific capacity observed during the first cycle is not actually an intercalation process; the single plateau probably corresponds to the SEI formation reaction interface.

Subsequent cycles are characterized by a steeply decreasing shape of the potential curve, with a low potential as that of graphite, but at the same time different in the fact that in graphite the potential suddenly drops to a low potential plateau (Figure 5.27 (a)). A low specific capacity, with respect to the first cycle, is observed. Since the high first-cycle specific capacity is actually due to SEI formation, the real specific capacity of TEGO and H-TEGO is probably that of the cycles from the second onward. Specific capacity of TEGO after the first cycle, of about 304±14 mA h g$^{-1}$, obtained for a C-rate of 0.1 C (a current such that the cell is completely discharged in 10 hours), is similar to that of graphite (Figures 5.20 (a) and (b)). Specific capacity is retained even at high C-rates, the most extreme being 25 C (a current such that the cell is completely discharged in 1/25 hours), in which an average capacity of 109±3 mA h g$^{-1}$ is observed. H-TEGO is by far more performing (Figure 5.21 (a) and (b)): for a low C-rate of 0.1 C specific capacity is 1290±60 mA h g$^{-1}$, and 360±20 mA h g$^{-1}$ for an extreme C-rate of 25 C. For the case of 1 C, the observed specific capacity is 670±40 mA h g$^{-1}$.

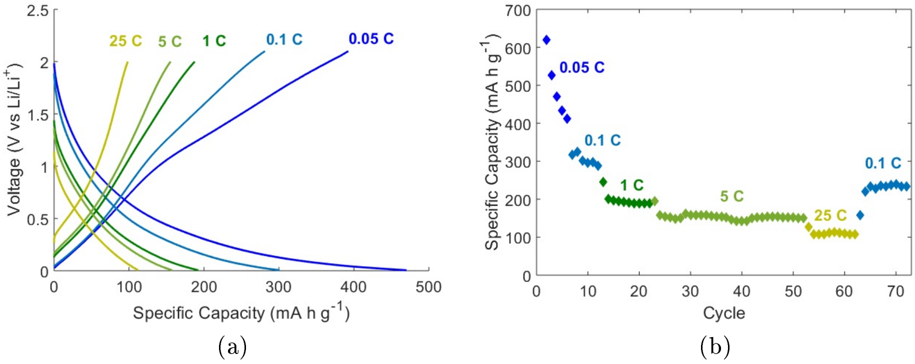

Figure 5.20: OCV of half cells (a) and comparison of discharge specific capacity at different rates of discharge (b) with electrodes based on TEGO.

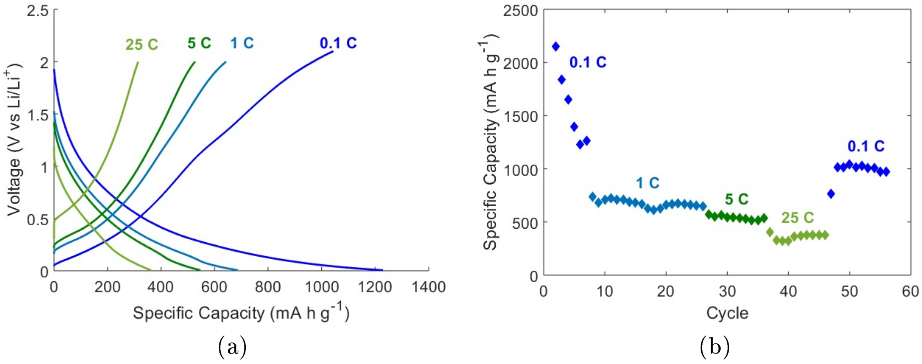

Figure 5.21: OCV of half cells (a) and comparison of discharge specific capacity at different rates of discharge (b) with electrodes based on H-TEGO.

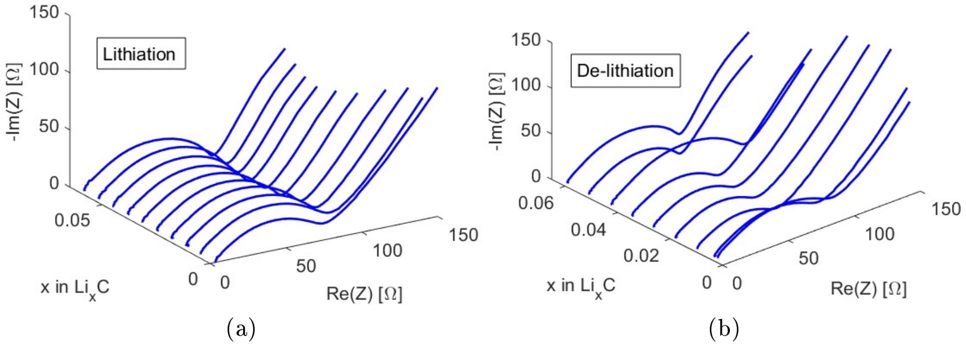

(a) (b)

Figure 5.22: Nyquist plot for EIS performed on half-cells based on TEGO at different stages of lithiation (a) and de-lithiation (b).

### Impedance spectroscopy

EIS measurements on half-cells with electrodes based on TEGO and H-TEGO were performed at a constant temperature of 25 °C and at different SOC conditions, by galvanostatically charging and discharging the cells for 10% of their total capacity between each EIS measurement, in order to study diffusion dynamics in graphene-based electrodes at each stage of intercalation and explain the steeply decreasing behaviour of the discharge GCP curve. Nyquist plots for EIS performed on TEGO, as a function of the content of lithium in the electrode, are shown in Figure 5.22 (a) for the lithiation process and in Figure 5.22 (b) for the de-lithiation process, while Nyquist plots for lithiation and de-lithiation of H-TEGO are shown in Figures 5.22 (a) and (b), respectively. In general, lithiation process seems to be more regular than de-lithiation process, since Nyquist plots are much more similar to each other.

Diffusion coefficient of lithium in TEGO and H-TEGO has been calculated from EIS as a function of the content of lithium in the electrode (Figures 5.24 (a) and (b)). The equivalent circuit employed to model the system is shown in the inset of Figure 5.24 (a). $R_e$ is the resistance of the external circuit, $R_{ct}$ is the charge transfer resistance between the electrode and the electrolyte, $Z_w$ is the Warburg impedance and *CPE* is a constant phase element impedance taking into account the geometrical capacity of the system. Diffusion coefficient is calculated from the Warburg coefficient and the OCV curve, obtained from the GCP potential acquired before each EIS measurement, by using the 4.12 equation. Both electrodes are characterized by a very different diffusion coefficient between lithiation and de-lithiation. This is probably due to the unconventional shape of the OCV curve of TEGO and H-TEGO, which, instead of displaying the typical plateau of battery electrodes, feature a steeply

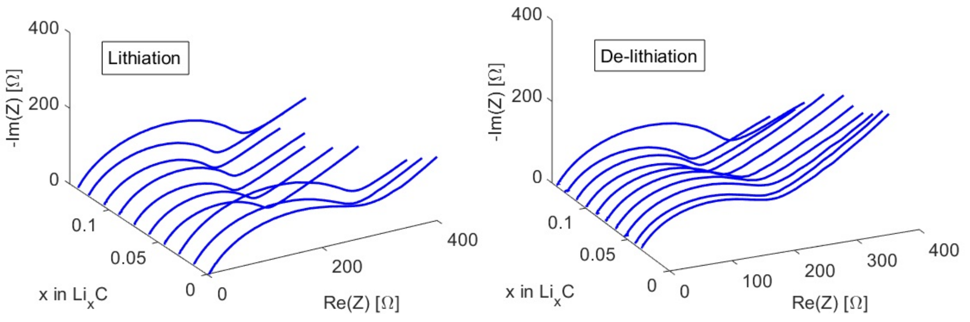

(a) (b)

Figure 5.23: Nyquist plot for EIS performed on half-cells based on H-TEGO at different stages of lithiation (a) and de-lithiation (b).

decreasing behaviour during discharge (lithiation) and an approximatively linear behaviour during charge (de-lithiation), as seen in Figures 5.20 and 5.21. This causes a significant difference in the derivative of the OCV with respect to the lithium content in the electrode, while the Warburg coefficient is more regular (Figures 5.25 (a) and (b)).

### 5.3.3 Electrochemical characterization of full-cells

Full-cells were realized by coupling TEGO and H-TEGO with different cathode materials. Due to the large quantity of lithium consumed by the anode during the first cycle, all anodes underwent a pre-lithiation process, which consists in assembling the anodes in half cells and cycling three times, after which the anodes are removed from the half-cells and employed to assemble the full-cells. This method is different than that reported in [30] for a similar system, and has the advantage of allowing the formation of a more complete SEI, since it was observed that formation of SEI requires more than one cycle to complete. Evidence that SEI is preserved after disassembling the half-cells is reported in [28]. By means of GCP, electrochemical performance of full-cells was studied. Different rates of charge and discharge were employed, in order to obtain both a good approximation of the OCV curve, and the change in capacity corresponding to high current rates. Galvanostatic potential as a function of state of charge for full-cells with TEGO and H-TEGO based anode, probed at 0.1 C, is shown in Figures 5.27 (b), 5.28 (a) and 5.28 (b), respectively with lithium nickel manganese cobalt (NMC), lithium cobalt oxide (LCO) and lithium iron phosphate (LFP) cathodes. All the full-cells are characterized by a similar behaviour: the absence of evident plateaus and values of potential spanning a wide voltage range. No evident difference is

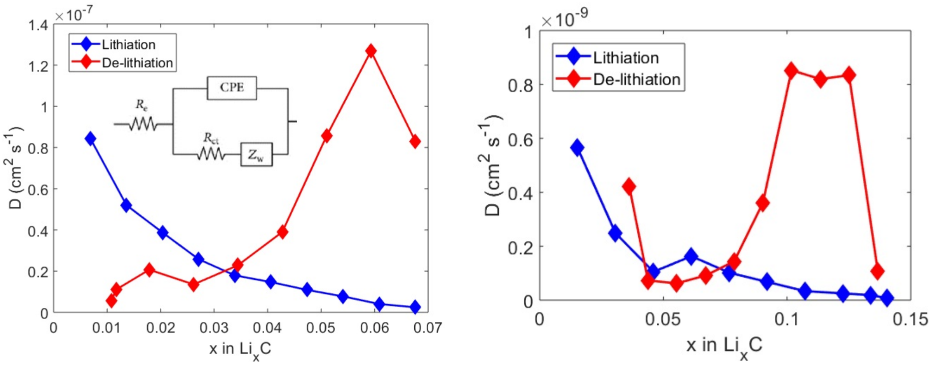

(a) (b)

Figure 5.24: Diffusion coefficient of lithium in TEGO (a) and H-TEGO (b), at different stages of lithiation and de-lithiation. Inset: equivalent circuit model employed to analyze the EIS data.

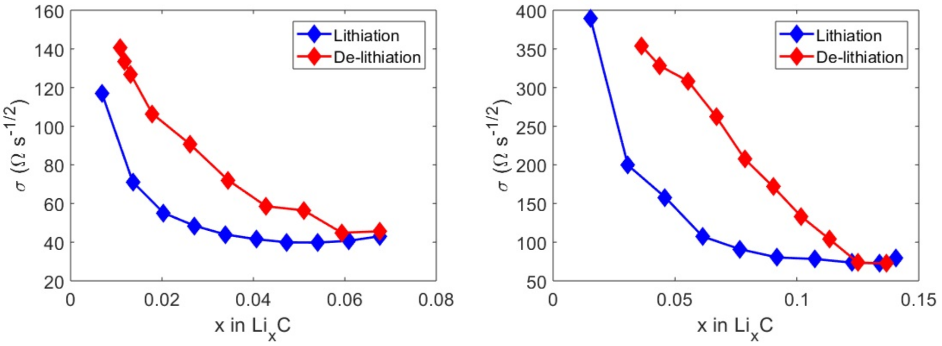

(a) (b)

Figure 5.25: Warburg coefficient calculated from EIS for lithium in TEGO (a) and H-TEGO (b), at different stages of lithiation and de-lithiation.

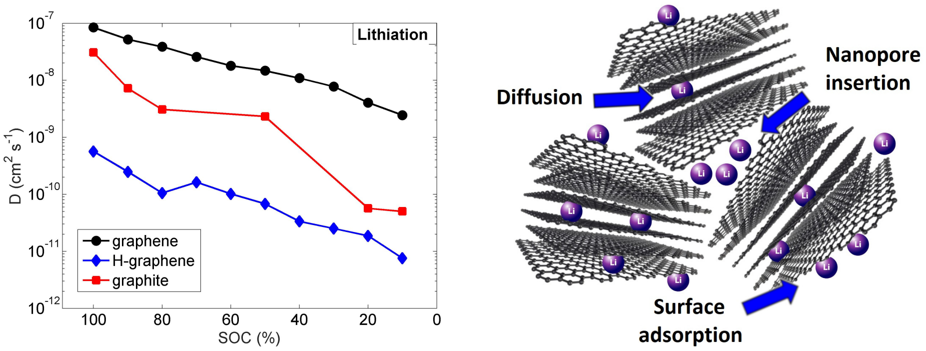

(a) (b)

Figure 5.26: (a) Comparison between diffusion coefficient in TEGO and H-TEGO calculated at different stages of lithiation. (b) Possible explanation of the difference in diffusion between TEGO and H-TEGO.

observed between the potential of TEGO and H-TEGO during charge and discharge.

### NMC

Figure 5.29 shows the specific capacity of full-cells with TEGO and H-TEGO based anodes and NMC-based cathodes. Cells have been initially charged and discharged at 0.1 C, and then either charged at a higher C-rate while keeping at 0.1 C the C-rate for the discharge, or discharged at a higher C-rate while keeping at 0.1 C the C-rate for the charge. For the cell based on TEGO, a high retention of capacity is observed when charging at a fast C-rate, up to 5 C, and discharging at a low C-rate, while capacity drops significantly when charging at 25 C. When discharging at a fast C-rate, capacity drops faster, showing a capacity significantly lower the initial one even at 5 C. This considerable drop in specific capacity is probably due to the cathode, since fast C-rate capabilities of TEGO (as well as H-TEGO) were observed in the half-cells. The drop in specific capacity from the first cycle to the subsequent one is probably due to an incomplete formation of the SEI, since the initial specific capacity is much higher than expected, too close to that observed for the first cycle of TEGO-based half-cells. Since the amount of lithium initially present in the cathode isn't enough to justify such a specific capacity, lithium is probably supplied by the electrolyte; this is undesireable, since removing too much lithium from the electrolyte may lead to malfunction of the battery. For the full cells with electrodes based on H-TEGO and NMC, capacity retention is more stable than that of the TEGO-based full-cell, since no significant difference is observed between fast discharge and fast charge. However, initial

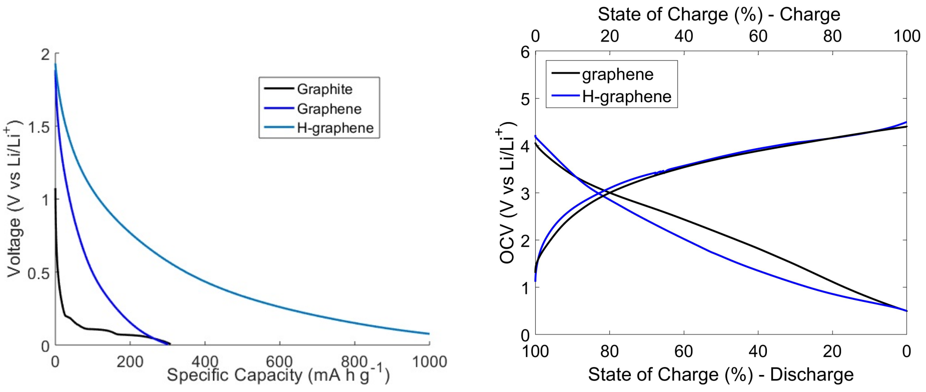

(a) (b)

Figure 5.27: (a) Comparison between OCV vs specific capacity curves of TEGO, H-TEGO and graphite. (b) OCV as a function of state of charge for full-cells with either TEGO or H-TEGO anode and NMC cathode.

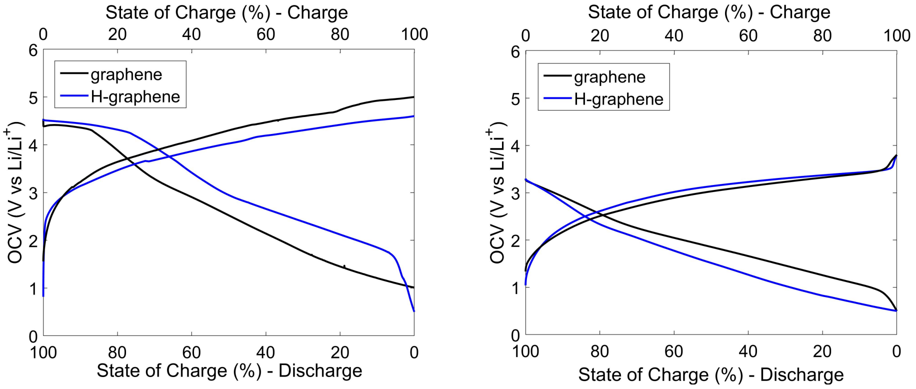

(a) (b)

Figure 5.28: (a) OCV as a function of state of charge for full-cells with either TEGO or H-TEGO anode and LCO cathode. (b) OCV as a function of state of charge for full-cells with either TEGO or H-TEGO anode and LFP cathode.

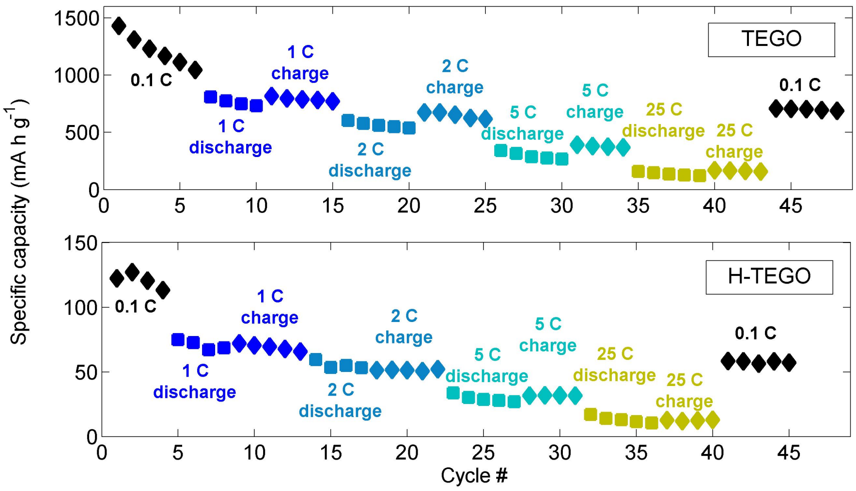

Figure 5.29: Specific capacity of the anode at different rates of charge and discharge for full-cells with either TEGO or H-TEGO anode and NMC cathode.

specific capacity is much lower than both that of the TEGO-based full-cell and that observed for H-TEGO half-cell; three different full-cells were assembled, but two of them were characterized by a low capacity, while the third failed.

## LCO

LCO-based full cells with TEGO and H-TEGO anodes are characterized by a less evident difference between fast charge and fast discharge (Figure 5.30); however, as for NMC-based cells, a significant drop in capacity is observed for C-rates equal to or higher than 5 C. Since the fast rate capabilities of TEGO and H-TEGO were already studied in half-cells, this is again due to the effect of the cathode, which limits the maximum current. It is also worth noting that all the 5 full-cells with TEGO-based anode and LCO-based cathode failed before the 35$^{th}$ cycle. This could be due to the fact that $LiCoO_2$ is unstable at a potential higher than 4.2 V, and at a high charge rate the electrode potential may be locally higher than the measured one, due to a polarization effect caused by ohmic drop.

## LFP

Lastly, the GCP capacity at different C-rates for full-cells with LFP cathode and either TEGO or H-TEGO anode is shown in Figure 5.31. Cycles in which full-cells are subject to a fast charge and slow discharge show a better

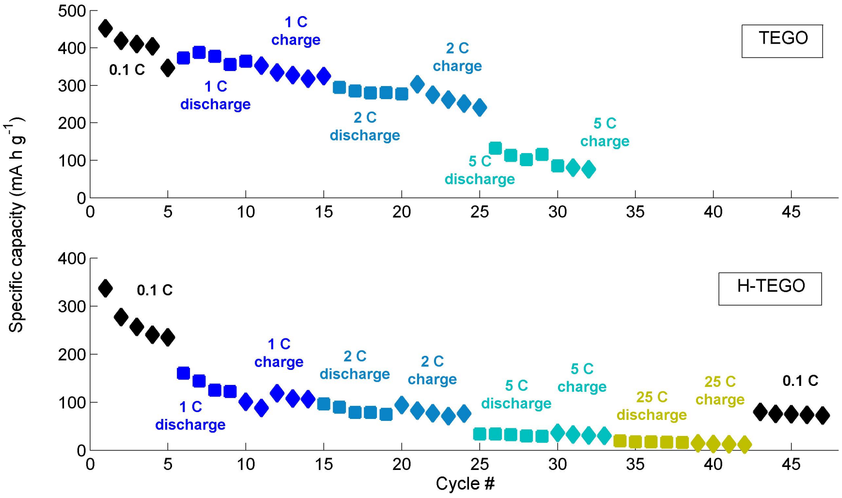

Figure 5.30: Specific capacity of the anode at different rates of charge and discharge for full-cells with either TEGO or H-TEGO anode and LCO cathode.

capacity than those in which cells are more rapidly discharged, suggesting that, since this is not observed in LCO-based devices, the cathode is the cause of the capacity decrease. The full-cell with H-TEGO anode and LFP cathode features the best performance among all the full-cells that have been studied, with an anodic specific capacity of 366±11 mA h g$^{-1}$ at low charge and discharge rate, and a still high 305±16 mA h g$^{-1}$ when charging at 5 C, although performance drops significantly at 25 C, probably due to a limit of the cathode, as observed in all the full-cells.

### 5.3.4 Discussion

Graphene-based electrodes, and in particular H-TEGO electrodes, are characterized by a large reversible specific capacity, despite the fact that the first discharge is dominated by the formation of a massive SEI layer. Discharge and charge GCP curves have an unconventional shape, characterized by the absence of plateaus, for both TEGO and H-TEGO. Two significant differences are observed between TEGO and H-TEGO. The first is the larger specific capacity of H-TEGO, calculated from GCP; the second is the diffusion coefficient of lithium in the electrode, calculated from EIS. In particular, while diffusion in TEGO is about 10 times higher than that of graphite, diffusion in H-TEGO is actually much lower, about 10 times lower than graphite and 100 times lower than TEGO. This is quite surprising, since H-TEGO displayed the best performance during GCP tests, both in term of specific capacity and retention of capacity during fast charge-discharge cycles, the latter of which should denote fast diffusion dynamics. Such behaviour has an explanation:

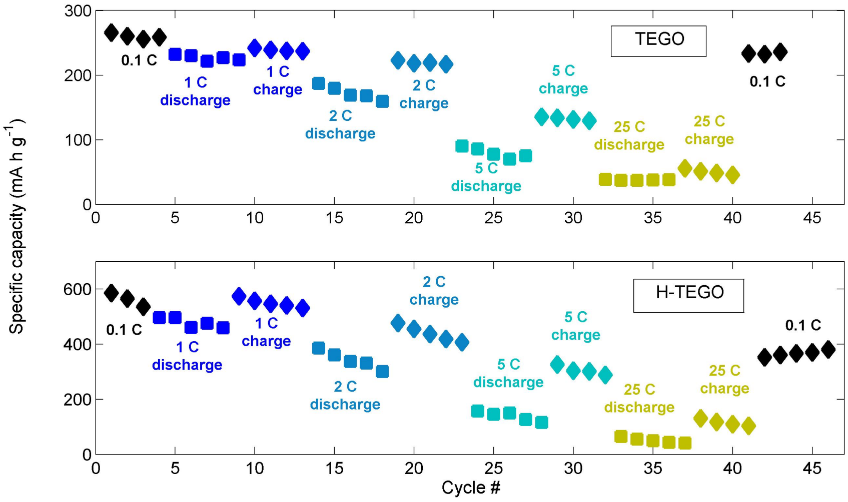

Figure 5.31: Specific capacity of the anode at different rates of charge and discharge for full-cells with either TEGO or H-TEGO anode and LFP cathode.

diffusion in TEGO is higher than that in graphite since TEGO is composed by small flakes of one to few layers graphene, and lithium can rapidly move in the innermost core of the flakes by crossing the space between planes, while in graphite, to completely intercalate the bulk, the distance between the core and the edges of the planes is longer. In H-TEGO, diffusion between layers is probably hindered by the presence of electron-positive hydrogen or other functional groups on the surface and/or on the edges of each graphene plane. The fast charge and discharge is then probably not caused by diffusion of lithium inside graphene layers, which is a chemical process, but by a physical, intrinsically faster, process, as adsorption on the surface of graphene or inside the pores of the graphene matrix (Figure 5.26 (b)). This explanation is supported by previous NMR studies on the insertion and extraction of sodium ions in TEGO[28]; despite the active ions are different, lithium is chemically similar to sodium, which could explain the similarity in the charge accumulation behaviour. In particular, NMR performed on sodium in TEGO electrodes proved the existence of three different insertion mechanisms: one consists in the intercalation of sodium between layers, one corresponds to the insertion inside the nanopores, and one is attributed to the formation of the SEI, which is confirmed by the irreversibility of the process. The electrostatic capacitive charge accumulation effect, corresponding to the insertion inside the nanopores is the explanation for the high charge and discharge rates of both TEGO and H-TEGO, and is probably not observed in the EIS characterization, since the impedance of the process is probably orders of magnitude lower than that of electrochemical intercalation.

The idea of a physical charge accumulation process is proven by the atypical shape of the GCP curves, which is similar to galvanostatic charge and discharge curves of electrochemical double layer capacitors (EDLCs), especially for the approximatively linear charge curves[113][114]. Specific capacity calculated for TEGO and H-TEGO is actually much larger than that of typical EDLCs[115][114], but similar to that of batteries; for this reason, the explanation for the performance of TEGO and H-TEGO electrodes is that the fast charge and discharge rate capability is probably given by the fast, physical electrostatic charge accumulation, while the high capacity is given by the slower, electrochemical charge accumulation. This has been observed before in [116], although in that case graphene was employed only to provide the electrostatic charge accumulation, while the electrochemical charge accumulation was provided by $Mg_2Ni$; on the contrary, in TEGO and H-TEGO based electrodes the graphene-related materials provide both the faster electrostatic accumulation and the slower electrochemical accumulation, probably thanks to the fact that TEGO and H-TEGO are made of both single and multiple graphene layers (up to 3-5 layers), and lithium can be electrochemically intercalated between graphene layers in non-single layer graphene.

Full-cells with TEGO and H-TEGO anodes are characterized by a surprising absence of plateaus, typical of all cathode materials; plateaus should be at 3.8 V for NMC, 4.2 V for LCO and 3.4 V for LFP. Instead, cells seems to be fully charged at the same potential as the theoretical plateau potential of the cathode; their potential keeps on decreasing up to a lower limit of 1 V. This is due to the fact that the potential of the cell is given by the difference between the potential of cathode and that of the the anode. When charging or discharging, the potential of the cathode is almost constant, since it is dominated by the plateau, but the potential of the anode changes, as observed for the GCP curves of the TEGO and H-TEGO half-cells; as a consequence, the cell potential is not constant and no plateaus are observed, but instead the difference in potential is dominated by the potential of TEGO and H-TEGO, known from GCP performed on the half-cells.

## 5.4 Solid electrolytes

Solid electrolytes are one possible solution to many of the safety problems of batteries, such as toxicity and possibility of leaks and of ignition[31]. Complex metal hydrides, like $LiBH_4$, are characterized by a fast ionic conductivity but only at high temperatures. Some fullerene-based compounds, like $Li_4C_{60}$[36], are characterized by a high room temperature ionic conductivity, although with a possible concurrent non-negligible electronic conductivity. Composites of borohydrides and fullerides were synthesized, with the aim of enhancing room temperature ionic conductivity of borohydrides and of reducing possible electronic contributions to conductivity of fullerides. Moreover, a gel electrolyte, made by combining a $Mg(AlCl_2BuEt)_2$-polyvinylidene fluoride composite with $C_{60}$, was synthesized and characterized, with the aim of enhancing ionic conductivity, as reported in a lithium-ion ionic conductor[39].

### 5.4.1 Borohydride composites

Lithium borohydride-lithium fulleride and sodium borohydride-sodium fulleride composites were synthesized via solid-state reaction. Ionic conductivity of all materials was calculated by means of electrochemical impedance spectroscopy (EIS). Crystal structures of $Li_4C_{60}$-$LiBH_4$ and $Li_6C_{60}$-$LiBH_4$ were also characterized through X-ray diffraction (XRD).

#### Impedance spectroscopy

Ionic conductivity of $Li_xC_{60}$-$LiBH_4$ composites was measured by means of EIS, in the temperature range of 300-420 K. Three different composites were synthesized, each with a different $Li_xC_{60}$ (x=4,6,12) fulleride. Such composites are characterized by the typical EIS tail in the Nyquist plot (an example is shown in Figure 5.32 (a)), signature of ionic conductivity without electronic conductivity, calculated by using the model shown in the inset of Figure 5.32 (a). Each composite is compared to pure $LiBH_4$ in Figure 5.32 (b). Each new composite is effective in increasing room temperature ionic conductivity of lithium borohydride, the best one being $Li_6C_{60}$-$LiBH_4$ with $6.2 \cdot 10^{-6}$ S cm$^{-1}$, as opposed to pure $LiBH_4$ with barely $6.5 \cdot 10^{-8}$ S cm$^{-1}$ and pure $Li_6C_{60}$ with $1.3 \cdot 10^{-6}$ S cm$^{-1}$. $LiBH_4$ still features the best performance after the phase transition at 420 K, at which temperature ionic conductivity of each composite is below that of $LiBH_4$, with the exception of an ionic conductivity of $6.5 \cdot 10^{-4}$ S cm$^{-1}$ for $Li_{12}C_{60}$-$LiBH_4$, which is almost the same as that of $LiBH_4$.

Since $Li_xC_{60}$-$LiBH_4$ composites are more effective in improving $LiBH_4$ conductivity at room temperature than at higher temperatures, and since producing all solid-state commercial batteries is still a challenge, due to room temperature low conductivity of solid electrolytes, the best room temperature performing composite, $Li_6C_{60}$-$LiBH_4$, was further optimized, by changing either the duration of the annealing process, or the relative amount of fulleride added to the borohydride. Three different annealing temperatures were investigated: 2 h, 24 h and 48 h (Figure 5.33 (a)). The shortest treatment, of just 2 h, seems to be too short to effectively enhance ionic conductivity: at a first glance, room temperature conductivity seems higher than that of lithium borohydride, but in fact low temperature conductivity is quite similar to that of pure $Li_6C_{60}$, while high temperature behaviour resembles that of $LiBH_4$. Consequently, $Li_6C_{60}$-$LiBH_4$ composite is not formed and probably

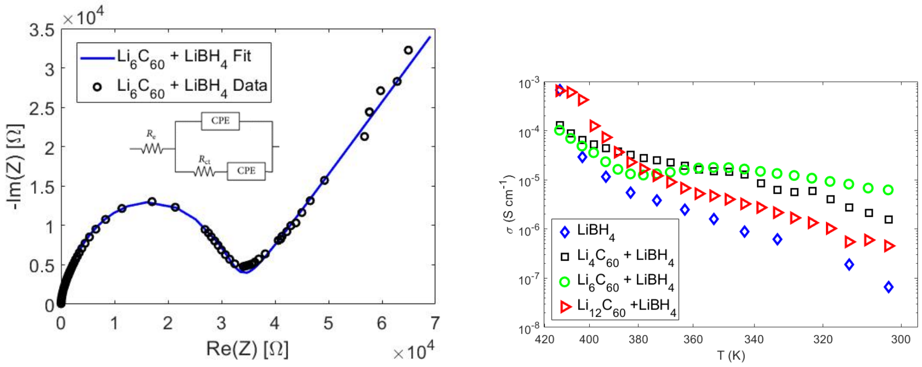

(a) (b)

Figure 5.32: (a) Nyquist plot of the EIS performed on $Li_6C_{60}$-$LiBH_4$ at room temperature. Inset: equivalent circuit employed to model the systems. (b) Comparison between the ionic conductivity of $LiBH_4$ and of three different composites of $LiBH_4$, with either $Li_4C_{60}$, $Li_6C_{60}$, or $Li_{12}C_{60}$ in a 50%-50% ratio.

precursors are still segregated. On the contrary, annealing temperatures of 24 h and 48 h do not show any difference either in the low and in the high temperature behaviour; however, the phase transition temperature is shifted at lower temperatures, at about 240 K, for the 48 h treatment sample. Lastly, three different ratios of $Li_6C_{60}$:$LiBH_4$ (75:25, 50:50, 25:75) were employed, with annealing time of 24 h (Figure 5.33 (b)). $Li_6C_{60}$:$LiBH_4$ ratio of 75:25 features the best performance, with a room temperature ionic conductivity of 5.9 $\cdot 10^{-5}$ S cm$^{-1}$, 1000 times higher than pure $LiBH_4$ and 50 times higher $Li_6C_{60}$. Hopping activation energy is 320±10 meV.

EIS was also performed on $Na_6C_{60}$-$NaBH_4$ composite in the temperature range of 300-400 K; the presence of a small tail in the Nyquist plot suggests that the composite is an ionic conductor (Figure 5.34 (a)), although it is not as evident as for $Li_6C_{60}$-$LiBH_4$. Figure 5.34 (b) shows the ionic conductivity of the composite before and after annealing, calculated by using the model shown in the inset of Figure 5.34 (a). Ionic conductivity of annealed $Na_6C_{60}$-$NaBH_4$ composite ranges from 4.8$\cdot 10^{-5}$ S cm$^{-1}$ at room temperature, up to 1.4$\cdot 10^{-3}$ S cm$^{-1}$ at 400 K; hopping activation energy is 640±20 meV at low temperatures.

### Structural characterization

Powder XRD was performed on the most interesting sample, $Li_6C_{60}$-$LiBH_4$, in order to check if the enhanced ionic conductivity is the result of an embedding of $C_{60}$ in the $LiBH_4$ structure, as reported in [39], of an amorphization of the sample, or if an entirely new crystal structure is produced. Evidence of the formation of a new crystal structure is observed in the XRD pattern:

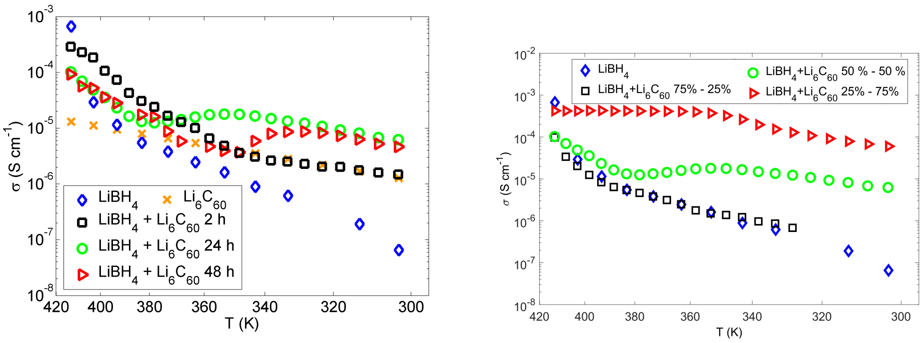

(a) (b)

Figure 5.33: (a) Comparison between the ionic conductivity of $LiBH_4$, $Li_6C_{60}$ and of three different composites of $LiBH_4$ with $Li_6C_{60}$ in a 50%-50% ratio, treated at 220 °C for 2, 24 or 48 h. (b) Comparison between the ionic conductivity of $LiBH_4$ and of three different composites of $LiBH_4$ with $Li_6C_{60}$, with three different ratios: 25%-75%, 50%-50%, or 75%-25%.

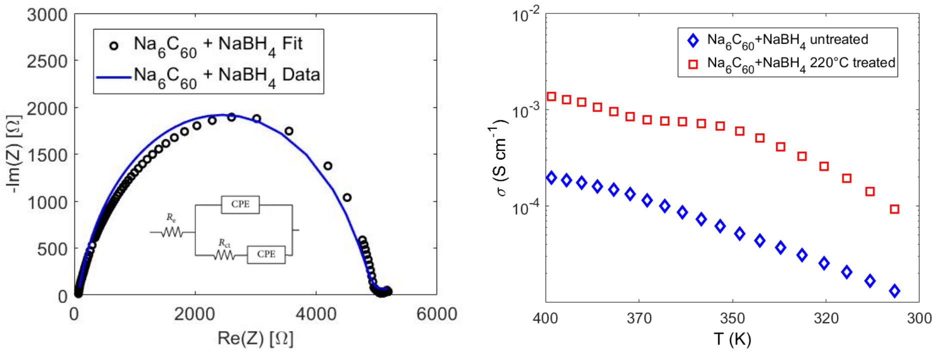

(a) (b)

Figure 5.34: (a) Nyquist plot of the EIS performed on $Na_6C_{60}$-$NaBH_4$ at room temperature. Inset: equivalent circuit employed to model the systems. (b) Ionic conductivity of $Na_6C_{60}$-$NaBH_4$ composite before and after thermal treatment.

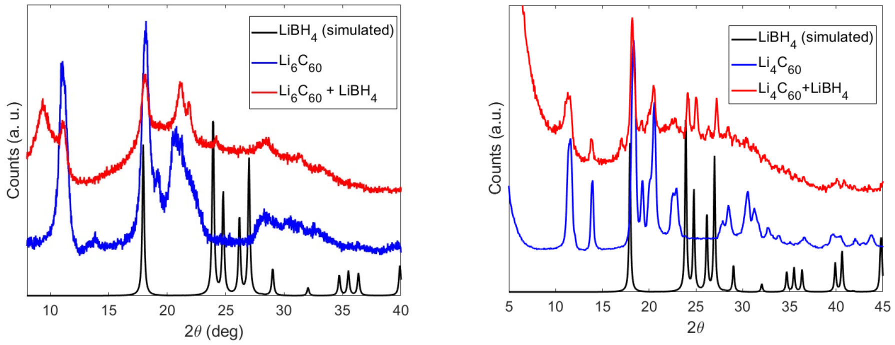

(a) (b)

Figure 5.35: (a) XRD of $Li_6C_{60}$-$LiBH_4$ compared to the starting materials. (b) XRD of $Li_4C_{60}$-$LiBH_4$ compared to the starting materials.

at least two new peaks are visible, at 9.4° and 21.8°, while most of the peaks of $LiBH_4$ disappear, at 24.8°, 26.1° and 27.0° (Figure 5.35 (a)). None of such peaks is ascribable to any other phases of $LiBH_4$; consequently, it is possible that $LiBH_4$ form an alloy with $Li_6C_{60}$, in which $BH_4^-$ ions substitute $C_{60}$ molecules.

Powder XRD was also performed on $Li_4C_{60}$-$LiBH_4$, in order to check if also the second best composite gives rise to a new crystal structure. In this case all the peaks of the starting materials are observed in the final composite (Figure 5.35 (b)), contrarily to the case of $Li_6C_{60}$-$LiBH_4$, in which $LiBH_4$ peaks were not observable in the composite material; moreover, only one new peak is observed at 17.0°, which could be ascribable to a spurious signal. It is possible that the fullerene molecules in $Li_4C_{60}$, strongly bound by covalent bonds, cannot react with $LiBH_4$. The high ionic conductivity of the composite could be due to the already high ionic conductivity of $Li_4C_{60}$[36].

### 5.4.2 $Mg(AlCl_2BuEt)_2$ composite

Ionic conductivity of $Mg(AlCl_2BuEt)_2$-polyvinylidene fluoride (PVDF) gel composite was measured by means of EIS, in the temperature range of 300-400 K. Conduction of ions is proven by the presence of a typical tail in the Nyquist plot (Figure 5.36 (a)). An ionic conductivity ranging from $2{\cdot}10^{-7}$ S cm$^{-1}$ at room temperature up to $5.2{\cdot}10^{-5}$ S cm$^{-1}$ at 400 K was observed (Figure 5.36 (b)), and was calculated by using the model shown in the inset of Figure 5.36 (a). Following the same route of conductivity enhancement of polyethylene oxide (PEO), nanostructured $Al_2O_3$ was added to the solution. An increase in conductivity was observed, although room temperature ionic conductivity was unchanged. Moreover, a decrease of conductivity at

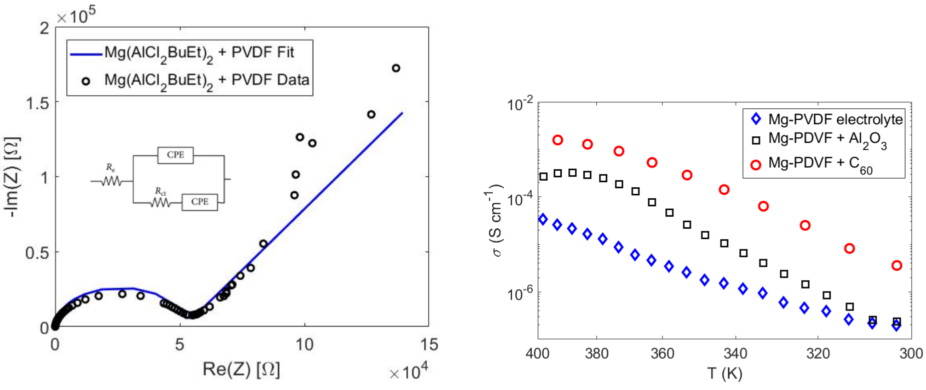

(a) (b)

Figure 5.36: (a) Nyquist plot of the EIS performed on $Mg(AlCl_2BuEt)_2$-PVDF composite at room temperature. Inset: equivalent circuit employed to model the systems. (b) Comparison between ionic conductivity of $Mg(AlCl_2BuEt)_2$-PVDF gel composite with and without $Al_2O_3$ or $C_{60}$ additives.

temperatures higher than 380 K was also observed, deviating from the expected linear behaviour in an Arrhenius plot, probably due to a degradation of the electrolyte at high temperature. $C_{60}$ was also studied as an additive in $Mg(AlCl_2BuEt)_2$-PVDF, following the route of [39], and compared to the starting electrolyte. An increased ionic conductivity of $3.6 \cdot 10^{-6}$ S cm$^{-1}$ at room temperature, up to $2.3 \cdot 10^{-3}$ S cm$^{-1}$ at 400 K, was observed.

### 5.4.3 Discussion

$Li_6C_{60}$-$LiBH_4$ (75%-25% in weight) was found to be the best ionic conductor at room temperature, with an ionic conductivity of $5.9 \cdot 10^{-5}$ S cm$^{-1}$. However, it is also the worst one at high temperature, due to a phase transition at about 360 K, after which ionic conductivity drops, deviating from the expected linear behaviour. Above 380 K, ionic conductivity is linear again, but with a different slope, proving the formation of a new phase with a different activation energy required for ion hopping. $Li_6C_{60}$-$LiBH_4$ also featured a new crystal phase, observed though XRD. It is possible that the new crystal structure corresponds to an alloy in which $BH_4^-$ ions substitute fullerene molecules; since $BH_4^-$ ions are smaller than $C_{60}$, the enhancement in ionic conductivity is probably due to the larger space available to lithium ions, allowing easier hopping processes. Although the formation of a new phase seems in contrast with [39], where the reduction of $C_{60}$ is reported in $C_{60}$-$LiBH_4$ composite, in $Li_6C_{60}$-$LiBH_4$ fullerene molecules have their lowest unoccupied molecular orbitals (LUMO) completely filled, so no further reduction is permitted upon reaction with $LiBH_4$. Sadly, it is not possible to index the novel crystal structure, mainly due to both the not sufficient quality of the XRD signal, and the presence of the peaks of unreacted $Li_6C_{60}$. Such unreacted precursor material hints at the fact that finding the right stoichiometric ratio, rather than the employed empirical ratio, of $Li_6C_{60}$:$LiBH_4$ would be needed in order to achieve the highest ionic conductivity and a good XRD pattern for the new compound.

Similarly to $Li_6C_{60}$-$LiBH_4$, the sodium-based composite material after annealing is characterized by a phase transition at about 360 K, which determines an initial decrease of conductivity, followed by a recovery of the normal behaviour. It is worth noting that no comparison between $Na_6C_{60}$-$NaBH_4$ composite and its precursors is possible, since both $Na_6C_{60}$ and $NaBH_4$ are bad ionic conductors at low temperatures, with a conductivity too low to be measured by the impedance analyser. It is then safe to assume that, contrarily to what happens in $Li_6C_{60}$-$LiBH_4$, ball-milling itself is enough to produce a composite material, since a good ionic conductivity is observed even before annealing. It is possible that even in $Li_6C_{60}$-$LiBH_4$ the composite is produced before annealing, it being chemically very close to $Na_6C_{60}$-$NaBH_4$. Since in the case of untreated $Li_6C_{60}$-$LiBH_4$ no improvements in ionic conductivity is observed, it is possible that only a fraction of the starting materials reacts to form the composite during ball-milling, maybe at the grain boundaries: as such, no increase in ionic conductivity is observed, since both $Li_6C_{60}$ and $LiBH_4$ are characterized by room temperature conductivity, while for the sodium composite the enhancement is more evident, since both starting materials are ionic insulators. Reducing grain size would probably allow an increase of ionic conductivity in $Li_6C_{60}$-$LiBH_4$ even without annealing, but increasing ball-milling time is not possible, since longer milling can result in an amorphization of the composite, due to the break of $C_{60}$ molecules[109]. Instead of reducing grain size, a possible future development could be that of alloying $Li_xC_{60}$ or $Na_xC_{60}$ with other boron-based ionic conductor salts, like closo-boranes, in which the anion is characterized by an ionic radius more similar to that of fullerene molecules[117].

# Chapter 6

# Conclusions

The aim of this study has been to address different problems about batteries - performance, safety, materials availability and costs - by exploiting the properties of carbon nanostructured materials such as fullerene and graphene, thanks to their high specific surface area, good electrical conductivity and capability of hosting alkali and alkali-earth ions. In this work, sponsored by C1P8 s.r.l. in order to find new applications for fullerene-related materials, $C_{60}$ was characterized as anode material for sodium-ion (SIB) and magnesium-ion batteries, to better understand the physical process of ion intercalation and to develop new battery technologies. Hydrogenated fullerene and mixture of different fullerene molecules were also studied, in order to enhance specific capacity and increase reversibility, which was found out to be an issue in $C_{60}$-based half-cells. Graphene synthesized with a scalable method was characterized as well as anode material in lithium-ion batteries, in order to better understand intercalation mechanism and to develop a more performing technology for lithium-ion batteries. Graphene was also hydrogenated, in order to remove oxygen atoms and saturate dangling bonds, which are a consequence of the synthesis process. Moreover, for the first time graphene produced by thermal exfoliation and hydrogenated graphene were coupled to suitable cathodes, in order to develop complete prototypes, more similar to a possible commercially viable product. Lastly, solid electrolyte composites with enhanced ionic conductivity were realized and characterized, using lithium and sodium borohydride in conjunction with different fullerene derivatives: $Li_xC_{60}$ (x=4,6,12) and $Na_6C_{60}$. Moreover, a gel electrolyte, made by combining a $Mg(AlCl_2BuEt)_2$-polyvinylidene fluoride composite, was synthesized and characterized, with the aim of enhancing ionic conductivity.

## 6.1 Fullerene-based Na-ion batteries

The electrochemical intercalation of sodium in $C_{60}$, $C_{60}H_x$ (with x$\sim$39) and fullerene mixture, before and after ball-milling, was investigated for the first time by realizing and characterizing all solid-state half-cells. A proper solid electrolyte based on polyethylene oxide (PEO) was developed, to avoid dissolution of the electrode materials in the electrolyte. Six different reversible redox states were observed for $C_{60}$ by means of cyclic voltammetry (CV), some of which were confirmed also by galvanostatic chronopotentiometry (GCP). Interestingly, neighbour redox states are separated by an almost equal potential difference, as already reported in [118]. Some GCP plateaus did not find a matching counterpart in CV peaks, probably due to the fact that cell were studied through 2-electrode CV, which is less accurate than 3-electrode CV. Sodium was successfully intercalated in $C_{60}$, up to 250 mA h $g^{-1}$, corresponding, on average, to a theoretical stoichiometry of $Na_{6.8}C_{60}$, calculated from GCP measurements not taking into account possible side-reactions. However, $C_{60}$ was characterized by a low reversibility, which caused a fast decrease of the capacity. Electrochemical impedance spectroscopy (EIS) measurements highlighted a slow diffusion dynamic of sodium in $C_{60}$-based electrode, which explains the inhomogeneous distribution of intercalation phases observed with post-mortem powder X-ray diffraction (XRD) analysis. The low reversibility is probably caused by a combination of slow mobility of ions and the formation of stable intercalation phases, as the polymeric $Na_4C_{60}$[102], from which extraction of sodium is hindered[92].

Reversibility was successfully increased by exploiting hydrogenated fullerene $C_{60}H_x$ as electrode material. CV shows four different redox states for $C_{60}H_x$, but not equally spaced as in $C_{60}$. GCP shows that a slightly lower amount of sodium can be intercalated in $C_{60}H_x$, with respect to $C_{60}$, up to 230 mA h $g^{-1}$, corresponding, on average, to a stoichiometry of $Na_{6.5}C_{60}H_x$, calculated from GCP measurements not taking into account possible side-reactions. However, reversibility is significantly better, with more than 10% of the initial capacity retained after 20 cycles. Such higher reversibility is ascribable to the higher distance between hydrofullerene molecules, resulting in larger interstitial voids, and to the inability to from covalent bonds between hydrofullerene molecules, impeding the formation of polymeric structures. This is confirmed by the higher mobility of sodium ions, observed with EIS measurements, and by the formation of a single intercalation compound of sodium in $C_{60}H_x$, highlighted by post-mortem XRD, rather than a distribution of different phases as observed for $C_{60}$[92].

Reversibility was also improved by employing electrodes with fullerene mixture, which also has the advantage of being about five times less expensive than fullerene, since the latter is produced by refining fullerene mixture. High-energy ball-milling is capable of producing a novel crystalline phase, with *fcc* symmetry, in which $C_{60}$ and $C_{70}$ form a solid solution, as observed with XRD. Thanks to respectively XRD and nuclear magnetic resonance (NMR) analysis, no significant amorphization or polymerization of fullerenes molecules, which sometimes happens during ball-milling treatments, is observed. The increased disorder of this novel solid solution, as well as the larger average distance between fullerene molecules, promotes the electrochemical properties of ball-milled fullerene electrodes. In particular, a higher specific capacity than both $C_{60}$ and non ball-milled fullerene mixture is measured with GCP, both during the first and the subsequent cycles. A specific capacity of 320 mA h $g^{-1}$ is observed for ball-milled mixture during the first discharge, corresponding to 8.9 sodium ions per fullerene molecule, and a reversibility of 13% for the subsequent discharges is measured[93].

The study of SIB was successful in clarifying the electrochemical intercalation mechanism of sodium in fullerene and fullerene-related materials, and in realizing working all solid-state SIB. Performance of $C_{60}$ does not meet the requirements for practical applications, despite the fact that they are comparable to those of other all solid-state sodium-ion batteries (SIB), which range from a reversible specific capacity of 40 mA h $g^{-1}$[119][53] to a maximum of 100 mA h $g^{-1}$[54], and are still far from commercialization. The two main issues are the low reversibility, even when cycled at a low C-rate, and the shape of the potential curve as a function of the state of charge, which is not constant, as required for a battery electrode, but rather characterized by multiple plateaus. Employing other fullerene-related materials, in particular hydrogenated fullerene and ball-milled mixture, was successful in improving reversibility with respect to pure $C_{60}$. Despite the fact that both hydrogenated fullerene and ball-milled mixture are still characterized by a reversibility which is not sufficient for their use in commercial batteries, it would be interesting to combine the effects of hydrogenation and solid solution of $C_{70}$ in $C_{60}$, and further studies will be performed on sodium-ion batteries with hydrogenated ball-milled mixture anodes. Another possible future development is that of studying intercalation potentials with 3-electrode CV, in order to increase accuracy on redox potentials during reduction/oxidation.

## 6.2 Fullerene-based Mg-ion batteries

The electrochemical intercalation of magnesium in $C_{60}$, $C_{60}H_x$ (with x$\sim$39) and fullerene mixture, before and after ball-milling, was investigated by realizing anodes and characterizing them in half-cells. A proper organo-magnesium electrolyte was synthesized, to avoid the formation of a solid electrolyte interphase (SEI) layer impermeable to magnesium. Contrarily to SIB, just one, slightly reversible redox reaction is observed for $C_{60}$ with CV. Interestingly, several plateaus are observed with GCP, one of which confirming the reaction highlighted by CV. Magnesium was successfully intercalated with a specific capacity up to 44.7 mA h $g^{-1}$, corresponding, on average, to a stoichiometry of $Mg_{0.6}C_{60}$, calculated from GCP measurements not taking into account possible side-reactions. As for SIB, reversibility is quite low, about 8% after 10 cycles. This could be again ascribable to the formation of stable polymeric phases such as $Mg_2C_{60}$.

Reversibility was successfully increased by exploiting hydrogenated fullerene $C_{60}H_x$ as electrode material. CV shows three different redox states for $C_{60}H_x$, although no evidence of reversibility is observed. GCP shows that a higher amount of magnesium, almost double, can be intercalated in $C_{60}H_x$, with respect to $C_{60}$, up to 85.7 mA h $g^{-1}$, corresponding, on average, to a stoichiometry of $Mg_{1.2}C_{60}$, calculated from GCP measurements not taking into account possible side-reactions. Specific capacity is significantly better than that of $C_{60}$ after 10 cycles, with 6.8 mA h $g^{-1}$, and the reasons of such higher performance are probably the same as for SIB: larger space between fullerene molecules and absence of polymer structures.

Similarly to SIB, reversibility was also improved by employing electrodes with the less expensive fullerene mixture, by exploiting the solid solution between $C_{60}$ and $C_{70}$ obtained with high-energy ball-milling. Also in this case, the increased disorder of this novel solid solution, as well as the larger average distance between fullerene molecules, promotes the electrochemical properties of ball-milled fullerene electrodes. CV demonstrates that contribution of $C_{70}$ is negligible for non ball-milled mixture, while a reversible redox reaction is observable for ball-milled mixture. A higher specific capacity than both $C_{60}$ and non ball-milled fullerene mixture is measured with GCP, both during the first and the subsequent cycles. In particular, a specific capacity of 125 mA h $g^{-1}$ is observed for ball-milled mixture during the first discharge, corresponding to 1.7 magnesium ions per fullerene molecule, and a specific capacity of 9.7 mA h $g^{-1}$ after 20 cycles.

The study of magnesium-ion batteries was successful in electrochemically intercalating fullerene and fullerene-related materials with magnesium, and in clarifying it insertion/extraction mechanism. Similarly to sodium-ion fullerene batteries, the two main issues are the low reversibility and the non-flat shape of the potential curve as a function of the state of charge, characterized by multiple plateaus. The employment of other fullerene-related materials, in particular hydrogenated fullerene and ball-milled mixture, was successful in improving first discharge specific capacity and subsequent cycles reversibility, with respect to pure $C_{60}$. This constitutes an improvement to the performance reported in [25], which led to a Toyota patent[26], in which fullerene-based magnesium-ion batteries featured a first discharge specific capacity of 50 mA h $g^{-1}$. Moreover, in our work electrodes were composed of a majority of fullerene or fullerene-related materials, as opposed to [25], in which barely a 35% of the electrode was made of $C_{60}$. Similarly to sodium-ion batteries, the increase in reversibility is still not high enough to justify their use in commercial batteries, but the combination of the effects of hydrogenation and solid solution of $C_{70}$ in $C_{60}$ could further improve reversibility, and will require more studies, along with 3-electrode CV to better determine the potentials of the redox reactions.

## 6.3 Graphene-based Li-ion batteries

Research on graphene-based lithium-ion batteries was carried out in collaboration with the Center for Automotive Research of The Ohio State University in Columbus, Ohio, United States of America. The electrochemical intercalation of lithium in thermally exfoliated graphite oxide (TEGO) and hydrogenated TEGO (H-TEGO) was investigated by realizing and characterizing half-cells with anodes based on TEGO and H-TEGO. Lithium was successfully intercalated in TEGO, with a reversible specific capacity of 304 mA h $g^{-1}$ at 0.1 C. TEGO proved to be especially good for its high charge and discharge rate capabilities, retaining nearly 36% of capacity even at an extreme C-rate of 25 C, both during charge and discharge. H-TEGO featured an even more outstanding performance, with a reversible specific capacity of 1290 mA h $g^{-1}$ at 0.1 C, of 670 mA h $g^{-1}$ at 1 C and of 360 mA h $g^{-1}$ at 25 C. Thanks to such an amazing performance, TEGO and especially H-TEGO should definitively be considered as anode materials for lithium-ion batteries.

Diffusion of lithium in TEGO and H-TEGO was studied with EIS analysis. A diffusion coefficient of $2{\cdot}10^{-8}$ $cm^2$ $s^{-1}$ at half SOC, about 10 times higher than that of graphite, was calculated for TEGO, while a diffusion coefficient of $1{\cdot}10^{-10}$ $cm^2$ $s^{-1}$ was calculated for H-TEGO. It has been reported in [119] that charge transfer impedance of the lithium-electrolyte interface in half-cells is non-negligible and that it possesses a time constant similar to that of the anode-electrolyte charge transfer; consequently, the contribution of the charge transfer mechanisms are irresolvable. However, all the half-cells tested with EIS were prepared in the same conditions, so it is safe to assume that the contribution of the lithium-electrolyte interface is similar for each cell, thus allowing a comparison between the charge transfer impedance and diffusion coefficents of TEGO, H-TEGO and graphite. Moreover, while diffusion should be dependent on the state of charge of the anode, charge transfer resistance of lithium is theoretically independent from the state of charge, so the behaviour of the diffusion coefficient as a function of the state of charge is reliable. The slower diffusion dynamics of H-TEGO, while also being capable of fast charging and discharging, and the shape of the GCP curves, suggests the simultaneous occurrence of two distinct phenomena: battery-like electrochemical intercalation, due to lithium insertion between graphene layers, and supercapacitor-like electrostatic accumulation of charges, due to lithium adsorbed into graphene pores or attracted by electrical charges on graphene surface. The fast charge and discharge capability is given by the supercapacitor-like accumulation, while the high specific capacity is given by the slower battery-like transfer of lithium ions between graphene layers. Such effect has been reported before[116], but only in systems in which the electrode is made by two different components; in the case of TEGO and H-TEGO, it is the first time in which this effect is observed in a single component, which provides both contributions to charge accumulation.

For the first time graphene produced with a highly scalable thermal exfoliation and hydrogenated graphene have been coupled to a cathode in full-cells, which were studied by means of GCP; either lithium nickel manganese cobalt oxide (NMC), lithium cobalt oxide (LCO) or lithium iron phosphate (LFP) have been employed as cathodes. The best performance has been obtained for full-cells with LFP, and in particular for the cell coupling H-TEGO with LFP, probably due to the faster rate capabilities of the cathode, with an anodic specific capacity of 305 mA h $g^{-1}$ with a charge rate of 5 C. Such a good performance makes graphene a very interesting candidate as anode for lithium-ion batteries; however, before exploiting TEGO or H-TEGO in commercial batteries, three main issues have to be addressed. Firstly, graphene-related materials, due to their high specific surface area, give rise to a massive SEI[28]. Besides the resulting waste of lithium, a large quantity of lithium can cause a faster ageing of the battery, so further studies on ageing effect on graphene electrodes are needed. The second issue is that a higher than normal variance of the electrodes' specific capacity is observed. This could be due to the hand-made nature of the cells, but could also be caused by intrinsic inhomogeneities of the electrode materials. Lastly and more importantly, the main issue is the slope of the OCV curve, which does not present plateaus, but rather a surprising hysteresis, with an almost linear behaviour during discharge, typical for supercapacitors, and a steeply increasing behaviour during charge, which could be the effect of the combined supercapacitive and redox effects. Such behaviour could be the solution to some typical problems of existing technologies. The first is the fact that plateau potential of graphite is very close to zero vs $Li/Li^{+}$; this may cause the formation of a metallic lithium plating on the anode[120], which results in the death of the battery, and typically happens when charging and discharging the battery at high current rates, due to the potential drop caused by the internal resistance of the battery. The second is the fact that some cathode materials, among which LFP, has a very flat plateau in the OCV curve, which makes really hard to estimate the state of charge of the battery from the potential. For LFP in particular, for a change in potential of 1 mV, the corresponding change in SOC is of 0.4% for most of the discharge curve[121], without even taking into account potential changes due to temperature changes, drift currents and ageing[122]. These two problems could be solved by TEGO or H-TEGO, but the issue of the non-flat potential must be solved. One strategy is that of assembling a battery with an unbalanced ratio of cathode and anode: for example, if the graphene needed to balance the capacity of the cathode is doubled, its contribution to the potential difference of the cell is halved; the potential range of the battery can also be controlled by assembling the battery with graphene in a partially lithiated stage, so that the potential difference of the cell is always in the higher half. The proposed method for pre-lithiation grants enough control on the level of lithiation of the anode material, to tune the exact state of charge needed before assembling the full-cell.

## 6.4 Fullerene-based solid electrolytes

Composite lithium or sodium solid electrolytes based on borohydrides and fullerides were synthesized and studied through EIS and XRD analysis, and magnesium gel electrolytes based on $Mg(AlCl_2BuEt)_2$ and polyvinylidene fluoride (PVDF) was synthesized and studied through EIS analysis. Different $LiBH_4$ composites were tested, changing either the $Li_xC_{60}$ (x=4,6,12) fulleride compound, the annealing time or the ratio between the borohydride and the fulleride. The best composite is $Li_6C_{60}$-$LiBH_4$, featuring a room temperature ionic conductivity of $5.9 \cdot 10^{-5}$ S $cm^{-1}$. What is most interesting is the formation of a new compound, observed with powder XRD analysis, although crystal structure has yet to be indexed, and will require further investigation. All $Li_6C_{60}$-$LiBH_4$ compounds featured a phase transition between 350 and 400 K; such phase transition will require more study by means of XRD. $Na_6C_{60}$-$NaBH_4$ was also synthesized, for which a room temperature ionic conductivity of $4.8 \cdot 10^{-5}$ S $cm^{-1}$ was observed, although ionic conductivity signature is not as clear as those of the other solid electrolytes and will require further investigation.

Lastly, a room temperature ionic conductivity of $3.6 \cdot 10^{-6}$ S $cm^{-1}$ was observed for $Mg(AlCl_2BuEt)_2$-PVDF gel electrolyte with the addition of fullerene, whereas ionic conductivity without fullerene is barely $1.9 \cdot 10^{-7}$.

All novel ionic conductors are characterized by a high room temperature ionic conductivity, which makes them good candidates for solid-solid state batteries. More studies are required to better optimize their performance, in particular to find the exact ratio of reagents, which has been so far chosen empirically.

# Bibliography

[1] BP statistical review of world energy 2019, 2019. (Citato alle pagine 1, 50).

[2] Steinke, F., Wolfrum, P. and Hoffmann, C. Grid vs. storage in a 100% renewable europe. *Renewable Energy*, 2013. (Citato a pagina 2).

[3] Li, Q., Chen, J., Fan, L., Kong, X. and Lu, Y. Progress in electrolytes for rechargeable Li-based batteries and beyond. *Green Energy and Environment*, 2016. (Citato a pagina 2).

[4] Scott, A. Counting the ways to store renewable energy. *Chemical and engineering news*, 2018. (Citato a pagina 2, 2).

[5] Huggins, R. A. *Advanced batteries - Materials science aspects.* Springer, 2009. (Citato alle pagine 2, 11, 12, 12, 32, 33, 33, 46).

[6] Tarascon, J. M. and Armand, M. Issues and challenges facing rechargeable lithium batteries. *Nature*, 2001. doi: 414(6861):359-367. (Citato alle pagine 2, 9).

[7] Akridge, J. and Brodd, R. Pacific power symposium, 2010. (Citato a pagina 2).

[8] Panasonic NCR18650PF. https://industrial.panasonic.com, 2019. (Citato a pagina 2).

[9] Zhu, X., Guo, Z. and Hou, Z. Solar-powered airplanes: A historical perspective and future challenges. *Progress in aerospace sciences*, 2014. (Citato alle pagine 2, 4).

[10] Balakrishnan, P. G., Ramesh, R. and Kumar, T. P. Safety mechanisms in lithium-ion batteries. *Journal of Power Sources*, 2006. (Citato a pagina 2).

[11] EU Science Hub. Li-ion batteries can have a second life as energy storage. https://ec.europa.eu/jrc/en/science-update/li-ion-batteries-second-life-energy-storage, 2018. (Citato a pagina 3).

[12] Samco technologies. https://www.samcotech.com, 2019. (Citato a pagina 3).

[13] U. S. Geological survey. Commodity summaries. http://minerals.usgs.gov/minerals/pubs/commodity/lithium/, 2016. (Citato alle pagine 3, 12).

[14] Slater, M. D. and Kim, D. and Lee, E. and Johnson, C. S. Sodium-ion batteries. *Advanced functional materials*, 2013. (Citato alle pagine 3, 12, 13, 13, 13).

[15] Railsback, L. B. Some fundamentals of mineralogy and geochemistry. (Citato a pagina 3).

[16] Ge, P. and Fouletier, M. Electrochemical intercalation of sodium in graphite. *Solid state ionics*, 1988. (Citato alle pagine 3, 12, 22).

[17] Kawaguchi, M. and Kurasaki, A. Intercalation of magnesium into a graphite-like layered material of composition $BC_2N$. *Chemical Communications*, 2012. (Citato alle pagine 3, 12, 23).

[18] Aurbach, D., Lu, Z., Schechter, A., Gofer, Y., Gizbar, H., Turgeman, R., Cohen, Y., Moshkovich, M. and Levi, E. Prototype systems for rechargeable magnesium batteries. *Nature*, 2000. (Citato alle pagine 3, 12, 32, 52, 70).

[19] Crowe, A. J. and Bartlett, B. M. Solid state cathode materials for secondary magnesium-ion batteries that are compatible with magnesium metal anodes in water-free electrolyte. *Journal of Solid State Chemistry*, 2016. (Citato alle pagine 3, 12).

[20] Loutfy, R. O. and Katagiri S. Fullerene materials for lithium-ion battery applications. *Perspective of fullerene nanotechnology*, 2002. doi: 10.1007/0-306-47621-5_32. (Citato alle pagine 4, 5, 22, 24, 30, 57).

[21] Pramudita, J. C., Pontiroli, D., Magnani, G., Gaboardi, M., Riccò, M., Milanese, C., Brand, H. and Sharma, N. Graphene and selected derivatives as negative electrodes in sodium-and lithium-ion batteries. *ChemElectroChem*, 2015. (Citato alle pagine 4, 5, 26, 28, 52, 52, 53, 75).

[22] Yildirim, T. and Zhou, O. and Fischer, J. E. and Bykovetz, N. and Strongin, R. A. and Cichy, M. A. and Smith III, A. B. and Lin, C. L. and Jelinek, R. Intercalation of sodium heteroclusters into the $C_{60}$ lattice. *Letters to Nature*, (360), 1992. (Citato alle pagine 4, 21, 23).

[23] Quintavalle, D. and Borondics, F. and Klupp, G. and Baserga, A. and Simon, F. and Jànossy, A. and Kamaràs, K. and Pekker, S. Structure and properties of the stable two-dimensional conducting polymer $Mg_5C_{60}$. *Phys. Rev. B*, 2008. (Citato alle pagine 5, 23).

[24] Indranil Lahiri and Wonbong Choi. Carbon nanostructures in lithium ion batteries: Past, present, and future. *Critical Reviews in Solid State and Materials Sciences*, 2013. (Citato a pagina 5).

[25] Zhang, R., Mizuno, F. and Ling, C. Fullerenes: non-transition metal clusters as rechargeable magnesium battery cathodes. *Chemical Communications*, 2015. (Citato alle pagine 5, 13, 53, 98, 98).

[26] R. Zhang and F. Mizuno. Fullerenes as high capacity cathode materials for a rechargeable magnesium battery, 2013. URL `https://patents.google.com/patent/US20150099166`. US Patent US20150099166A1. (Citato alle pagine 5, 23, 98).

[27] Lian, P., Zhu, X., Liang, S., Li, Z., Yang, W. and Wang, H. Large reversible capacity of high quality graphene sheets as an anode material for lithium-ion batteries. *Electrochimica Acta*, 2010. (Citato alle pagine 5, 26).

[28] Pramudita, J. C., Rawal, A., Choucair, M., Pontiroli, D., Magnani, G., Gaboardi, M., Ricco, M. and Sharma, N. Mechanisms of sodium insertion/extraction on the surface of defective graphenes. *ACS applied materials & interfaces*, 2016. (Citato alle pagine 6, 55, 80, 86, 100).

[29] Z. Liu and X. Zhou. *GRAPHENE energy storage and conversion applications*. CRC press. (Citato alle pagine 6, 25, 25, 25, 26, 27, 28).

[30] Hassoun, J., Bonaccorso, F., Agostini, M., Angelucci, M., Betti, M.G., Cingolani, R., Gemmi, M., Mariani, C., Panero, S., Pellegrini, V. and Scrosati, B. An advanced lithium-ion battery based on a graphene anode and a lithium iron phosphate cathode. *Nano letters*, 2014. (Citato alle pagine 6, 55, 80).

[31] Wang, Q., Jiang, L., Yu, Y. and Sun, J. Progress of enhancing the safety of lithium ion battery from the electrolyte aspect. *Nano energy*, 2019. (Citato alle pagine 6, 87).

[32] Matsuo, M., Nakamori, Y., Orimo, S., Maekawa, H. and Takamura, H. Lithium superionic conduction in lithium borohydride accompanied by structural transition. *Applied physics letters*, 2007. (Citato alle pagine 6, 30, 31, 32).

[33] Wen, Z., Xu, X. and Li, J. Preparation, microstructure and electrical properties of $Li_{1.4}Al_{0.4}Ti_{1.6}(PO_4)_3$ nanoceramics. *Journal of electroceramics*, 2009. (Citato alle pagine 6, 30).

[34] Li, C., Wang, J., Chang, Z., Yin, Y., Yang, X. and Zhang, X. Preparation and characterization of PAN-LATP composite solid-state electrolyte. *SCIENTIA SINICA Chimica*, 2018. (Citato alle pagine 6, 30).

[35] Croce, F. and Appetecchi, G. B. and Persi, L. and Scrosati, B. Nanocomposite polymer electrolytes for lithium batteries. *Letters to nature*, 1998. (Citato alle pagine 6, 30, 31, 50).

[36] Riccò, M., Belli, M., Mazzani, M., Pontiroli, D., Quintavalle, D., Jánossy, A. and Csányi, G. Superionic conductivity in the $Li_4C_{60}$ fulleride polymer. *Physical review letters*, 2009. (Citato alle pagine 6, 22, 30, 87, 91).

[37] Pontiroli, D., Aramini, M., Gaboardi, M., Mazzani, M., Gorreri, A., Ricco, M., Margiolaki, I. and Sheptyakov, D. Ionic conductivity in the Mg intercalated fullerene polymer $Mg_2C_{60}$. *Carbon*, 2013. (Citato alle pagine 6, 22, 30).

[38] Chusid, O., Gofer, Y., Gizbar, H., Vestfrid, Y., Levi, E., Aurbach, D. and Riech, I. Solid-state rechargeable magnesium batteries. *Advanced Materials*, 2003. (Citato a pagina 7).

[39] Teprovich, J. A., Colon-Mercado, H. R., Ward, P. A., Peters, B., Giri, S., Zhou, J., Greenway, S., Compton, R. N., Jena, P. and Zidan R. Experimental and theoretical analysis of fast lithium ionic conduction in a $LiBH_4C_{60}$ nanocomposite. *The Journal of Physical Chemistry C*, 2014. (Citato alle pagine 7, 31, 88, 89, 92, 92).

[40] Battery university. batteryuniversity.com, . (Citato alle pagine 9, 33, 33, 33).

[41] Bohr, M. Let's clear up the node naming mess. https://newsroom.intel.com, 2017. (Citato a pagina 10).

[42] Davion Hill. Easing the risks of battery investment. https://www.energy-storage.news/blogs/easing-the-risks-of-battery-investment1, 2019. (Citato a pagina 10).

[43] Eoin Malins. Storing your stuff with clever filesystems: ZFS and tmpfs, 2018. (Citato a pagina 10).

[44] Ian Heggie. What is the total internet speed of the world? https://www.quora.com/What-is-the-total-Internet-speed-of-the-world, 2018. (Citato a pagina 10).

[45] Goodenough, J. and Park, K. The li-ion rechargeable battery: a perspective. *Journal of the American Chemical Society*, 2013. (Citato a pagina 11).

[46] Zhecheva, E., Stoyanova, R., Jiménez-Mateos, J. M., Alcàntara, R., Lavela, P. and Tirado, J. L. EPR study on petroleum cokes annealed at different temperatures and used in lithium and sodium batteries. *Carbon*, 2002. (Citato a pagina 13).

[47] Alcàntara, R., Jiménez-Mateos, J. M., Lavela, P. and Tirado, J. L. Carbon black: a promising electrode material for sodium-ion batteries. *Electrochem. Commun.*, 2001. (Citato a pagina 13).

[48] Thomas, P., Ghanbaja, J., and Billaud, D. Electrochemical insertion of sodium in pitch-based carbon fibres in comparison with graphite in $NaClO_4$-ethylene carbonate electrolyte. *Electrochimica acta*, 1999. (Citato a pagina 13).

[49] Dubois, M., and Billaud, D. Electrochemical impedance spectroscopic study of the intercalation of lithium and sodium ions into polyparaphenylene in carbonate-based electrolytes. *Electrochimica acta*, 2002. (Citato a pagina 13).

[50] Li, Y., Hu, Y. S., Titirici, M. M., Chen, L., and Huang, X. Hard carbon microtubes made from renewable cotton as high-performance anode material for sodium-ion batteries. *Advanced Energy Materials*, 2016. (Citato a pagina 13).

[51] Alcàntara, R., Jaraba, M., Lavela, P., and Tirado, J. L. $NiCo_2O_4$ spinel: first report on a transition metal oxide for the negative electrode of sodium-ion batteries. *Chemistry of Materials*, 2002. (Citato a pagina 13).

[52] Fang, Y., Yu, X.Y. and Lou, X.W.D. Nanostructured electrode materials for advanced sodium-ion batteries. *Matter*, 2019. (Citato a pagina 13).

[53] Park, C. W., Ahn, J. H., Ryu, H. S., Kim, K. W. and Ahn, H. J. Room-temperature solid-state sodium/sulfur battery. *Electrochemical and solid-state letters*, 2006. (Citato alle pagine 13, 97).

[54] Inoishi, A., Omuta, T., Kobayashi, E., Kitajou, A., and Okada, S. A single-phase, all-solid-state sodium battery using $\mathrm{na}_{3-x}\mathrm{v}_{2-x}zr_x(\mathrm{po}_4)_3$ as the cathode, anode, and electrolyte. *Advanced Materials Interfaces*, 2017. (Citato alle pagine 13, 97).

[55] Wang, L., Welborn, S.S., Kumar, H., Li, M., Wang, Z., Shenoy, V.B. and Detsi, E. High-rate and long cycle-life alloy-type magnesium-ion

battery anode enabled through (de)magnesiation-induced near-room-temperature solid-liquid phase transformation. *Advanced Energy Materials*, 2019. (Citato a pagina 13).

[56] Niu, J., Yin, K., Gao, H., Song, M., Ma, W., Peng, Z. and Zhang, Z. Composition-and size-modulated porous bismuth-tin biphase alloys as anodes for advanced magnesium ion batteries. *Nanoscale*, 2019. (Citato a pagina 13).

[57] Kroto, H.W. and Heath, J.R. and O'Brien, S.C. and Curl, R.F. and Smalley, R.E. C60: Buckminsterfullerene. *Nature*, 1985. doi: 318(6042): 162-163. (Citato a pagina 17).

[58] Burchell, T. D. *Carbon materials for advanced technology.* 1999. (Citato alle pagine 17, 17, 18, 18, 20, 20, 21).

[59] Liu, Z. G., Ohi, H., Masuyama, K., Tsuchiya, K. and Umemoto, M. Investigation on structure transition of fullerene during mechanical alloying and subsequent treatments. *J. Mater. Res.*, 2000. (Citato alle pagine 17, 53, 58, 69).

[60] Fetzer, J. C. and Gallegos, E. J. The separation and identification of higher molecular weight fullerenes. *Polyciclic aromatic compounds*, 1992. (Citato a pagina 17).

[61] Kroto, H.W. The stability of the fullerenes $C_n$, with n = 24, 28, 32, 36, 50, 60 and 70. *Nature*, 1987. doi: 329.6139:529âĂŞ531. (Citato a pagina 18).

[62] New allotropes of carbon. http://www.chimdocet.it, . (Citato alle pagine 18, 19).

[63] Forrò, L. and Mihàly L. Electronic properties of doped fullerenes. *Reports on progress in physics*, 2001. (Citato alle pagine 19, 21, 22, 22).

[64] Andreoni, W., Gygi, F. and Parrinello, M. Structural and electronic properties of $C_{70}$. *Chemical physics letters*, 1992. (Citato alle pagine 19, 20).

[65] Hess, B. C., Bowersox, D. V., Mardirosian, S. H. and Unterberger, L. D. Electroabsorption in $C_{60}$ and $C_{70}$. Third-order nonlinearity in molecular and solid states. *Chemical physics letters*, 1996. (Citato a pagina 20).

[66] Pontiroli, D. Synthesis, structural investigation and spectroscopic properties of lithium fullerides. PhD Thesis, 2006. (Citato a pagina 21).

[67] Udvardi, L. and Szabò, G. A lattice-gas model for alkali-metal fullerides: face-centred-cubic structure. *Journal of Physics: Condensed Matter*, 1996. (Citato a pagina 21).

[68] Mixed interfullerene bonding motifs in $C_{60}$-based polymers. http://www.esrf.eu/UsersAndScience/Publications/Highlights/2005/Materials/MAT11, 2005. (Citato a pagina 23).

[69] Chabre, Y. and Djurado, D. and Armand, M. and Romanow W. R. and Coustel, N. and McCauley, J. P. and Fischer J. E. and Smith, A. B. Electrochemical intercalation of lithium into solid $C_{60}$. *Journal of the american electrochemical society*, 1992. (Citato a pagina 23).

[70] Zhang, R., Mizuno, F. and Ling, C. Fullerene: non-transition metal clusters as rechargeable magnesium battery cathodes. *Chem. Commun.*, 2015. (Citato a pagina 23).

[71] Talyzin, A. and Tsybin, Y. and Purcell, J. and Schaub, T. and Shulga, Y. and Noreus, D. and Sato, T. and Dzwilewski, A. and Sundqvist, B. and Marshall, A. Reaction of hydrogen gas with $C_{60}$ at elevated pressure and temperature: Hydrogenation and cage fragmentation. *Journal of physical chemistry*, 2006. (Citato a pagina 24, 24).

[72] Hall, L. and McKenzie, D. and Attalla, M. and Vassallo, A. and Davis, R. and Dunlop, J. and Cockaynet, D. The structure of hydrogenated fullerene ($C_{60}H_{36}$). *Journal of physical chemistry*, 1993. (Citato a pagina 24, 24).

[73] Bianco, A., Cheng, H. M., Enoki, T. et al. All in the graphene family—a recommended nomenclature for two-dimensional carbon materials. *Carbon*, 2013. (Citato a pagina 25).

[74] Rutgers physics and astronomy. www.physics.rutgers.edu, 2019. (Citato a pagina 26).

[75] Rani, P. and Jindal, V. K. Designing band gap of graphene by B and N dopant atoms. *RSC Advances*, 2012. (Citato a pagina 26).

[76] McCann, E. and Koshino, M. The electronic properties of bilayer graphene. *Rep. Prog. Phys.*, 2013. (Citato a pagina 26).

[77] Zhou, X., Wang, F., Zhu, Y. et al. Graphene modified $LiFePO_4$ cathode materials for high power lithium ion batteries. *J. Mater. Chem.*, 2011. (Citato a pagina 26).

[78] Wang, H., Cui, L. F., Yang, Y., Sanchez Casalongue, H., Robinson, J. T., Liang, Y. et al. $Mn_3O_4$graphene hybrid as a high-capacity anode material for lithium ion batteries. *Journal of the American Chemical Society*, 2010. (Citato a pagina 26).

[79] Hu, L., Wu, F., Lin, C., Khlobystov, A. and Li, L. Graphene-modified $LiFePO_4$ cathode for lithium ion battery beyond theoretical capacity. *Nature Communications*, 2013. (Citato a pagina 27).

[80] Chou, S., Wang, J., Choucair, M., Liu, H., Stride, J. and Dou, S. Enhanced reversible lithium storage in a nanosize silicon/graphene composite. *Electrochemistry Communications*, 2010. (Citato a pagina 27).

[81] Gaboardi, M., Bliersbach, A., Bertoni, G., Aramini, M., Vlahopoulou, G., Pontiroli, D., Mauron, P., Magnani, G., Salviati, G., Züttel, A. and Riccò, M. Decoration of graphene with nickel nanoparticles: study of the interaction with hydrogen. *Journal of Materials Chemistry A*, 2014. (Citato alle pagine 28, 29, 75).

[82] Pontiroli, D., Aramini, M., Gaboardi, M., Mazzani, M., Sanna, S., Caracciolo, F., Carretta, P., Cavallari, C., Rols, S., Tatti, R. and Aversa, L. Tracking the hydrogen motion in defective graphene. *The Journal of Physical Chemistry C*, 2014. (Citato a pagina 29).

[83] Moore, E. A. and Smart, L. E. *Solid state chemistry.* Taylor and Francis, 2005. (Citato a pagina 30).

[84] Agrawal, R. C. and Pandley, G. P. Solid polymer electrolytes: materials designing and all-solid-state battery applications: an overview. *Topical reviews*, 2008. (Citato a pagina 31).

[85] Wieczorek, C. and Florjanczyk, Z. and Stevens, J. R. Composite polyether based solid electrolyte. *Electrochimica acta*, 1995. (Citato alle pagine 31, 50).

[86] Sveinbjornsson, D., Myrdal, G. J. S., Blanchard, D., Bentzen, J. J., Hirata, T., Mogensen, M. B., Norby, P., Orimo, S. and Vegge, T. Effect of heat treatment on the lithium ion conduction of the $LiBH_4$-LiI solid solution. *J. Phys. Chem.*, 2013. (Citato a pagina 31).

[87] Sveinbjornsson, D., Myrdal, G. J. S., Blanchard, D., Bentzen, J. J., Hirata, T., Mogensen, M. B., Norby, P., Orimo, S. and Vegge, T. Effect of heat treatment on the lithium ion conduction of the $LiBH_4$-LiI solid solution. *J. Phys. Chem.*, 2013. (Citato a pagina 31).

[88] Besenhard, J. O. *Handbook of battery materials.* Wiley, 1999. (Citato alle pagine 33, 46, 47, 47, 48).

[89] Cobalt institute. Critical Raw Material. https://www.cobaltinstitute.org/critical-raw-material.html, 2019. (Citato a pagina 33).

[90] Kittel, C. *Introduction to solid state physics, Eighth Edition.* Wiley. (Citato alle pagine 36, 36, 38, 38).

[91] Cullity, B. D. *Elements of X-ray diffraction.* Addinson Wesley. (Citato a pagina 40).

[92] Scaravonati, S., Magnani, G., Gaboardi, M., Allodi, G., Riccò, M. and Pontiroli, D. Electrochemical intercalation of fullerene and hydrofullerene with sodium. *Carbon*, 2018. (Citato alle pagine 40, 48, 50, 51, 53, 54, 55, 57, 60, 60, 60, 61, 61, 61, 62, 63, 64, 64, 65, 65, 66, 66, 67, 67, 67, 68, 68, 68, 68, 96, 96).

[93] Pontiroli, D., Scaravonati, S., Sidoli, M., Magnani, G., Fornasini, L., Milanese, C. and Riccò, M. Fullerene mixtures as negative electrodes in innovative na-ion batteries. *Chemical Physics Letters*, 2019. (Citato alle pagine 40, 48, 53, 53, 54, 55, 57, 58, 58, 59, 59, 59, 59, 61, 62, 63, 63, 69, 69, 69, 69, 97).

[94] Bruker. Instrument configuration for powder diffraction. Advanced X-ray Workshop, S.N. Bose National Centre for Basic Sciences, 2011. (Citato a pagina 40, 40).

[95] Barsoukov, E. and Macdonald J. R. *Impedance Spectroscopy Theory, Experiment, and Applications.* 2005. (Citato alle pagine 41, 41, 42, 42, 43, 44, 44, 45).

[96] Raleigh, D. O. *Electroanalytical Chemistry.* 1972. (Citato a pagina 42).

[97] Huggins, R. A. Simple method to determine electronic conductivity in mixed and ionic components of the conductors. *Ionics*, 2002. (Citato alle pagine 43, 43, 43, 43, 44, 44).

[98] Bard, A. J. and Faulkner, L. R. *Electrochemical Methods: Fundamentals and Applications, Second Edition.* Wiley. (Citato a pagina 44).

[99] Ho, C., Raistrick, I. D. and Huggins, R. A. Application of A-C techniques to the study of lithium diffusion in tungsten trioxide thin films. *J. Electrochem. Soc.*, 1980. (Citato a pagina 44).

[100] Elgrishi, N., Rountree, K. J., McCarthy, B. D., Rountree, E. S., Eisenhart, T. T. and Dempsey, J. L. A practical beginner's guide to cyclic voltammetry. *J. Chem. Educ.*, 2017. (Citato alle pagine 48, 49).

[101] Schweikert, N., Heinzmann, R., Eichhofer, A., Hahn, H. and Indris, S. Electrochemical impedance spectroscopy of $Li_4Ti_5O_{12}$ and $LiCoO_2$ based half-cells and $Li_4Ti_5O_{12}/LiCoO_2$ cells: Internal interfaces and influence of state-of-charge and cycle number. *Solid State Ionics*, 2012. (Citato a pagina 63).

[102] Oszlànyi, G., Baumgartner, G., Faigel, G. and Forrò, L. $Na_4C_{60}$: an alkali intercalated two-dimensional polymer. *Phys. Rev. Lett.*, 1997. (Citato alle pagine 65, 96).

[103] Rosseinsky, M. J., Murphy, D. W., Fleming, R. M., Tycko, R., Ramirez, A. P., Dabbagh, G. and Barrett, S. E. Structural and electronic properties of sodium intercalated $C_{60}$. *Nature*, 1992. (Citato a pagina 65).

[104] An, S. J., Li, J., Daniel, C., Mohanty, D., Nagpure, S. and Wood, D. L. The state of understanding of the lithium-ion-battery graphite solid electrolyte interphase (sei) and its relationship to formation cycling. *Carbon*, 2016. (Citato a pagina 67).

[105] Klupp, G., Matus, P., Quintavalle, D., Kiss, L. F., Kovàts, É., Nemes, N. M., Kamaràs, K., Pekker, S. and Jànossy, A. Phase segregation on the nanoscale in $Na_2C_{60}$. *Phys. Rev. B*, 2006. (Citato a pagina 68).

[106] Rachdi, F., Hajji, L., Galtier, M., Yildirim, T., Fischer, J. E., Goze, C. and Mehring, M. $^{13}C$ and $^{23}Na$ NMR studies of $Na_2C_{60}$ and $Na_6C_{60}$ fullerides. *Phys. Rev. B*, 1997. (Citato a pagina 68).

[107] Sundqvist, B., Andersson, O., Gong, C., Liu, B., Tonpheng, B., Yu, J. and Yao, M. AC impedance of $A_4C_{60}$ fullerides under pressure. *N. J. Phys.*, 2015. (Citato a pagina 68).

[108] Baril, D. and Chabre, Y. Electrochemical Time of Flight Investigation of $C_{60}$ Dissolution-Diffusion into a Polymer Electrolyte. *Electrochemical and solid-state letters*, 2001. (Citato a pagina 68).

[109] Lad'yanov, V. I., Nikonova, R. M., Larionova, N. S., Aksenova, V.V., Mukhgalin, V. V., Rud', A. D. Deformation-induced changes in the structure of fullerites $C_{60/70}$ during their mechanical activation. *Phys. Solid State*, 2013. (Citato alle pagine 68, 68, 68, 93).

[110] Kaminsky, J., Budesìnsky, M., Taubert, S., Bour, P. and Straka, M. Fullerene $C_{70}$ characterization by $^{13}c$ NMR and the importance of the solvent and dynamics in spectral simulations. *Physical Chemistry Chemical Physics*, 2013. (Citato a pagina 69).

[111] Allemand, P. M., Koch, A., Wudl, F., Rubin, Y., Diederich, F., Alvarez, M. M., et al. Two different fullerenes have the same cyclic voltammetry. *J. Am. Chem. Soc.*, 1991. (Citato a pagina 69).

[112] Pontiroli, D., Aramini, M., Gaboardi, M., Mazzani, M., Gorreri, A., Riccò, M., Margiolaki, I., Sheptyakov, D. Ionic conductivity in the Mg intercalated fullerene polymer $Mg_2C_{60}$. *Carbon*, 2012. (Citato a pagina 74).

[113] Béguin, F., Presser, V., Balducci, A. and Frackowiak, E. Carbons and electrolytes for advanced supercapacitors. *Advanced materials*, 2014. (Citato a pagina 87).

[114] Chen, G. Z. Understanding supercapacitors based on nano-hybrid materials with interfacial conjugation. *Progress in Natural Science: Materials International*, 2013. (Citato a pagina 87, 87).

[115] Simon, P., Gogotsi, Y., and Dunn, B. Where do batteries end and supercapacitors begin? *Science*, 2014. (Citato a pagina 87).

[116] Li, N., Du, Y., Feng, Q. P., Huang, G. W., Xiao, H. M. and Fu, S. Y. A novel type of battery-supercapacitor hybrid device with highly switchable dual performances based on a carbon skeleton/$Mg_2Ni$ free-standing hydrogen storage electrode. *ACS applied materials & interfaces*, 2017. (Citato alle pagine 87, 100).

[117] Hwang, S. J., Bowman, R. C., Reiter, J. W., Rijssenbeek, J., Soloveichik, G. L., Zhao, J. C., Kabbour, H. and Ahn, C. C. NMR confirmation for formation of $[B_{12}H_{12}]^{2-}$ complexes during hydrogen desorption from metal borohydrides. *The Journal of Physical Chemistry C*, 2008. (Citato a pagina 93).

[118] Echegoyen, L. and Echegoyen L. E. Electrochemistry of fullerenes and their derivatives. *Acc. Chem. Res.*, 1998. (Citato a pagina 96).

[119] Ong, T. S., and Yang, H. Symmetrical cell for electrochemical ac impedance studies of lithium intercalation into graphite. *Electrochemical and Solid State Letters*, 2001. (Citato alle pagine 97, 99).

[120] Uhlmann, C., Illig, J., Ender, M., Schuster, R. and Ivers-Tiffée, E. In situ detection of lithium metal plating on graphite in experimental cells. *Journal of Power Sources*, 2015. (Citato a pagina 100).

[121] Lu, L., Han, X., Li, J., Hua, J. and Ouyang, M. A review on the key issues for lithium-ion battery management in electric vehicles. *Journal of Power Sources*, 2013. (Citato a pagina 100).

[122] Wang, Y., Zhang, C. and Chen, Z. A method for state-of-charge estimation of $LiFePO_4$ batteries at dynamic currents and temperatures using particle filter. *Journal of Power Sources*, 2015. (Citato a pagina 100).